The Atomic Structure of the
Indium Antimonide (001) Surface.

Thesis submitted for the degree of

Doctor of Philosophy

at the University of Leicester

by

Nigel Jones BSc (Hons) (Leicester)

Department of Physics and Astronomy

University of Leicester

March 1998

UMI Number: U105888

UMI

Dissertation Publishing

UMI U105888

ProQuest

The Atomic Structure of the
Indium Antimonide (001) Surface.

Nigel Jones

Abstract

The atomic structures of the c(8x2) and c(4x4) reconstructions of InSb(001) have been determined using surface X-ray diffraction. Large in-plane and out-of-plane data sets were measured for each of the reconstructions, enabling a detailed model of the precise atomic structure to be calculated for the first time. A new model, consisting of chains of indium atoms, separated by parallel pairs of antimony dimers on top of an antimony terminated bulk, has been proposed for the InSb(001)-c(8x2) reconstruction. The model represents a significant departure from any of the models previously suggested for the c(8x2) reconstruction of the III-V (001) surfaces. The InSb(001)-c(4x4) surface is found to be consistent with a previously reported missing dimer model. It is proposed, however, that the groups of dimers are incomplete in approximately one third of the cases. The dimer bond lengths and the corresponding bond angles, have also been determined for the first time. The c(4x4) reconstruction is found to be notably flatter than the c(8x2) reconstruction.

A surface phase transition study from the highly ordered c(4x4) phase to a disordered *asymmetric*(1x3) phase, shows that a fully reversible transition takes place. The results indicate that the transition is a consequence of random desorption of antimony dimer atoms in distinct isolated regions, rather than a general reduction in domain size.

Oxide removal from the InSb(001) surface has been achieved using a number of techniques. The quality of the resulting surfaces was determined from the reflected X-ray intensity and the in-plane fractional-order reflections.

Acknowledgements.

This thesis is based on the following articles:

Chapter 5   N. Jones, C. Norris, C.L. Nicklin, P. Steadman, J.S.G. Taylor, C.F. McConville and A.D. Johnson, Surf.Sci. **398** (1998) 105.

Chapter 7   N. Jones, C. Norris, C.L. Nicklin, P. Steadman, S.H. Baker and S.L. Bennett, accepted for publication, Surf. Sci. Jan. 1998.

Chapter 8   N. Jones, C. Norris, C.L. Nicklin, P. Steadman, J.S.G. Taylor, A.D. Johnson and C.F. McConville, Appl. Surf. Sci. **123/124** (1998) 141.

Contents.

Chapter 1.

Introduction.

A detailed knowledge of the physics and chemistry of semiconductor surfaces is an essential requirement in the manufacture of modern electronic devices. The atomic geometry of a surface is a most fundamental property and therefore, research in this field clearly has to start at this level, that is, with an accurate description of the surface atomic structure.

A surface is created when the three dimensional periodicity of a crystal is terminated, for example, by cleavage of the crystal. In direct consequence, the atoms at the surface have a reduced atomic coordination and a lower symmetry than their bulk counterparts. The surface atoms therefore have distinctly different properties to those in the bulk.

In spite of the fact that the surface region contains only a small number of atomic layers, the performance of a semiconductor device is critically influenced by precisely this region. For instance, the resulting atomic geometry may lead to the formation of new localised electronic states of the surface which will affect the properties of any interface grown upon it. These so-called surface states account, in part, for the height of the Schottky barrier experienced by electrons travelling from a semiconductor to a metal. Surface states can also be associated with changes in potential due to relaxation, surface reconstruction and structural imperfections or defects, which may all arise upon the creation of a surface. If the charge associated with any of the

surface states is different from the bulk charge distribution, then band bending occurs; the surface states therefore directly affect the electrical properties of a surface.

The study of the atomic structure of semiconductor surfaces has been greatly enhanced in recent years because of the large developments in surface science techniques coupled with the advent of molecular beam epitaxy (MBE). The most commonly used techniques in the determination of the atomic structure of semiconductor surfaces include, low energy electron diffraction (LEED), reflection high energy electron diffraction (RHEED), photoemission spectroscopy (PES) and more recently, surface X-ray diffraction (SXRD) and scanning tunnelling microscopy (STM). SXRD is now widely established as a powerful probe of surface crystallography, and because of the weak interaction of X-rays with matter, the scattered intensities can be interpreted using kinematic theory. The development of purpose built synchrotron radiation sources has provided the necessary intensity required to perform an X-ray scattering experiment.

MBE has opened up a wide field of study as it provides the necessary flexibility for varying the surface stoichiometry of a sample while simultaneously monitoring the evolution of a structure. The MBE growth of compound semiconductors can, in particular, be dictated as the growth kinetics are dominated by the different sticking coefficients of the corresponding elements. This ability to control the composition of a surface at an atomic level, has enabled novel structures with specific properties to be fabricated.

The contents of this thesis describe a complete investigation of the chemically clean (001) surface of indium antimonide using surface X-ray diffraction. General III-V semiconductors are introduced in chapter 2. The concept of surface reconstruction, and in particular the reconstructions exhibited by the InSb(001) surface are also outlined. The kinematic theory of X-ray diffraction is summarised in chapter 3 and the relevant experimental aspects, including diffractometry and data analysis methods, are highlighted in chapter 4.

The determination of the atomic structure of the InSb(001)-c(4x4) reconstruction is described in detail in chapter 5, and a study of the phase transition between the c(4x4) surface phase and an *asymmetric*(1x3) surface phase is presented in chapter 6. In chapter 7, the determination of a novel atomic structure for the c(8x2) reconstruction of InSb(001) is described, and a study of the removal of the native oxide from InSb(001) substrates is reported in chapter 8. Finally, the experimental work is summarised in chapter 9.

Chapter 2.

The Indium Antimonide (001) surface.

2.1   Introduction.

Compound III-V materials are formed when atoms from group IIIb of the periodic table combine with atoms from group Vb. The resulting compounds are both crystalline and semiconducting and contain an equal proportion of both atom types. III-V semiconductors (III-Vs) therefore have, on average, the same number of electrons per atom as the group IV semiconductors which include silicon and germanium.

The first structural analysis of the III-V compound semiconductors was performed in 1929 by Goldschmidt [1] who confirmed the crystal structure is similar to that of diamond, but with a lower symmetry as there are two atom types per unit cell.
III-V semiconductors possess distinctly different properties from their group IV counterparts which are perfectly covalent. In III-V semiconductors the interstitial electron density is diminished and there is a tendency for the electron cloud around the group V ion core to have more charge than is necessary to compensate the positive charge, whereas the electron cloud around the group III ion core has somewhat less. The crystal is therefore primarily covalent but has a slight ionic character as well.

As there are two atom types per unit cell there are a number of possible III-V combinations and the resulting compounds cover a wide range of semiconducting

properties. Certain properties of the most commonly used III-Vs are listed in Table 2.1.

III-V compounds crystallise in an arrangement in which each atom is at the centre of a regular tetrahedron, the corners of which are occupied by an atom of the opposite type. These tetrahedra can be arranged into two different structures, zinc-blende which is cubic and wurzite which is hexagonal. The cubic zinc-blende structure has the same geometry as the diamond structure but has different atom types occupying alternate sites in the lattice inferring a lower symmetry on the structure. The wurzite structure is similar to zinc-blende except that alternate (111) layers are rotated through 180° about the [111] axis resulting in a hexagonal symmetry.

All compounds containing antimony, arsenic and phosphorus, on which most attention has been focused, adopt a zinc-blende structure; the nitrides of the group III elements have the wurzite form. Wurzite and zinc-blende structures are similar differing only in the relative positions of the third nearest neighbours, which are closer together in the wurzite form. The third nearest neighbours are unlike atoms and crystals with a wurzite structure are likely to have a larger charge difference between atom types. It is significant that nitrogen has a noticeably larger electronegativity than the other group V elements leading to the formation of a wurzite structure in nitrides. Conversely, crystals having a zinc-blende structure are unlikely to have a significant charge on atoms implying there is not a large ionic contribution to the bonding. The zinc-blende and wurzite structures [2] are shown schematically in fig. 2.1.

For completeness, it is noted that boron nitride is different with a hexagonal structure similar to that of graphite and the bismuthides are infact metallic compounds without tetrahedral structure.

	Band Gap (eV)	m_e^*	melting point (°C)
InSb	0.17	0.014	525
InAs	0.36	0.022	942
InP	1.27	0.067	1057
GaSb	0.67	0.050	707
GaAs	1.29	0.068	1237
GaP	2.25	0.35	1477
AlSb	1.60	0.09	1057
AlAs	2.16	-	1597
AlP	2.50	-	1497
C	5.40	-	> 4000
Si	1.11	0.580	1410
Ge	0.67	0.350	958

Table 2.1: *Selected properties of III-V semiconductors. Certain group IV elements have been included for comparison.*

Surface Reconstruction

A surface is created by the termination of the three dimensional periodicity of an atom in bulk crystal. In the case of the semiconductor materials this is commonly ... layer crystals (covalently bonded) crystals, in which there is a ... bond. ... covalent crystals semiconductors is strongly ... in the case of semiconductor compound structures the electrons are ... to remain ... surface. The presence of a semiconductor surface by cleavage creates a large number of unsatisfied electrons, these unsatisfied or 'dangling' bonds. ... gives rise to ... at the high reactivity of semiconductor surfaces and explain why ... chemically reactive surface many semiconductors. It follows that a newly created surface is in an energetically favourable state and the surface will attempt to minimise the dangling bond density, e.g. by oxidation. The surface can, however, also lower its free energy without reacting with foreign atoms. One such example of this is surface reconstruction.

When a surface reconstructs it frequently adopts a structure with a higher periodicity (and a lower symmetry) to that of the bulk. Dangling bonds are commonly satisfied by ... the inclusion of the atoms from the bond can, involves ... strain in the surface just as the ability of a surface to lower its ... free energy ... length ...

Fig. 2.1: The *(a) zincblende and (b) wurzite crystal structures.*

2.2 Surface Reconstruction.

A surface is created by the termination of the three dimensional periodicity of an infinite bulk crystal. In the case of semiconductor materials this is commonly achieved by cleavage of a crystal. Unlike metallic crystals, in which there is a delocalised sea of electrons, the bonding within semiconductors is strongly directional and in the case of tetrahedrally bonded structures the electrons are confined to definite sp^3 orbitals. The creation of a semiconductor surface by cleavage creates a large number of unpaired electrons, that is, unsatisfied or 'dangling' bonds. Dangling bonds are responsible for the high reactivity of semiconductor surfaces and explain why surface oxides rapidly form on many semiconductors. It follows that a newly created surface is clearly in an energetically unfavourable state and the surface will attempt to minimise the dangling bond density, e.g. by oxidation. The surface can, however, also lower its free energy without reacting with foreign atoms. One such example of this is surface reconstruction.

When a surface reconstructs it frequently adopts a structure with a higher periodicity (and a lower symmetry) to that of the bulk. Dangling bonds are commonly satisfied by dimerisation of surface atoms. The movement of atoms to form the bond can, however, induce strain in the uppermost surface layers. The ability of a surface to reconstruct and lower its free energy is therefore limited by the amount of strain that can be accommodated by the surface. It is ultimately the minimum in the total surface energy that determines the final surface atomic structure. A common characteristic of a large proportion of semiconductor surfaces is that atomic reconstruction is not confined solely to the uppermost surface layer. Many semiconductor surfaces, e.g. Si(111)-(7x7), actually exhibit reconstructions which extend several layers into the bulk [3].

2.3 Indium Antimonide (001).

Indium antimonide, InSb, has probably been the most intensively studied III-V semiconductor because of the distinct properties that arise from its narrow band gap

and high electron mobility. The narrow band gap gives InSb a high absorption coefficient associated with band to band transitions for wavelengths below ~6μm. In consequence InSb is widely used in infra-red (IR) detectors, lasers and filters.

Single crystal InSb was used for all the experiments reported in this thesis. The technique used for the production of single crystal InSb is the Czochralski vertical-pulling method [4]. More precisely, it was the InSb(001) surface that was of specific interest, this surface being prepared from the large pulled crystal by cleavage under vacuum. There are, in general, two main difficulties in producing crystals of a particular orientation: i) change of orientation by twinning and ii) contamination by foreign atoms. These factors are controlled by good epitaxy between the seed and the melt in the seeding on process and growth in a hydrogen atmosphere which helps maintain oxygen free conditions.

The advent of molecular beam epitaxy (MBE) has provided great flexibility in the variation of surface composition of III-V semiconductors and it is the (001) surface of InSb that is more widely used than any of its other surfaces for epitaxial growth. The first detailed study of the InSb(001) surface was performed by Oe *et al* [5] using reflection high-energy electron diffraction (RHEED). They reported the existence of three main surface reconstructions. These were, in order of increasing antimony concentration, the c(8x2), the *asymmetric*(1x3) and the $(2\sqrt{2} \times 2\sqrt{2})R45°$ reconstructions, the surfaces being classified using the Wood notation [6]. They found the c(8x2) surface was indium rich and was present at all temperatures when the Sb/In ratio was less than unity. The other two reconstructions were only observed between certain temperatures and when the Sb/In ratio was greater than unity. A so-called *pseudo* (4x3) structure was also proposed to exist in a narrow transition region where the ratio of Sb/In ~ 1. A surface phase diagram was established from these findings, with substrate temperature and surface stoichiometry as parameters. The surface phase diagram is shown in fig. 2.2. It is noted that the $(2\sqrt{2} \times 2\sqrt{2})R45°$ cell is the primitive unit cell of a c(4x4) structure. The c(4x4) notation is less cumbersome and has been widely adopted in place of the $(2\sqrt{2} \times 2\sqrt{2})R45°$ notation.
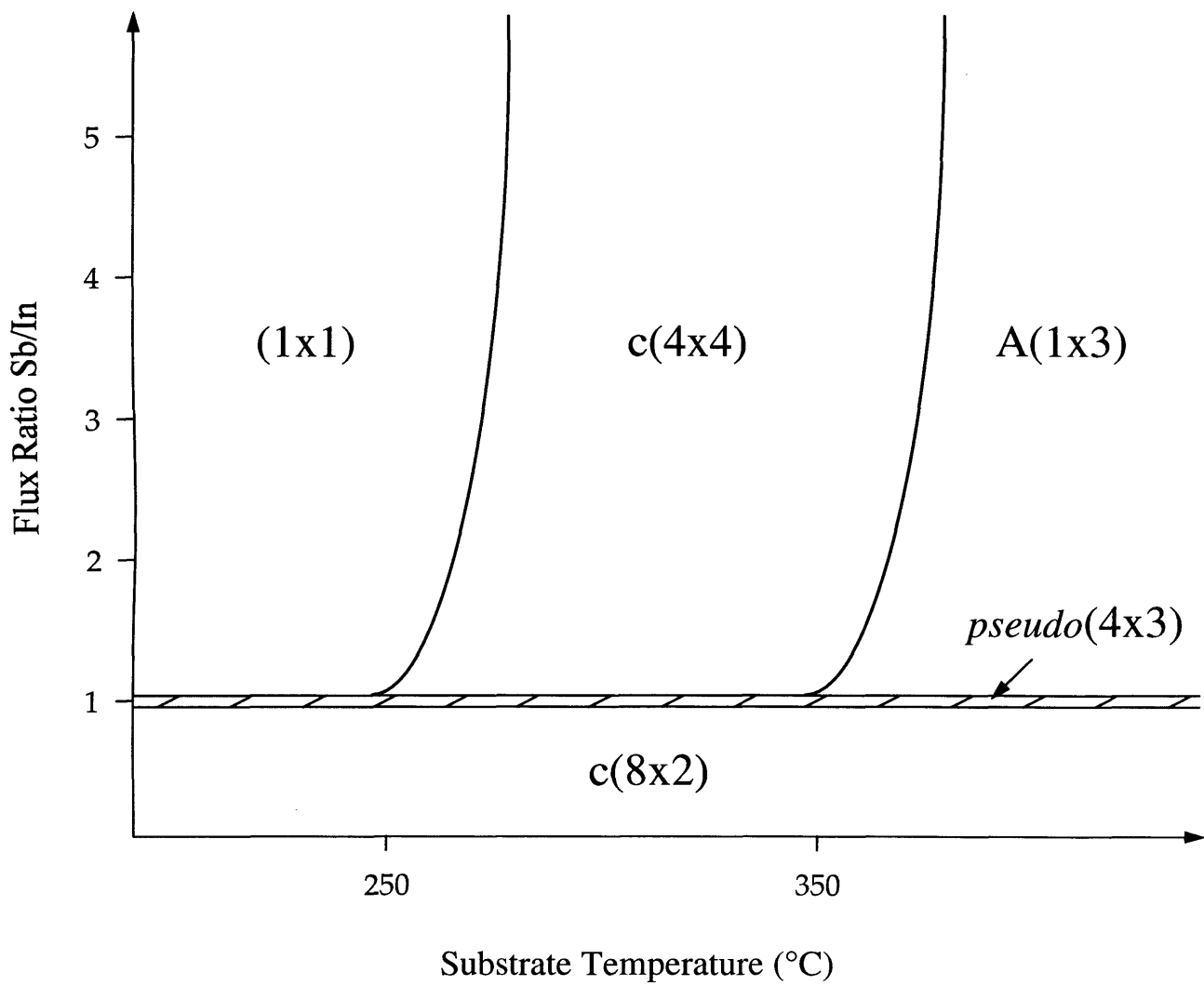
Fig. 2.2: *Surface phase diagram of the InSb(001) surface, established using RHEED measurements [5].*

In contrast to the (001) surface of GaAs there have been few fundamental studies of InSb(001) surfaces. There is a strong consensus that the c(4x4) surface consists of dimers [7,8,9], though the exact atomic positions have not been determined. The precise nature of the c(8x2) surface of both GaAs(001) and InSb(001) also remains very much unresolved, with several possible models proposed [7,10,11]. A number of techniques, including scanning tunnelling microscopy (STM) [12], photoemission spectroscopy (PES) [7], reflection high energy electron diffraction (RHEED) [13] and total energy based theoretical calculations [14], have been employed in an attempt to determine the surface structure of both the c(4x4) and the c(8x2) reconstructions.

2.3.1 The c(8x2) reconstruction.

The InSb(001)-c(8x2) reconstruction is indium rich and is observed at all temperatures up to close to the melting point of InSb. Fig. 2.3 shows the real space and reciprocal space lattice patterns of the c(8x2) surface in the two dimensional surface plane. The reciprocal space lattice pattern is what is actually measured during a surface X-ray diffraction experiment. The fractional-order peaks, which arise solely due to the reconstructed surface, are denoted by the smaller circles in fig. 2.3. The larger open circles represent in-plane Anti-Bragg peaks and the filled circles in-plane Bragg peaks. For the c(8x2) reconstruction the reciprocal space lattice is derived from its real space counterpart using equations (2.1) - (2.3).

$$\mathbf{a_1}' = 4\mathbf{a_1} + \mathbf{a_2} = \frac{a_0}{2}(5\mathbf{i} - 3\mathbf{j}) \qquad \mathbf{b_1}' = \frac{\pi}{2a_0}(\mathbf{i} - \mathbf{j}) = \frac{1}{4}\mathbf{b_1} \qquad (2.1)$$

$$\mathbf{a_2}' = 2\mathbf{a_2} = a_0(\mathbf{i} + \mathbf{j}) \qquad \mathbf{b_2}' = \frac{\pi}{4a_0}(3\mathbf{i} + 5\mathbf{j}) = \frac{1}{2}\mathbf{b_2} - \frac{1}{8}\mathbf{b_1} \qquad (2.2)$$

$$\mathbf{a_3}' = \mathbf{a_3} = a_0\mathbf{k} \qquad \mathbf{b_3}' = \mathbf{b_3} = \frac{2\pi}{a_0}\mathbf{k} \qquad (2.3)$$
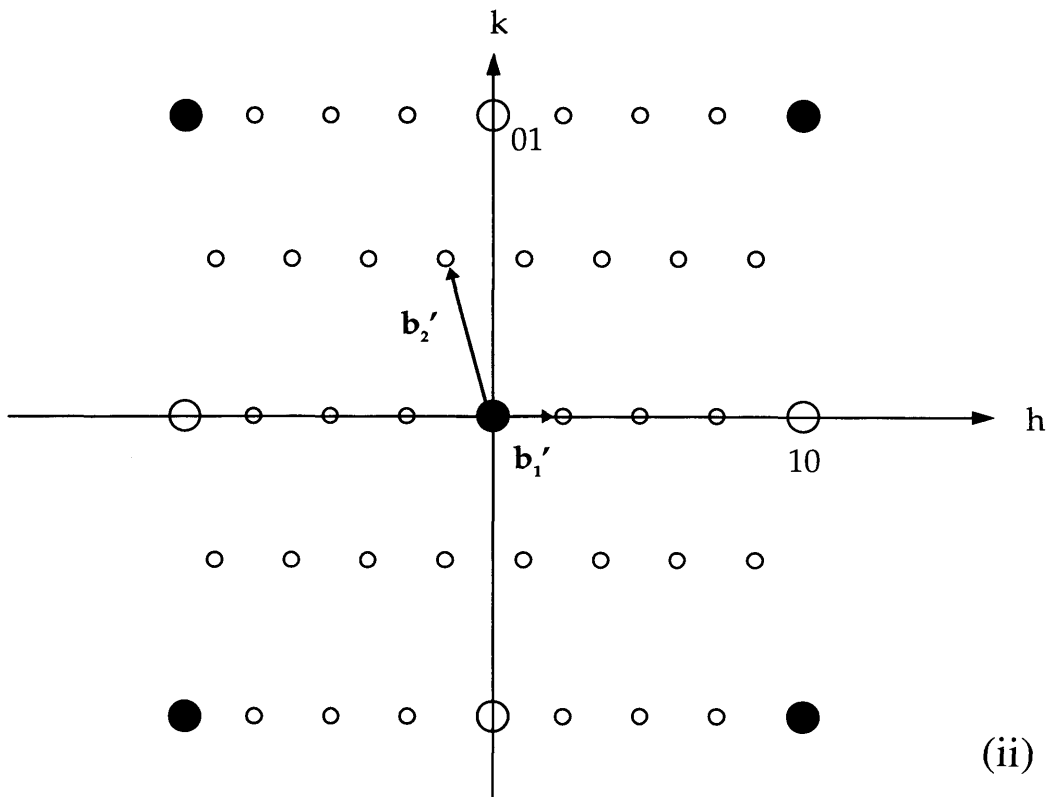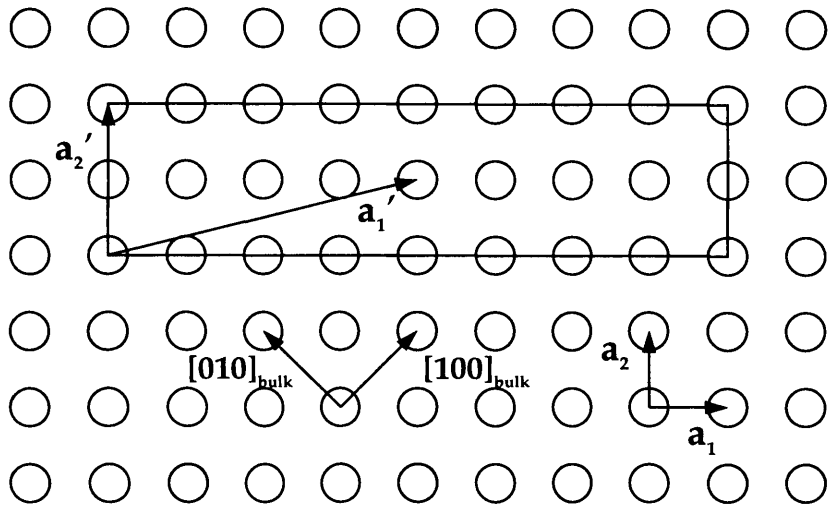
Fig. 2.3: *(i) Real space and (ii) reciprocal space lattice patterns for a c(8x2) surface.*

where a_0 is the lattice parameter 6.479Å, a_1, a_2 and a_3 define the unreconstructed bulk unit cell, a_1' and a_2' the reconstructed surface unit cell and b_i, b_i' the corresponding reciprocal space lattice.

To date, several models have been proposed for the c(8x2) reconstruction of the III-V semiconductor surfaces. Various models for GaAs(001)-c(8x2) surface are described in detail in chapter 7. However, only one model for the InSb(001)-c(8x2) reconstruction has been suggested. This model was proposed by John et al [7] from photoemission spectroscopy data. They performed analyses of In and Sb core-level photoemission intensities, as well as surface to bulk intensity ratios, for both the c(8x2) and c(4x4) reconstructions. The experimental results indicated a small, but unresolved, surface shift was present for the c(8x2) surface, though the relative intensity of the surface component could not be reliably deduced from the data. The study further considered the c(8x2) surface to be terminated by a fraction of a monolayer of In and found the coverage fell between 0.62 and 0.79 monolayers (mL). On these findings, they proposed a model terminated by 0.75 mL of indium. The model was essentially identical to an earlier model proposed by Chadi [14] for the As-rich GaAs(001)-c(2x8) reconstruction, but with group III atoms substituted for group V atoms and vice versa. The only experimental evidence for such a model was, however, the value for the indium coverage.

Data obtained from a later STM study of the same c(8x2) surface, performed by Schweitzer et al [12], was believed to be consistent with the model of John et al [7]. The features in their STM micrographs were proposed, however, to arise due to tunnelling of electrons associated with second layer atoms, and not from the uppermost layer In atoms. A further STM study performed by Varekamp et al [15], suggested the previous interpretations of the STM features were infact incorrect necessitating the need for a revaluation of the structural model of InSb(001)-c(8x2).

2.3.2 The c(4x4) reconstruction.

The InSb(001)-c(4x4) reconstruction is antimony rich and is only observed over a certain temperature range under an antimony overpressure. In contrast to the c(8x2) surface, for which there have been relatively few studies, the c(4x4) surface of the III-V semiconductors has been studied in detail [7,8,16-22]. The c(4x4) surface is highly ordered and is prepared by adsorption of the group V element in the relevant temperature range.

The reciprocal space lattice pattern is derived from the real space lattice using equations (2.4) - (2.6).

$$\mathbf{a_1}' = 2\mathbf{a_1} + 2\mathbf{a_2} = 2a_0\mathbf{i} \qquad\qquad \mathbf{b_1}' = \frac{\pi}{a_0}(\mathbf{i} - \mathbf{j}) = \frac{1}{2}\mathbf{b_1} \qquad (2.4)$$

$$\mathbf{a_2}' = 4\mathbf{a_2} = 2a_0(\mathbf{i} + \mathbf{j}) \qquad\qquad \mathbf{b_2}' = \frac{\pi}{a_0}\mathbf{j} = \frac{1}{4}(\mathbf{b_2} - \mathbf{b_1}) \qquad (2.5)$$

$$\mathbf{a_3}' = \mathbf{a_3} = a_0\mathbf{k} \qquad\qquad \mathbf{b_3}' = \mathbf{b_3} = \frac{2\pi}{a_0}\mathbf{k} \qquad (2.6)$$

The real and reciprocal space lattices are shown in fig. 2.4.

As with the c(8x2) reconstruction, the early work on the c(4x4) surface of III-V semiconductors was carried out on GaAs(001). The earlier models of the c(4x4) reconstruction are based upon a bulk-like substrate terminated by between 1 and $1^1/_2$ mL of the group V element, and were arrived at using theoretical energy based calculations [14] and RHEED/PES measurements [16]. The proposed different coverages of the c(4x4) were believed to be in consequence of its variable stoichiometry. A further study by Sauvage-Simkin *et al* [17] suggested a mixture of structures coexisted with respective surface coverages of 1/2 mL and 3/4 mL of As on top of an As-terminated bulk, accounting for the wide range of stoichiometry.
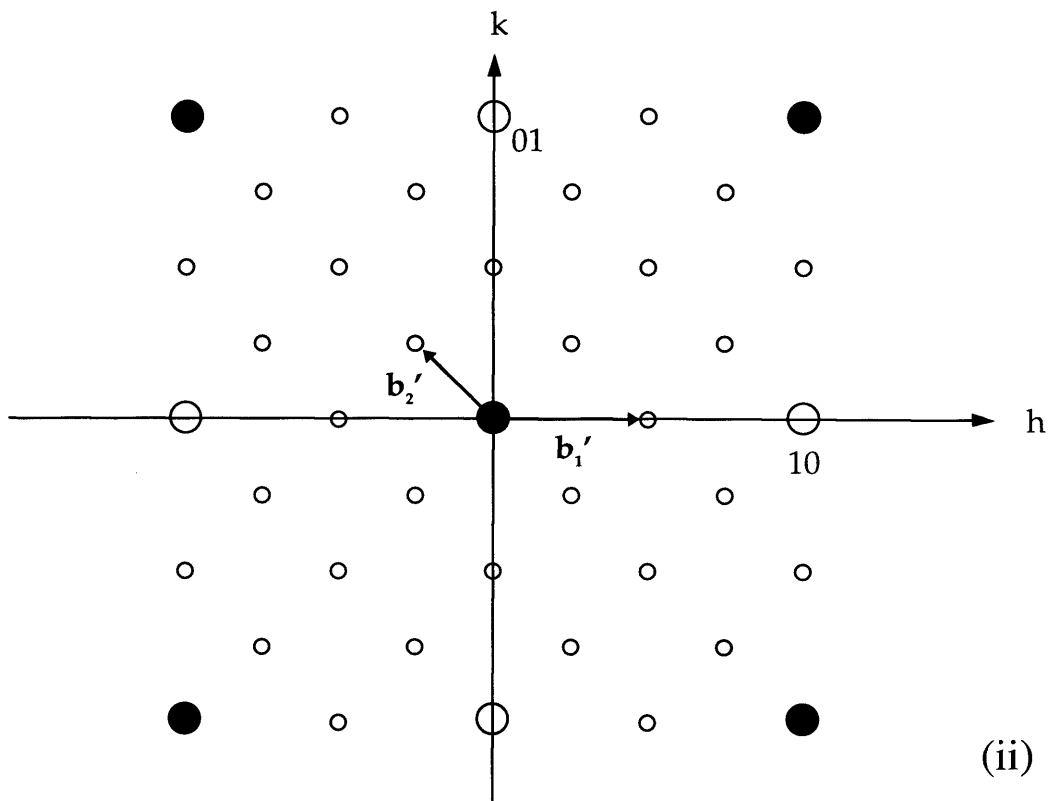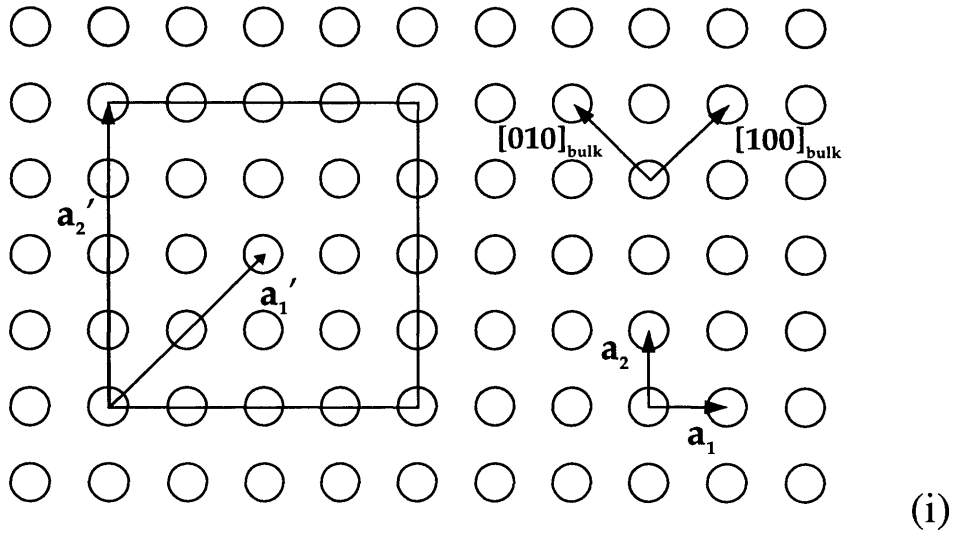
Fig. 2.4: *(i) Real space and (ii) reciprocal space lattice patterns for a c(4x4) surface.*

The earliest model for the InSb(001)-c(4x4) reconstruction was again proposed by John *et al* [7]. Their photoemission measurements revealed the c(4x4) surface was terminated by between 1.3 and 1.95 mL of Sb, and lineshape analysis showed a model terminated by $1^3/_4$ mL of Sb to be the most consistent with the data. Later STM measurements by McConville *et al* [8] were also reported to show agreement with the model proposed by John *et al* [7]. However, unlike the case for the c(8x2) reconstruction, the supporting evidence for the John model was strong as the STM images were believed to arise due to tunnelling of electrons from the uppermost layer atoms.

2.3.3 The *asymmetric*(1x3) and *pseudo*(4x3) reconstructions.

The *asymmetric*(1x3) surface is antimony rich and has been extensively studied using RHEED [5,13,23], helium atom scattering [24] and STM [8]. The early RHEED measurements showed the existence of unequally spaced third-order diffraction streaks, which lead to the asymmetric description of the reconstruction. De Oliveira *et al* [13] found that the surface was disordered and proposed the reconstruction could be explained as a superstructure resulting from a mixture of (2x4) domains. The STM micrographs of McConville *et al* [8] also clearly show that the surface has significant short range disorder.

The *pseudo*(4x3) surface has only been observed using RHEED and appears to be an intermediate surface, (hence the prefix *pseudo*), in the transition from the In-rich c(8x2) surface to the Sb-rich *asymmetric*(1x3) surface.

2.4 Summary.

The c(8x2) and c(4x4) reconstructions of the InSb(001) surface are both highly ordered and characterised by large domain sizes of up to 1000Å, whereas the *asymmetric*(1x3) and *pseudo*(4x3) reconstructions appear to be disordered.

The main attention of this thesis is therefore focused on the determination of the precise atomic structure of the c(8x2) and c(4x4) surfaces of InSb(001). Without a detailed knowledge of the surface structure there can be no proper understanding of the electronic, vibrational and chemical properties of the entire surface region which is essential for semiconductor device fabrication.

References.

[1]   V.M. Goldschmidt, Trans. Faraday Soc. **25** (1929) 253.

[2]   J.S. Blakemore, *Solid State Physics*, Cambridge University Press, 1985.

[3]   E.G. McRae, Surf. Sci. **124** (1983) 106.

[4]   A. Bar-Lev, *Semiconductor and Electronic Devices*, 2nd edn, Prentice-Hall International Inc., New Jersey, 1984.

[5]   K. Oe, S. Ando and K. Sugiyama, Jpn. J. Appl. Phys. **19** (1980) L417.

[6]   E.A. Wood, J. Appl. Phys. **35** (1964) 1306.

[7]   P. John, T. Miller and T.C. Chiang, Phys. Rev. B **39** (1989) 1730.

[8]   C.F. McConville, T.S. Jones, F.M. Leibsle and N.V. Richardson, Surf. Sci. **303** (1994) 172.

[9]   T.S. Jones, C.F. McConville, F.M. Leibsle and N.V. Richardson, Surface Review and Letters, Vol. 1, No. 4 (1994) 513.

[10]   D.K. Biegelsen, R.D. Bringans, J.E. Northrup, L.-E. Swartz, Phys. Rev. B **41** (1990) 5701.

[11]   S.L. Skala, J.S. Hubacek, J.R. Tucker, J.W. Lyding, S.T. Chou and K.Y. Cheng, Phys. Rev. B **48** (1993) 1404.

[12]   M.O. Schweitzer, F.M. Leibsle, T.S. Jones, C.F. McConville and N.V. Richardson, Surf. Sci. **280** (1993) 63.

[13]   A.G. de Oliveira, S.D. Parker, R. Droopad, B.A. Joyce, Surf. Sci. **227** (1990) 150.

[14]   D.J. Chadi, C. Tanner and J. Ihm, Surf. Sci. **120** (1982) L425.

[15]   P.R. Varekamp, M. Bjorkvist, M. Gothelid and U.O. Karlsson, Surf. Sci. **350** (1996) L221.

[16]   R. G. Jones, N.K. Singh and C.F. McConville, Surf. Sci. **208** (1989) L34.

[17]   P.K. Larsen, J.H. Neave, J.F. van der Veen, P.J. Dobson and B.A. Joyce, Phys. Rev. B **27** (1983) 4966.

[18]   M. Sauvage-Simkin, R. Pinchaux, J. Massies, P. Claverie, N. Jedrecy, J. Bonnet and I.K. Robinson, Phys. Rev. Lett. **62** (1989) 563.

[19]   A.P. Payne, P.H. Fuoss, D.W. Kisker, G.B. Stephenson and S. Brennan, Phys. Rev. B **49** (1994) 14427.

[20]   F.J. Lamelas, P.H. Fuoss, D.W. Kisker, G.B. Stephenson, P. Imperatori and S.Brennan, Phys. Rev B **49** (1994) 1957.

[21]   A.R. Avery, D.M. Holmes, J. Sudijono, T.S. Jones, B.A. Jones and G.A.D. Briggs, Phys. Rev. B **50** (1994) 8098.

[22]   P.M.Thibado, B.R. Bennett, B.V. Shanabrook and L.J. Whitman, submitted to J. Crystal Growth, July 96.

[23]   A.J. Noreika, M.H. Francombe and C.E.C. Wood, J. Appl. Phys. **52** (1981) 7416.

[24]   B.F. Mason, S. Laframboise and B.R. Williams, Surf. Sci. **258** (1991) 279.

Chapter 3.

Theory.

3.1 Introduction.

Over the last fifteen years X-ray diffraction has become established as a powerful technique for the study of surface crystallography. The atomic structure of many systems, including semiconductors [1], metal oxides [2], metal-semiconductor interfaces [3] and metal-metal interfaces [4] have been accurately determined using X-ray diffraction. Morphological information, such as surface roughness [5], can also be extracted from X-ray diffraction data.

The main advantage of using X-rays as a surface probe is that the scattering cross-section of X-rays with solid matter is small, which allows the single scattering approximation, or kinematic theory, to be used in the data analysis. Despite this small scattering cross-section, the necessary surface sensitivity required to determine the structure of the first few atomic layers can be achieved. One approach is to work at very small angles of incidence, i.e. below the critical angle of total external reflection (~0.2°). The penetration into the crystal in this case is limited to the extension of the evanescent wave, (~50Å). The difficulty is, however, the small angles involved making experimental alignment critical and reliant on very flat surfaces. More importantly, under these conditions, where there is a strong interaction with the surface, we are in a multiple scattering regime [6] and strictly kinematical theory becomes invalid. The reflected and refracted intensities as a function of the angle of

incidence, are shown in fig. 3.1(a). The variation of the X-ray penetration depth as a function of angle is also shown, fig. 3.1(b). It can be clearly be seen that the surface sensitivity decreases rapidly above the critical angle. Surface sensitivity can, however, be achieved using incident angles above the critical angle by isolating the surface in reciprocal space by recording only certain surface specific reflections. A reconstructed surface has, in general, a different periodicity, usually a simple multiple, to that of the bulk. This gives rise to fractional order rods, discussed in more detail later, which contain a scattering contribution only from the reconstructed surface. Any background from the bulk crystal, such as thermal diffuse scattering, is small and can be easily subtracted. By measuring such reflections, X-ray diffraction is only sensitive to those layers at the surface with the corresponding periodicity. This procedure is the one adopted here. The scattering from the surface region, however, is still weak, necessitating the need for a high intensity X-ray source, i.e. a synchrotron.

In this chapter the basic principles of kinematical diffraction theory are outlined, with the introduction of various related concepts.

3.2 X-ray diffraction theory.

3.2.1 Background.

The basis of the kinematical analysis is the first Born (or single scattering) approximation, which assumes the diffracted wave is made up only of singly scattered contributions. The amplitude of the scattered wave is also assumed to be small compared to that of the incident wave, true for small crystals, and the point of observation R_0 is assumed to be distant. It is noted that, as we are interested in elastic scattering, only a single wavelength of radiation need be considered. The electric field vector of a plane wave at time $t = 0$ with amplitude E_0 and wavevector k_i is given by
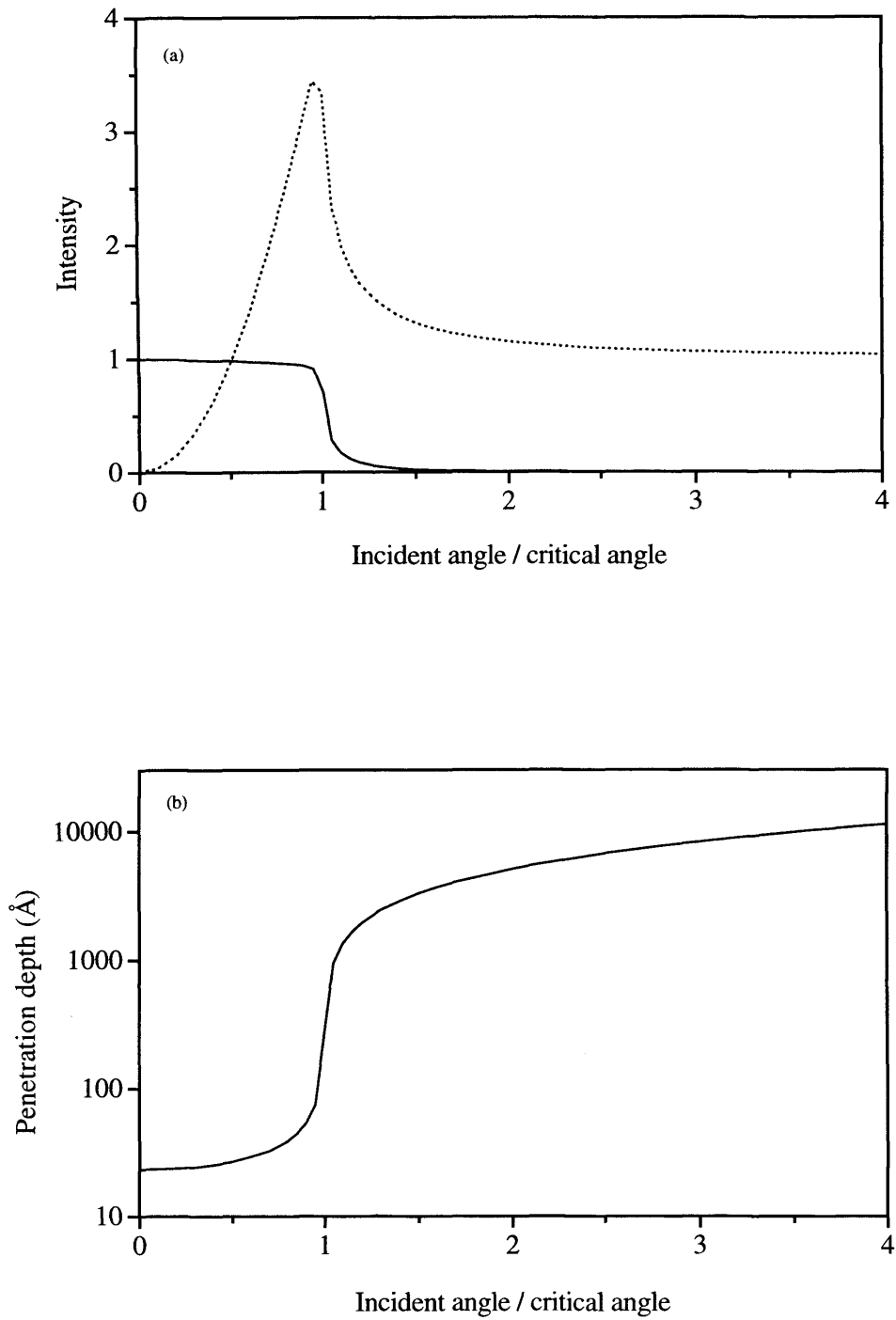
Fig 3.1: *Variation of (a) reflected intensity (solid line), refracted intensity (broken line) and (b) X-ray penetration depth as a function of the angle of incidence*

$$E(\mathbf{r}) = E_0 \exp(-i\mathbf{k}_i \cdot \mathbf{r}).$$ (3.1)

If plane waves are incident on a crystal surface, the resulting scattered field is made up of spherical waves. The Thomson formula [7,8] describes the amplitude of the emerging wave E_1 as a function of the amplitude of the incident wave E_0,

$$E_1 \exp(-i\mathbf{k}_f \cdot \mathbf{r}) = \frac{E_0}{4\pi\varepsilon_0} \frac{e^2}{mc^2} \frac{1}{R_0} \exp(i\mathbf{k}_i \cdot \mathbf{r}),$$ (3.2)

where e and m are, respectively, the electronic charge and mass. The $\dfrac{1}{R_0}$ term

describes the emergent spherical wave. The constant $\dfrac{e^2}{4\pi\varepsilon_0 mc^2} = r_e = 3\times10^{-15}$ m, implies the total scattering cross-section is small, justifying the use of kinematic theory.

It is convenient to introduce the concept of momentum transfer $\mathbf{q}$, the difference between the incident wavevector $\mathbf{k}_i$ and the final wavevector $\mathbf{k}_f$. In the case of elastic scattering $|\mathbf{k}_i| = |\mathbf{k}_f| = |\mathbf{k}| = 2\pi/\lambda$, which allows the Bragg law to be derived:

$$|\mathbf{q}| = 2|\mathbf{k}|\sin\theta.$$ (3.3)

Rearranging eq. (3.2) and using $\mathbf{q} = \mathbf{k}_f - \mathbf{k}_i$ gives

$$E_1 = \frac{E_0}{4\pi\varepsilon_0} \frac{e^2}{mc^2} \frac{1}{R_0} \exp(i\mathbf{q} \cdot \mathbf{r}).$$ (3.4)

It can be seen that $\mathbf{q}$ is an important variable in X-ray diffraction, being in equations for both the experimental in-plane scattering angle 2θ, and the theoretical scattering amplitude E_1. The typical scattering geometry for an X-ray diffraction experiment is shown in fig. 3.2.

The atomic form factor can now be introduced and is also defined in terms of $\mathbf{q}$:

$$f(\mathbf{q}) = \int_{-\infty}^{\infty} \rho(\mathbf{r})\exp(i\mathbf{q}.\mathbf{r})d\mathbf{r} . \tag{3.5}$$

The atomic form (or atomic scattering) factor is essentially the Fourier Transform (FT) of the electronic charge density for a single atom. We can in turn define the structure factor $F(\mathbf{q})$, the sum of scattering contributions from all the atoms in one unit cell. If there are N atoms in the unit cell then

$$F(\mathbf{q}) = \sum_{j=1}^{N} f_j(\mathbf{q})\exp(i\mathbf{q}.\mathbf{r}_j) , \tag{3.6}$$

where j accounts for the different atom types within the unit cell. Alternatively, it is convenient to define $F(\mathbf{q})$ in terms of the electron density $\rho(\mathbf{r})$. Defining $\rho(\mathbf{r})$ as the sum of the contributions to the electron density from all the atoms in the unit cell we can write

$$F(\mathbf{q}) = \int \rho(\mathbf{r})\exp(i\mathbf{q}.\mathbf{r})d\mathbf{r} . \tag{3.7}$$
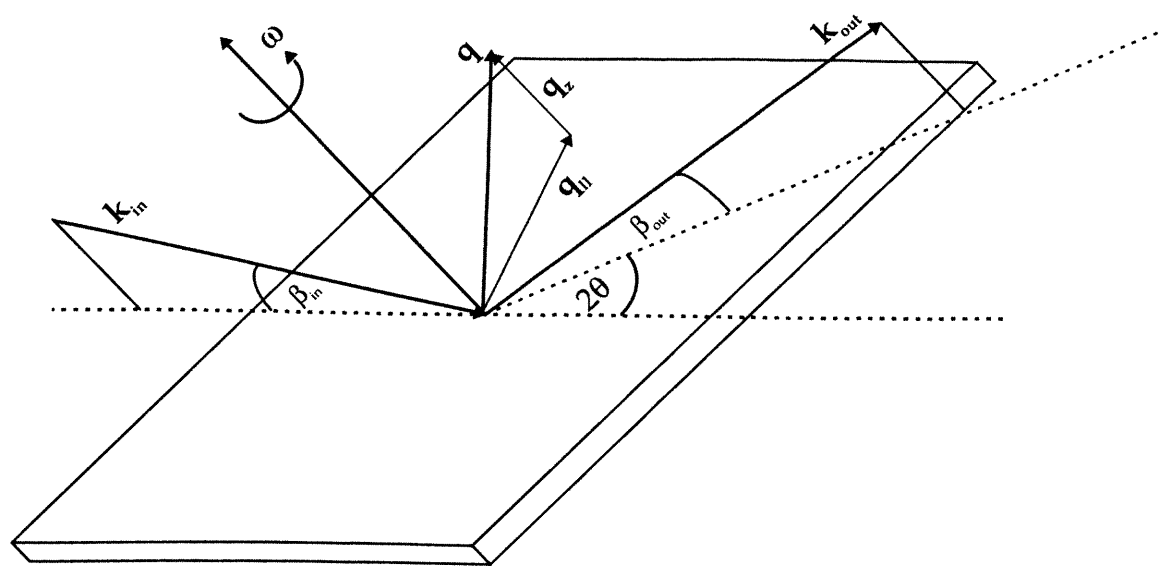
Fig. 3.2: *Schematic diagram showing a typical surface X-ray scattering ge*

F($\mathbf{q}$) is therefore the FT of the electron density in one unit cell and, conversely, the electron density is the inverse FT of the structure factor. F($\mathbf{q}$) is, however, a complex number,

$$F(\mathbf{q}) = |F| \exp i\alpha \qquad (3.8)$$

of which only the amplitude is measurable. The phase factor α is not an observable. Several methods can, however, be used to solve this so-called phase problem [9]. They include direct methods, the heavy atom method and anomalous scattering. The method adopted here employs the Patterson function [10] which allows the phase problem to be ignored and is discussed later.

3.2.2 X-ray scattering by a crystal lattice.

The structure factor gives the contribution to the scattering from a single unit cell. However, for the scattering from a three-dimensional crystal we need to consider an infinite crystal lattice with N_1, N_2 and N_3 unit cells along the three orthogonal crystal axes which are defined by the vectors $\mathbf{a}_1$, $\mathbf{a}_2$ and $\mathbf{a}_3$. The position of an atom is given by $\mathbf{R}_n + \mathbf{r}_j$, where

$$\mathbf{R}_n = n_1 \mathbf{a}_1 + n_2 \mathbf{a}_2 + n_3 \mathbf{a}_3 \ , \qquad (3.9)$$

n_i is an integer and $\mathbf{r}_j$ is the position of the jth atom with respect to the origin. The total scattered wave amplitude, E_{tot} , is equal to the sum of the scattering amplitudes of each unit cell :

$$E_{tot} = E_0 \frac{e^2}{4\pi\varepsilon_0 mc^2} \frac{1}{R_0} F(\mathbf{q}) \sum_{n_1}^{N_1-1} \sum_{n_2}^{N_2-1} \sum_{n_3}^{N_3-1} \exp(i\mathbf{q}.\mathbf{R}_n) \qquad (3.10)$$

The above term is a geometric sum and the summation term can be evaluated using the standard result to give

$$\sum_{n=0}^{N-1} \exp(i\mathbf{q}.n\mathbf{a}) = \frac{1 - \exp(i\mathbf{q}.N\mathbf{a})}{1 - \exp(i\mathbf{q}.\mathbf{a})} \qquad (3.11)$$

The intensity of the scattered beam is equal to the square modulus of the above and it is this quantity in which we are interested experimentally. The intensity can therefore be written as:

$$\left| \sum_{n=0}^{N-1} \exp(i\mathbf{q}.n\mathbf{a}) \right|^2 = \frac{\sin^2(N\mathbf{q}.\mathbf{a}/2)}{\sin^2(\mathbf{q}.\mathbf{a}/2)} \qquad (3.12)$$

It can be seen that the above summation, (eq. 3.10), will yield a maximum value when :

$$\mathbf{q}.\mathbf{R} = 2\pi m \qquad (3.13)$$

where m is an integer.

However, for the summation to converge, we need to define the reciprocal lattice parameters, $\mathbf{b}_i$, by:

$$\mathbf{a}_i.\mathbf{b}_j = 2\pi\delta_{ij} \qquad \text{with} \qquad \mathbf{q}=(h\mathbf{b}_1 + k\mathbf{b}_2 + l\mathbf{b}_3) \qquad (3.14)$$

which allows eq. (3.13) to be rewritten in the form of the Laue conditions :

$$\mathbf{q}_1.\mathbf{a}_1 = 2\pi h$$

$$\mathbf{q}_2.\mathbf{a}_2 = 2\pi k \qquad (3.15)$$

$$\mathbf{q}_3.\mathbf{a}_3 = 2\pi\lambda$$

where h, k and λ are the Miller indices.

All three of the Laue conditions have to be satisfied for diffraction to occur. Any set of three integers will satisfy the Laue conditions and this gives rise to an array of discrete points in reciprocal space. This is the reciprocal lattice and the diffracted intensity is non zero everywhere except at the points lying on the lattice. The corresponding lattice parameters, using eq. (3.14), can be written as:

$$\mathbf{b}_1 = 2\pi\frac{\mathbf{a}_2 \times \mathbf{a}_3}{\mathbf{a}_1.\mathbf{a}_2 \times \mathbf{a}_3} \qquad \mathbf{b}_2 = 2\pi\frac{\mathbf{a}_3 \times \mathbf{a}_1}{\mathbf{a}_1.\mathbf{a}_2 \times \mathbf{a}_3} \qquad \mathbf{b}_3 = 2\pi\frac{\mathbf{a}_1 \times \mathbf{a}_2}{\mathbf{a}_1.\mathbf{a}_2 \times \mathbf{a}_3}. \qquad (3.16)$$

3.3 Finite Temperature effects.

The Debye-Waller Factor.

Up to this point we have ignored the effect on temperature on the crystal lattice. At finite temperatures the atoms do not occupy definite positions, but actually vibrate about an equilibrium position. This causes a reduction in the scattered intensity which increases as a function of temperature. The intensity is lost as thermal diffuse scattering, and the intensity drop is described by the Debye-Waller factor which can be included in eq. (3.6):

$$F(\mathbf{q}) = \sum_j f_j(\mathbf{q}) \exp\left[\frac{-B_j \mathbf{q}^2}{16\pi^2}\right] \exp(i\mathbf{q}.\mathbf{r_j}), \qquad (3.17)$$

where B_j is the Debye-Waller factor.

Assuming the Debye-Waller factor to be isotropic we can write

$$B = 8\pi\langle u^2 \rangle, \qquad (3.18)$$

where $\langle u^2 \rangle$ is the mean-square atomic vibrational amplitude.

3.4 Surface X-ray diffraction.

Surface X-ray diffraction is distinguished from its bulk counterpart, described in the previous section, because of the fact that only a few atomic layers contribute to the diffracted intensity. Atoms at the surface of a crystal have a reduced coordination

and are in a different environment compared to those deep in the bulk. On the creation of a surface, the three-dimensional periodicity of the crystal is terminated which gives rise to a higher surface free energy. This energy is lowered, in general, by two effects:

i) reconstruction: the surface atoms move laterally to form a surface with a periodicity different to that of the underlying bulk, leading to a larger surface unit cell; and

ii) relaxation: the surface atoms move in the direction perpendicular to the surface to minimise the surface energy and also the elastic strain produced by surface reconstruction.

During the analysis, it is therefore convenient to think of the crystal to be composed of two distinct regions: the surface region, containing the uppermost atomic layers in which reconstruction and/or relaxation are significant; and the bulk region which we consider to be a perfect crystal infinite in two directions and truncated by a flat surface.

The total scattered amplitude is determined by adding the calculated scattered amplitudes of the bulk and surface regions.

3.4.1 Surface scattering.

The crystal surface can be thought of as a region with an infinite area (a_1, a_2 tend to infinity), but with a finite thickness, typically a few atomic layers, in the direction along the surface normal a_3. In consequence, the Laue condition, eq. (3.15), for the direction perpendicular to the surface can now be relaxed and may assume any real value. Constructive interference may therefore occur at non-integer values of the perpendicular momentum transfer, which gives rise to so-called diffraction rods. The scattering from the bulk is still present and leads to bulk Bragg peaks superposed on the diffraction rods at regular intervals. These diffraction rods are more commonly known as crystal truncation rods (CTRs). Their existence is a direct consequence of

the termination of a bulk crystal by a surface [11]. Experimentally, one measures the intensity of the CTR as a function of perpendicular momentum transfer λ, allowing a profile of the CTR to be established.

An important rod is the (00), or specular, rod. This is, in effect, an amplitude profile made up of contributions to the scattering solely in the direction perpendicular to the surface. Using equations (3.10) and (3.15) we can describe the contribution to the surface scattering given by the specular rod using a summation:

$$E_{surf}(\lambda) = F_{surf}(\lambda) \sum_{n=0}^{N-1} \theta_n \exp(-i2\pi\lambda Z_n / a_3),$$

(3.19)

where N is the number of surface layers, θ_n is the fractional coverage and Z_n is the height of each layer from the bulk terminated crystal.

All CTRs containing bulk Bragg peaks are, by definition, integer order rods, that is, they occur at integral values of h and k. For a reconstructed surface the in-plane surface unit cell is larger than that of the bulk, the periodicity in the surface plane being an integer multiple of that of the bulk. This gives rise to fractional order rods, which occur periodically between the integer order rods. Bulk scattering is forbidden at all points along the fractional order rods, which implies fractional rods contain contributions only from the reconstructed surface. A schematic diagram of a reconstructed surface and the corresponding reciprocal space lattice pattern is shown in fig. 3.3. The surface unit cell in fig. 3.3(a) has a periodicity that is four times greater than that of the bulk along the x-axis. Due to the inverse relationship between real and reciprocal space, this gives rise to fractional order diffraction rods at quarter order positions along the h-axis.

31

4x1 surface
unit cell

bulk unit cell

z

x

(a)

λ

bulk Bragg peak

2

crystal truncation rod

0   h

1   2

fractional order rod

-2

(b)
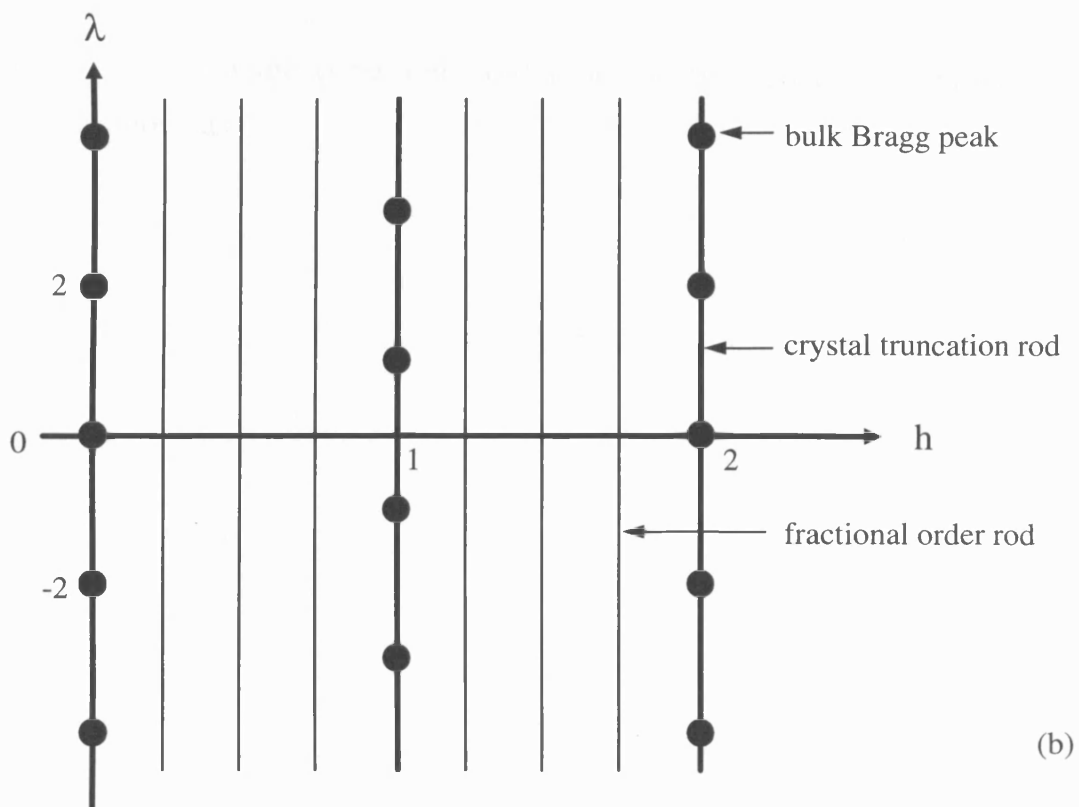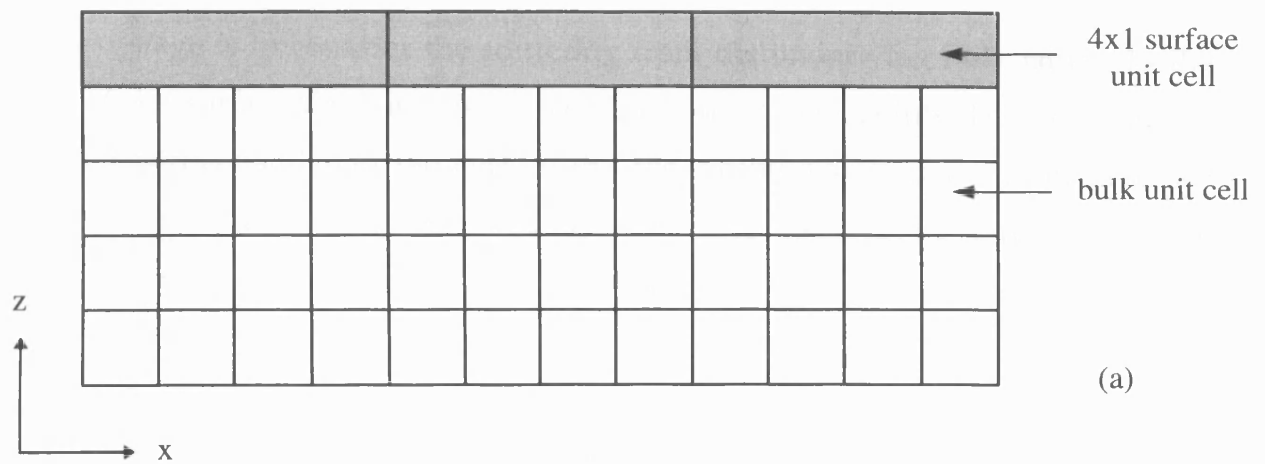
Fig 3.3: *Schematic diagram of (a) real space model and (b) the corresponding reciprocal space lattice pattern, for a reconstructed surface.*

3.4.2 Bulk scattering.

The next stage is to consider the scattering from the underlying bulk lattice. In the plane of the surface the scattering is confined to discrete points. However, in the direction perpendicular to the surface the rod profile varies periodically. We are therefore more interested in the perpendicular λ direction and, by setting $h = k = 0$, we can ignore the in-plane terms in eq. (3.10) which reduces to

$$E_{bulk}(\lambda) = E_0 \frac{e^2}{4\pi\varepsilon_0 mc^2} \frac{1}{R_0} F(\mathbf{q}) \sum_{n_3=0}^{N_3-1} \exp(i2\pi\lambda n_3). \qquad (3.20)$$

By employing the Laue conditions and ignoring the constant prefactors, we can rewrite the above as

$$E_{bulk}(\lambda) = F_{00}(\lambda) \sum_{n_3=0}^{N_3-1} \exp(i2\pi\lambda n_3). \qquad (3.21)$$

An attenuation factor also needs to be included to account for the fact that the X-rays are absorbed by the crystal:

$$E_{bulk}(\lambda) = F_{00}(\lambda) \sum_{n_3=0}^{N_3-1} \exp(i2\pi\lambda n_3) \exp\left(\frac{-n_3 a_3}{\mu}\right), \qquad (3.22)$$

where μ is the X-ray penetration depth.

The attenuation factor makes the summation convergent. If $N_3 \rightarrow \infty$, the standard result for a geometric progression yields the result:

$$E_{bulk}(\lambda) = F_{00}(\lambda) \frac{1}{1 - \exp(i2\pi\lambda)\exp(-a_3/\mu)} \; . \tag{3.23}$$

Equation (3.23) gives the diffracted intensity as a function of perpendicular momentum transfer for the bulk terminated crystal, that is, the diffraction rod profile.

For X-rays, $\mu \gg a_3$, and eq. (3.23) can be rewritten as

$$E_{bulk}(\lambda) = F_{00}(\lambda) \frac{1}{1 - \exp(i2\pi\lambda)} = F_{00}(\lambda) \frac{-\exp(i\pi\lambda)}{2\sin\pi\lambda} \; . \tag{3.24}$$

However, using the above equation, it can be seen that at integer values of λ, which coincide with the position of the bulk Bragg peaks, $E(\lambda) \rightarrow \infty$. This is clearly physically incorrect and implies that at the bulk Bragg peaks we need to use the full form of the above equation, eq. (3.23), that is, we need to take account of absorption. There is also a phase change of π at each Bragg peak. Halfway between the Bragg peaks the phase is zero and the scattering amplitude is just $\frac{1}{2}F_{00}(\lambda)$. This is the anti-Bragg position and is the position of maximum sensitivity to surface growth [12].

3.4.3 Total scattering.

The total scattered amplitude from the crystal is the sum of the bulk and surface contributions:

$$E_{hk}^{total}(\lambda) = E_{hk}^{bulk}(\lambda) + E_{hk}^{surf}(\lambda) \qquad (3.25)$$

At the fractional order rod positions, there is no bulk contribution, and $E_{total} = E_{surf}$. However, close to the bulk Bragg peaks, the bulk scattering term dominates and $E_{total} \approx E_{bulk}$. At integer order positions away from the Bragg peaks, there is interference between the two scattering amplitudes. This contribution varies as we move along the CTR between the Bragg peaks. A schematic diagram showing the interference between the bulk and surface scattering amplitudes is shown in fig. 3.4.

3.5 Integrated Intensity.

As stated earlier it is the scattered intensity, rather than the amplitude, that we are interested in experimentally. The scattered intensity is proportional to the square modulus of the amplitude, $E_{tot}^* E_{tot}$, and using eq. (3.10) we obtain for the intensity

$$I(\mathbf{q}) = I_0 \frac{r_e^2}{R_0^2} F^*(\mathbf{q})F(\mathbf{q}) \sum_{n_1=0}^{N_1-1}\sum_{n_2=0}^{N_2-1}\sum_{n_3=0}^{N_3-1} \exp i\mathbf{q}.(n_1\mathbf{a}_1 + n_2\mathbf{a}_2 + n_3\mathbf{a}_3) \sum_{n_1=0}^{N_1-1}\sum_{n_2=0}^{N_2-1}\sum_{n_3=0}^{N_3-1} \exp{-i\mathbf{q}}.(n_1\mathbf{a}_1 + n_2\mathbf{a}_2 + n_3\mathbf{a}_3)$$

$$(3.26)$$

where r_e is the classical electron radius and I_0 is the incident flux. The above term can be simplified by considering the amplitude from only a single layer of atoms of length L_x and L_y along the directions of $\mathbf{a}_1$ and $\mathbf{a}_2$ respectively.
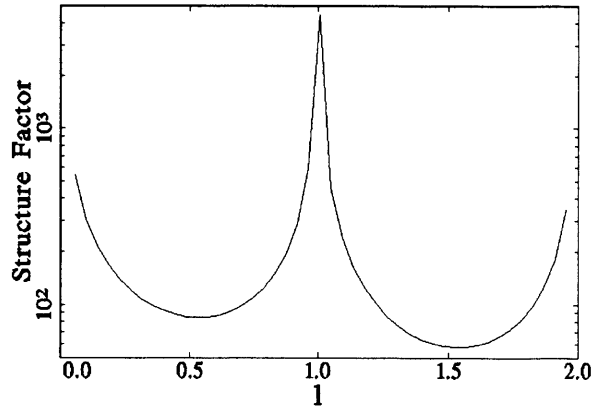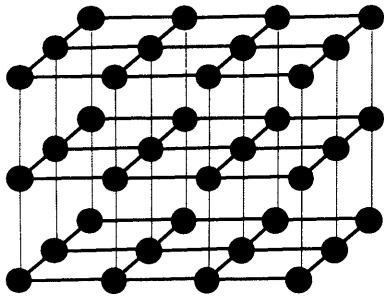
Fig 3.4(a): *The scattering amplitude, $E_{hk}^{bulk}(l)$, from a truncated simple cubic lattice.*
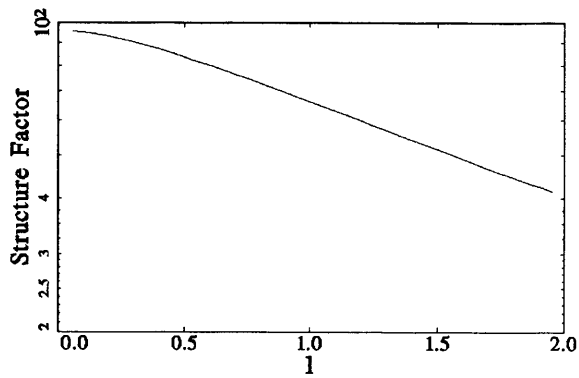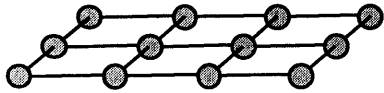

Fig. 3.4(b): *The scattering amplitude, $E_{hk}^{surface}(l)$, from a simple surface lattice.*
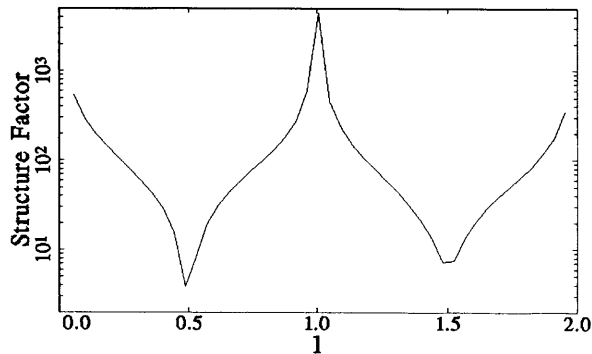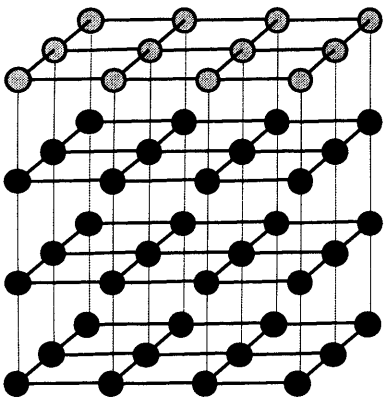
Fig 3.4(c): *The total scattering amplitude, $E_{hk}^{total}(l) = E_{hk}^{bulk}(l) + E_{hk}^{surface}(l)$, from a bulk*

solid as in a) having a surface b).

The third summation term can now be ignored and using eq. (3.12) in eq. (3.26) the scattered intensity becomes

$$I(\mathbf{q}) = I_0 \frac{r_e^2}{R_0^2} |F_{hkl}|^2 \frac{\sin^2 \pi h L_x / a_1}{\pi^2 h^2} \frac{\sin^2 \pi k L_y / a_2}{\pi^2 k^2} , \qquad (3.27)$$

where $L_x/a_1 = N_1$ and $L_y/a_2 = N_2$. However the above intensity is not, in fact, an observable unless the crystal is perfect, the incident X-ray beam is perfectly monochromatic and the detector acceptance is a δ-function in reciprocal space. This is quite clearly not the case in a real experiment. In practice, we measure a quantity called the integrated intensity. This is achieved by rotating the crystal about the surface normal, over a region in reciprocal space, until all the diffracted intensity for a specific reflection is recorded by the detector. This gives rise to a diffraction peak with a finite width in reciprocal space.

To derive the theoretical integrated intensity we first need to consider the differential scattering cross-section:

$$\left| \frac{d\sigma}{d\Omega} \right| = \frac{I(\mathbf{q})dA}{I_o d\Omega} , \qquad (3.28)$$

where the incident flux, I_0 is defined as the number of photons per unit time per unit area and the area element $dA = R_0^2 d\Omega$. The differential scattering cross-section, therefore, reduces to

38

$$\left|\frac{d\sigma}{d\Omega}\right| = \frac{I(\mathbf{q})R_0^2}{I_0} \ . \tag{3.29}$$

Using eq. (3.27) yields for the differential scattering cross-section:

$$\left|\frac{d\sigma}{d\Omega}\right| = r_e^2 \left|F_{hkl}\right|^2 \frac{\sin^2 \pi h L_x / a_1}{\pi^2 h^2} \frac{\sin^2 \pi k L_y / a_2}{\pi^2 k^2} \tag{3.30}$$

The experimental geometry to measure the integrated intensity of a reflection is shown schematically in fig. 3.5. The detector accepts radiation over an interval $\Delta\psi$ in the parallel in-plane direction and $\Delta\gamma$ in the perpendicular out-of-plane direction. Diffraction only occurs when the Ewald sphere cuts a diffraction rod. The integrated intensity is obtained by integrating the scattered intensity over time and the angular acceptance of the detector:

$$I_{int} = \int I_0 \left|\frac{d\sigma}{d\Omega}\right| dt d\psi d\gamma \ . \tag{3.31}$$

Using the geometry in fig. 3.5 we can define the area element of integration in terms of dt and $d\psi$ as

$$dA = k\omega q_{\parallel} \cos\theta dt d\psi \ , \tag{3.32}$$

39
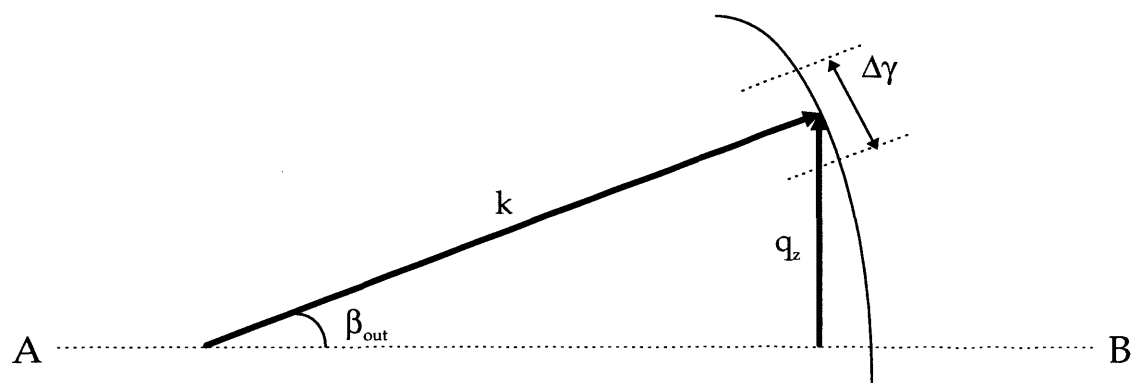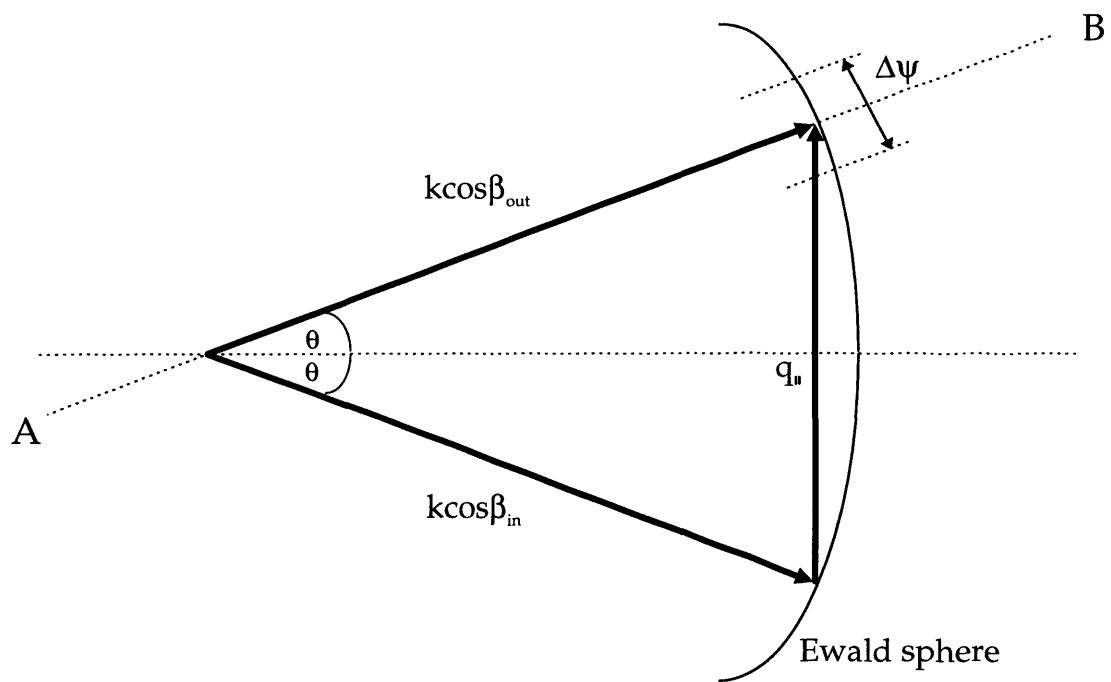
Fig. 3.5: *The geometry used in deriving the integrated intensity of an X-ray reflection: (a) plan view and (b) side view along the line AB.*

where ω is the speed of rotation of the crystal. Defining the area element in terms of h and k as

$$dA = \frac{4\pi^2}{A_u} dhdk , \qquad (3.33)$$

and using $k = 2\pi/\lambda$, we can write

$$dtd\psi = \frac{4\pi^2}{A_u} \frac{1}{k\omega q_{\parallel} \cos\theta} dhdk = \frac{\lambda^2}{\omega A_u} F_{Lor} dhdk , \qquad (3.34)$$

where F_{Lor} is the Lorentz factor,

$$F_{Lor} = \frac{k}{q_{\parallel} \cos\theta} = \frac{1}{\cos\beta \sin 2\theta} \qquad (3.35)$$

which accounts for the angle at which the Ewald sphere intersects a diffraction rod.

Thus substituting eq. (3.30) and (3.34) in eq. (3.31) we get for the integrated intensity:

$$I_{int} = r_e^2 \frac{I_0}{\omega} \frac{\lambda^2}{A_u} F_{Lor} \int \frac{\sin^2 \pi hL_x}{\pi^2 h^2} dh \int \frac{\sin^2 \pi kL_y}{\pi^2 k^2} dk \int |F_{hkl}|^2 d\gamma . \qquad (3.36)$$

Assuming $|F_{hkl}|$ to be constant ,the above can be evaluated to give

$$I_{int} = r_e^2 \frac{I_0}{\omega} \frac{\lambda^2}{A_u} F_{Lor} \frac{L_x}{a_1} \frac{L_y}{a_2} |F_{hkl}|^2 \Delta\gamma \qquad (3.37)$$

where $L_x L_y$ is the illuminated surface area A. Eq. (3.37) is the final term for the integrated intensity of any particular reflection. It corresponds to a cut through a diffraction rod at any λ value.

Throughout the chapter we have largely neglected the vector nature of E. We can account for this by including a polarisation factor P in the above giving:

$$I_{int} = r_e^2 \frac{I_0}{\omega} \frac{\lambda^2}{A_u} A F_{Lor} P |F_{hkl}|^2 \Delta\gamma \qquad (3.38)$$

In general the illuminated surface area A, the Lorentz factor F_{Lor} and the polarisation factor P, will be different for different reflections. Important correction factors need to be applied to the integrated intensity to account for this. The forms of A, F_{Lor} and P are discussed in further in chapter 4.

3.6 Structure Determination.

The Patterson Function.

It can be seen from eq. (3.17) that all positional information about the atomic structure of the surface unit cell is contained within the structure factor; the square of the structure factor $|F_{hkl}|^2$ being deduced from the measured integrated intensity, eq. (3.38). Structure determination of a measured sample involves the direct comparison of the experimental structure factors with the same set of theoretical structure factors, calculated using a theoretical model.

We already know , eq. (3.7), that the structure factor can be expressed as the Fourier transform of the electron density of a single unit cell. Unfortunately, it is not possible to directly measure the electron density experimentally, as only the amplitude of the structure factor can be determined. From eq. (3.8) it can be seen the total structure factor also contains a phase component which makes it a complex number. This phase problem is overcome by making use of the Patterson function.

The Patterson function can be directly obtained from the experimental data and yields model-independent real space information relating to the surface atomic structure. It is defined as:

$$P(\mathbf{r}) = \int \rho(\mathbf{R})\rho(\mathbf{r}+\mathbf{R})d\mathbf{R} \qquad (3.39)$$

and is the autocorrelation function of the electron density of the unit cell. Since the electron density can be written as

$$\rho(\mathbf{r}) = \frac{1}{V}\sum_{hkl} F_{hkl}\, \exp i(\mathbf{q}\cdot\mathbf{r}), \qquad (3.40)$$

43

the Patterson function becomes

$$P(\mathbf{r}) = \frac{1}{V^2} \int \sum_{hkl} \sum_{h'k'l'} F_{hkl} F_{h'k'l'} \exp i(\mathbf{q'} \cdot \mathbf{r}) \exp i(\mathbf{q} + \mathbf{q'}) \cdot \mathbf{R} d\mathbf{R} \qquad (3.41)$$

Now as the only non-zero integrals are where $h' = -h$, $k' = -k$ and $\lambda' = -\lambda$, eq. (3.41) reduces to

$$P(\mathbf{r}) = \frac{1}{V} \sum_{hkl} F_{hkl} F_{\overline{hkl}} \exp{-i(\mathbf{q} \cdot \mathbf{r})}, \qquad (3.42)$$

Since $F_{hkl} F_{\overline{hkl}}$ produces the same result for both hkl and $\overline{hkl}$ eq. (3.42) takes the general form of the Patterson function:

$$P(\mathbf{r}) = \frac{1}{V} \sum_{hkl} |F_{hkl}|^2 \cos 2\pi(hx + ky + \lambda z) \qquad (3.43)$$

Setting $\lambda = 0$ gives the two dimensional Patterson function:

$$P(\mathbf{r}) = \frac{1}{V} \sum_{hk0} |F_{hk}|^2 \cos 2\pi(hx + ky) \qquad (3.44)$$

44

The Patterson function is usually displayed as a contour plot (see for example fig. 5.3). In our analysis, only fractional-order reflections have been used to calculate $P(r)$ since they contain information solely about the reconstructed surface unit cell. Even though this leads to distortions in the Patterson function [13,14], a positive peak in a Patterson map still corresponds to an interatomic vector in the surface unit cell. The Patterson function is therefore a useful starting point in the determination of the structure of the surface unit cell as it does not assume a model of the structure.

References.

[1]   R.G. van Silfhout, J.F. van der Veen, C. Norris and J.E. Macdonald, Faraday Discuss. Chem. Soc. **89** (1990) 169.

[2]   T. Koyano, E. Kita, K. Ohshima and A. Tasaki, J. Phys. C. **32** (1991) 5921.

[3]   P.B. Howes, C. Norris, M.S. Finney, E. Vlieg and R.G. van Silfhout, Phys. Rev. B **48** (1993) 1632.

[4]   J.A. Meyer, J. Vrijmoeth, H.A. van der Vegt, E. Vlieg and R.J. Behm, Phys. Rev. Lett. **72** (1994) 3843.

[5]   N. Jones, C. Norris, C.L. Nicklin, P. Steadman, J.S.G. Taylor, C.F. McConville and A.D. Johnson, Appl. Surf. Sci. **123/124** (1998) 141.

[6]   G.H. Vineyard, Phys. Rev. B **26** (1982) 4146.

[7]   B.E. Warren, *X-ray Diffraction*, Addison-Wesley, Reading, 1969.

[8]   D.J. Jackson, *Classical Electrodynamics*, Wiley, New York, 1975.

[9]   I.K. Robinson and D.J. Tweet, Rep. Prog. Phys. **55** (1992) 599.

[10]   A.L. Patterson, Phys. Rev. **46** (1934) 372.

[11]   I.K. Robinson, Phys. Rev B **33** (1986) 3830.

[12]   C. Norris, Phil. Trans. R. Soc. London, A **344** (1990) 557.

[13]   J. Bohr, R. Fiedenhans'l, M. Nielsen, M. Toney, R.L. Johnson and I.K. Robinson, Phys. Rev. Lett. **54** (1985) 1275.

[14]   R. Fiedenhans'l, Surf. Sci. Rep. **10** (1989) 105.

Chapter 4.

Experimental.

4.1   Introduction.

The essential prerequisite for the study of atomically clean semiconductor surfaces is an ultra high vacuum (UHV) environment, as the sample surface must remain free of contamination. The substrate of interest throughout this thesis is the InSb(001) semiconducting surface and, more importantly, it is the clean surface reconstructions in which we are interested. As the reconstructed surfaces are polar, they are fairly reactive and any background contamination can lead to rapid deterioration in the quality of the reconstruction.

The UHV system used in the experiments was the Leicester University X-ray Chamber (LUXC) which was designed for *in-situ* SXRD measurements [1]. The environmental chamber allows complementary techniques such as low energy electron diffraction (LEED) and Auger electron spectroscopy (AES) to be used for surface preparation. The sample preparation procedures are described in more detail later.

The weak interaction of X-rays with matter, coupled with the grazing incidence angles required for surface sensitivity, implies a high intensity X-ray source and a long time period are needed to perform a complete study. The X-ray radiation was therefore provided by a synchrotron source.

A six-circle diffractometer [2,3] was used to orient the sample and to define the scattering vector used in the structural analysis of the crystal surface. All relevant experimental apparatus, including the six-circle diffractometer, are described in this chapter.

As mentioned earlier, the integrated intensity is the quantity which we measure experimentally. The deduction of the structure factors from the integrated intensities, including the application of appropriate correction factors, is also outlined here.

4.2   The UHV Chamber.

4.2.1   LUXC.

The experimental measurements were made using the LUXC environmental chamber [1]. The chamber, coupled to the six-circle diffractometer is shown schematically in fig. 4.1. A photograph of the experimental apparatus is also shown in plate 4.1. The main chamber is in effect an eight inch diameter stainless steel cylinder which has several ports built into its body. Each port is directed towards the centre of the sample which is mounted at one end of the main chamber. The ports accommodate the different pieces of surface science equipment used in sample preparation. They include an electron gun and a hemispherical analyser used for AES, an argon gun used for ion bombardment of freshly loaded substrates, and Knudsen cell evaporation sources [4] used for the deposition of materials onto the sample. At the other end of the main chamber (opposite the sample) there is an eight inch port to which either a rear view LEED optics or a load-lock sample transfer system can be mounted.

Incident X-rays enter the chamber through a large Be window, which subtends 200° in the vertical plane and 30° out of plane, before being scattered by the sample. The scattered X-rays leave the chamber through the same Be window and are collected by the solid state germanium detector.

out of plane
detector assembly

aluminium
beams

detector

Huber 3010 slits

detector beam pipes

Huber 3011 slit mounted onto
MF04CC Microcontrole
translation stages

metal vapour source

rear view LEED
or
sample prep/transfer system

electron analyser

$400 \, ls^{-1}$
Ion pump

Be
window

δ

ω

ϕ

χ

sample
rod

α
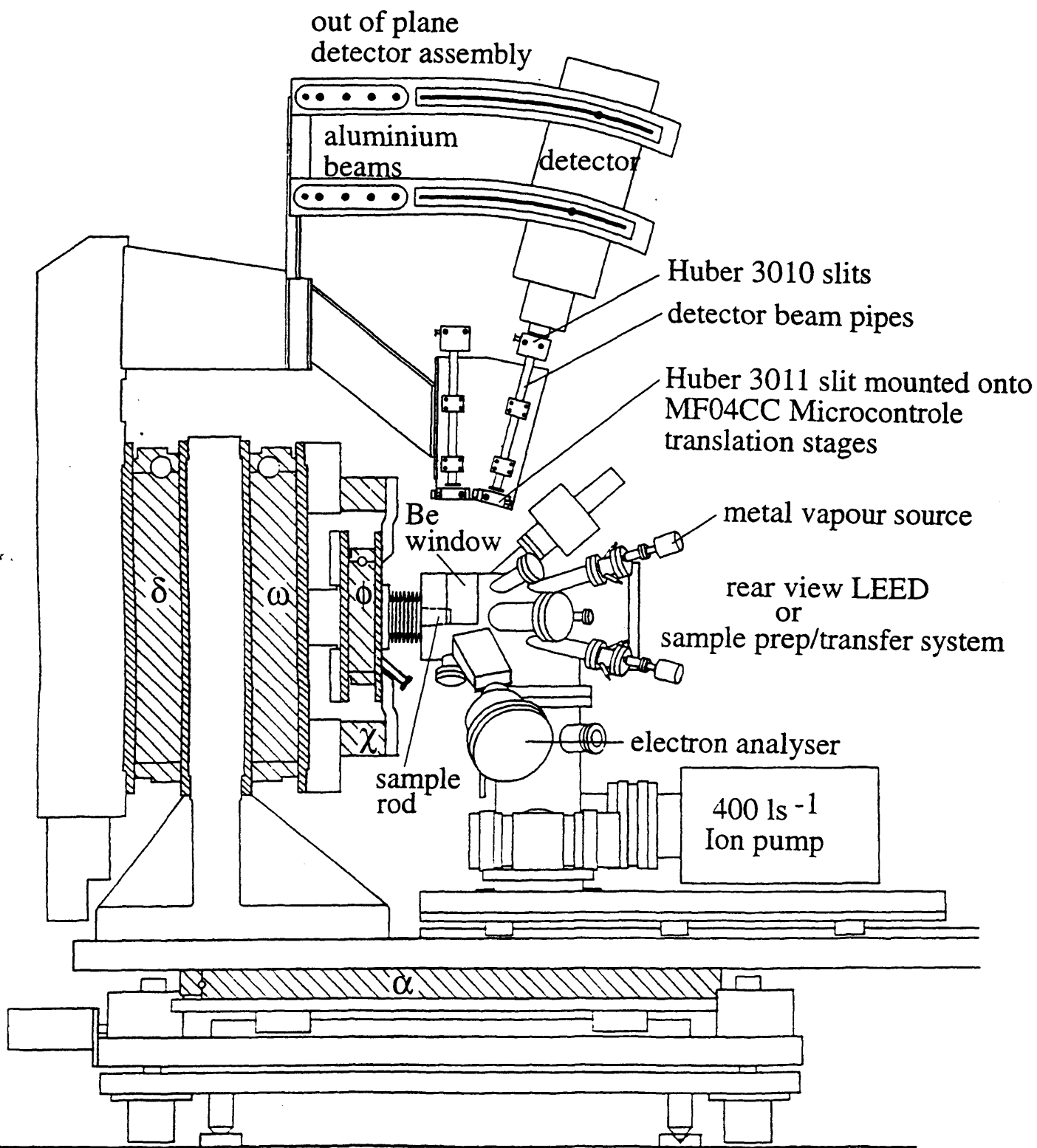
Fig. 4.1: *Schematic of the LUXC environmental chamber used for SXRD measurements.*

Plate 4.1: *Photograph of the experimental set-up used for surface X-ray diffraction at Daresbury Laboratory.*
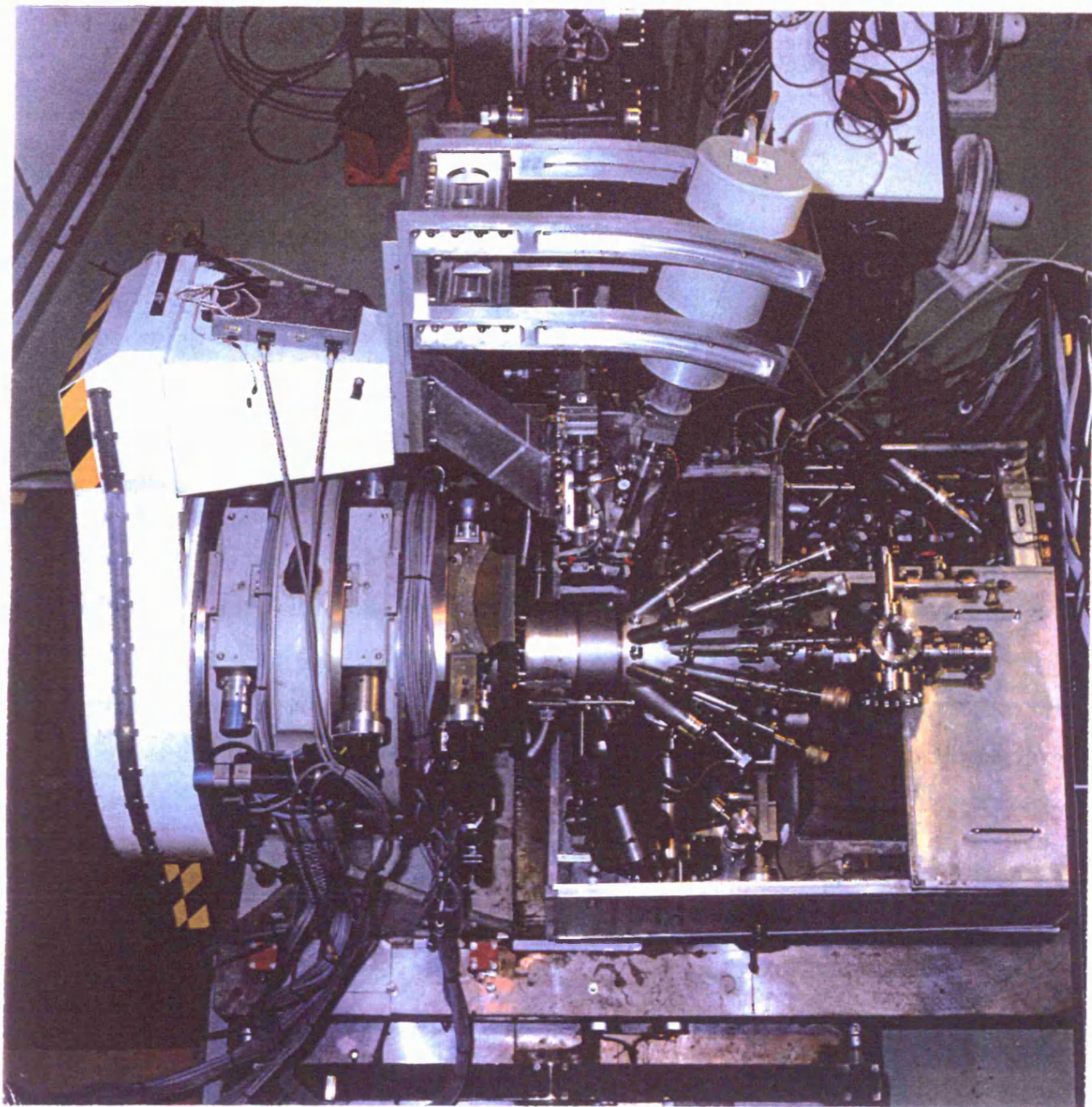
To obtain UHV, the chamber is first rough pumped from atmosphere down to $\sim 10^{-4}$ mbar using an external turbomolecular pump backed by a small rotary pump. The external pumping unit is then valved off and the chamber pumped by a 400 ls^{-1} Balzers turbomolecular pump and a liquid nitrogen cooled titanium sublimation pump (TSP). After baking the chamber for $\sim$ 18 hrs at 150°C and thorough outgassing of all components, a chamber pressure of $< 1x10^{-10}$ mbar is maintained using a Varian 400 ls^{-1} ion pump.

4.2.2 The Rotary seal.

Prepared InSb(001) substrates (section 4.3.1) are mounted on a purpose built sample heater housed in a differentially pumped rotary seal and bellows. This allows the sample to be rotated by the diffractometer without any measurable deterioration of the vacuum inside the main chamber.

The rotary seal was specially constructed at Leicester and is based on earlier designs [5,6]. It is, in essence, a stainless steel tube which can rotate through a full 360° inside three viton sealing rings which separate two differentially pumped stages. The low vacuum section is pumped from atmosphere down to $\sim 10^{-3}$ mbar by a small rotary pump. The high vacuum section is then pumped down to $\sim 10^{-6}$ mbar using a 50 ls^{-1} Balzers turbomolecular pump.

The sample heater is housed in a stainless steel tube at the end of the rotary feedthrough. The sample surface stands proud of the entire assembly allowing grazing incidence diffraction to be performed. The sample manipulator also allows efficient sample cooling down to liquid nitrogen (LN$_2$) temperature and sample transfer, in which both the sample and sample heater are transferred together.

4.3 Sample preparation.

4.3.1 InSb substrates.

The InSb(001) samples used in the experiments were cut from large pre-polished Sb-capped or uncapped wafers. The purchased, two inch, InSb wafers were polished on both sides and supplied by MCA Wafer Technology. The following recipe for cleaning the InSb wafers was developed by and carried out under the supervision of Dr A. D. Johnson at DRA Malvern, Worcs, UK.

The wafers were first degreased in hot solvents which were poured into separate soxhlets in the following order :

      i)   Acetone,

      ii)   Trichloroethylene   and

      iii)   Isopropyl Alcohol.

The wafers were placed in each soxhlet for thirty minutes. All chemicals used were the Aristar research grade. Extreme care was taken at all times to avoid contamination, with PTFE tweezers being used to handle the samples. The degreased substrates were now ready for an acetic etch, the wafers being given a two minute etch in the following mixture :

      i)   Nitric acid   4ml,

      ii)   Hydrofluoric acid   2ml,

      iii)   Acetic acid   2ml and

      iv)   Distilled water   20ml.

The acids were mixed in the order listed and stirred thoroughly. The mixture was placed in a PTFE beaker in a constant temperature bath set at 42°C. The mixture was left in the bath for 10 minutes. The final stage involved a lactic etch in which the wafers were given a two minute etch at room temperature in the following mixture of acids :

     i)   Lactic acid   50ml,

     ii)   Nitric acid   8ml and

     iii)   Hydrofluoric acid   2ml.

The acids were again mixed in the order listed and spun for 10 minutes. The spinner was rinsed in distilled water to prevent corrosion or contamination, a fresh batch of etch was used for each substrate.

Following the lactic etch the substrates were left in running distilled water for several minutes, after which they were placed into boiling methanol and stood for three minutes. The substrates were finally blown dry using a dry nitrogen jet.

The clean samples were next loaded into a UHV chamber in which they were capped with buffer layers of antimony. The protective overlayer was grown at room temperature, at which the sticking coefficient of antimony is non-zero allowing an amorphous cap (a few hundred Å) to be built up [7]. All samples used in the structural analysis (chapters 5, 7) and the phase transition study (chapter 6) were cut from wafers that were Sb-capped using the method outlined above. For the cleaning work (chapter 8) the samples used were uncapped.

InSb(001) samples with dimensions 8x8 mm^2 were cut from the larger wafers. The wafers cleave cleanly along the two orthogonal crystal planes, the directions of which are indicated by flats on the wafer edges. As the InSb samples were too thin to have steps cut into their edges, it was necessary to mount the semiconductor samples

InSb(001) wafer

[001]

8 mm

8 mm

0.5 mm

1 mm

10 mm

8 mm

Molybdenum block

Thin In layer
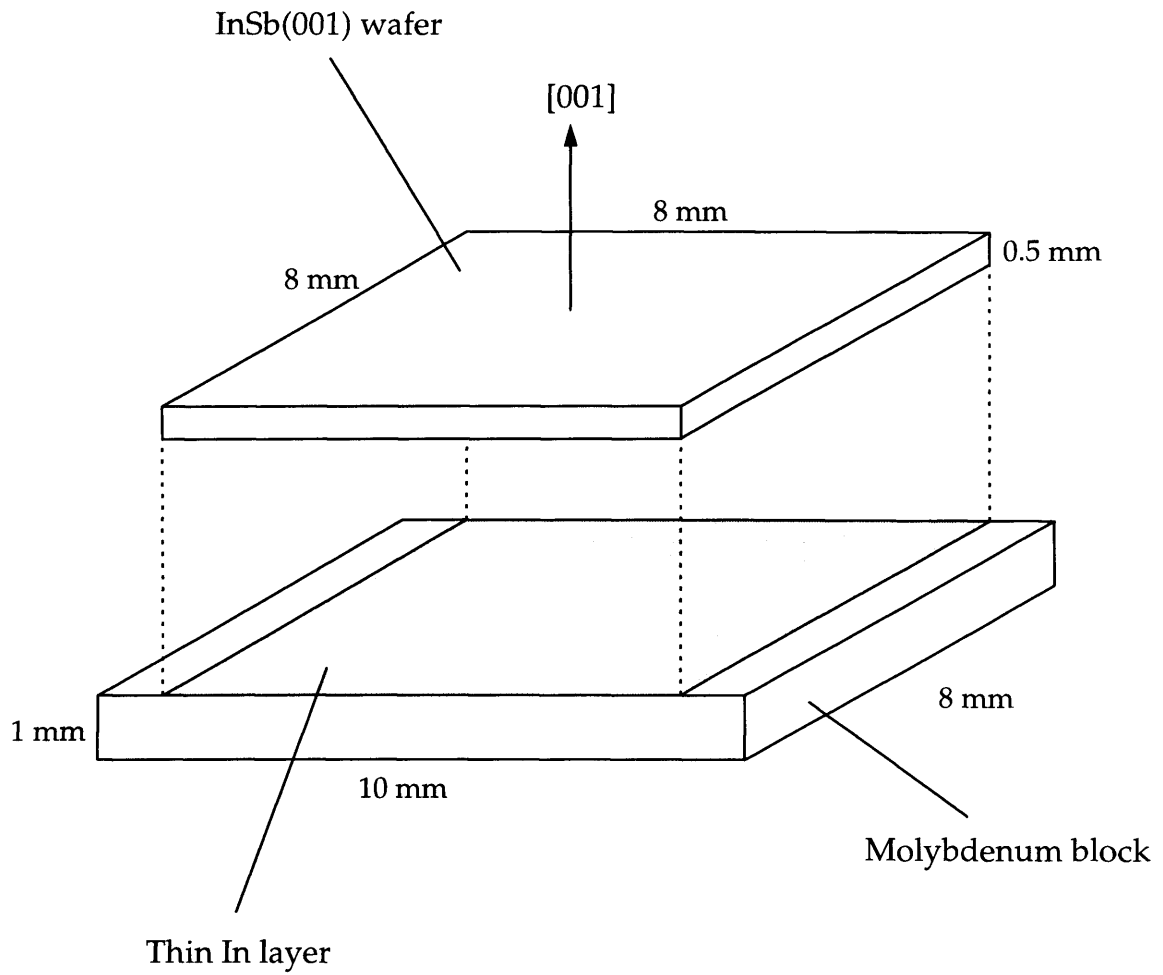
Fig. 4.2: *Schematic diagram of the indium bonding of an InSb*
sample to a Mo backing plate

onto backing plates. The molybdenum backing plate had dimensions $8 \times 10 \times 1 mm^3$ and was cleaned in successive ultrasonic baths of hot water, acetone and isopropyl alcohol. The block was electropolished [8] and RF heated at 800°C in a vacuum of 10^7 mbar.

The InSb(001) sample was then bonded to the Mo block using a thin In (99.9999% purity) seal. This procedure was carried out on a hotplate at ~ 150°C (the melting point of In). The bonded substrate was then left to cool to room temperature. The dimensions of the sample are shown in fig. 4.2.

After placing the samples in a UHV environment the InSb samples were treated with one cycle of argon ion bombardment (800v Ar^+ ions, $1.5\mu Acm^{-2}$, 1hr) and annealing (T_s = 350°C) to remove the thick native oxide layer. The cleanliness and atomic order of the surface were checked using a combination of SXRD, LEED and AES.

4.3.2 Auger electron spectroscopy.

Auger electron spectroscopy can be used to obtain information about the overall surface stoichiometry. Electrons with an energy of 2keV are emitted from a VG LEG31 electron gun. The electrons are incident on the sample surface and cause excitation in the surface region. The ejected Auger electrons are focused on to the entrance slit of a VSW HA50 hemispherical analyser. The analyser is mounted on a retractable bellows below the level of the detector support. Only electrons with a certain energy, the pass energy, will emerge from the analyser. The resulting electrons are collected by a channeltron electron multiplier.

The amplified Auger signal is differentiated by a phase sensitive lock-in amplifier to suppress the broad background signal. The analyser voltage, and therefore the pass energy, are externally controlled via a digital analogue converter by a personal computer. This arrangement allows not only the chemical status of the surface to be measured, but also the Auger signal of the substrate or adsorbate atoms to be
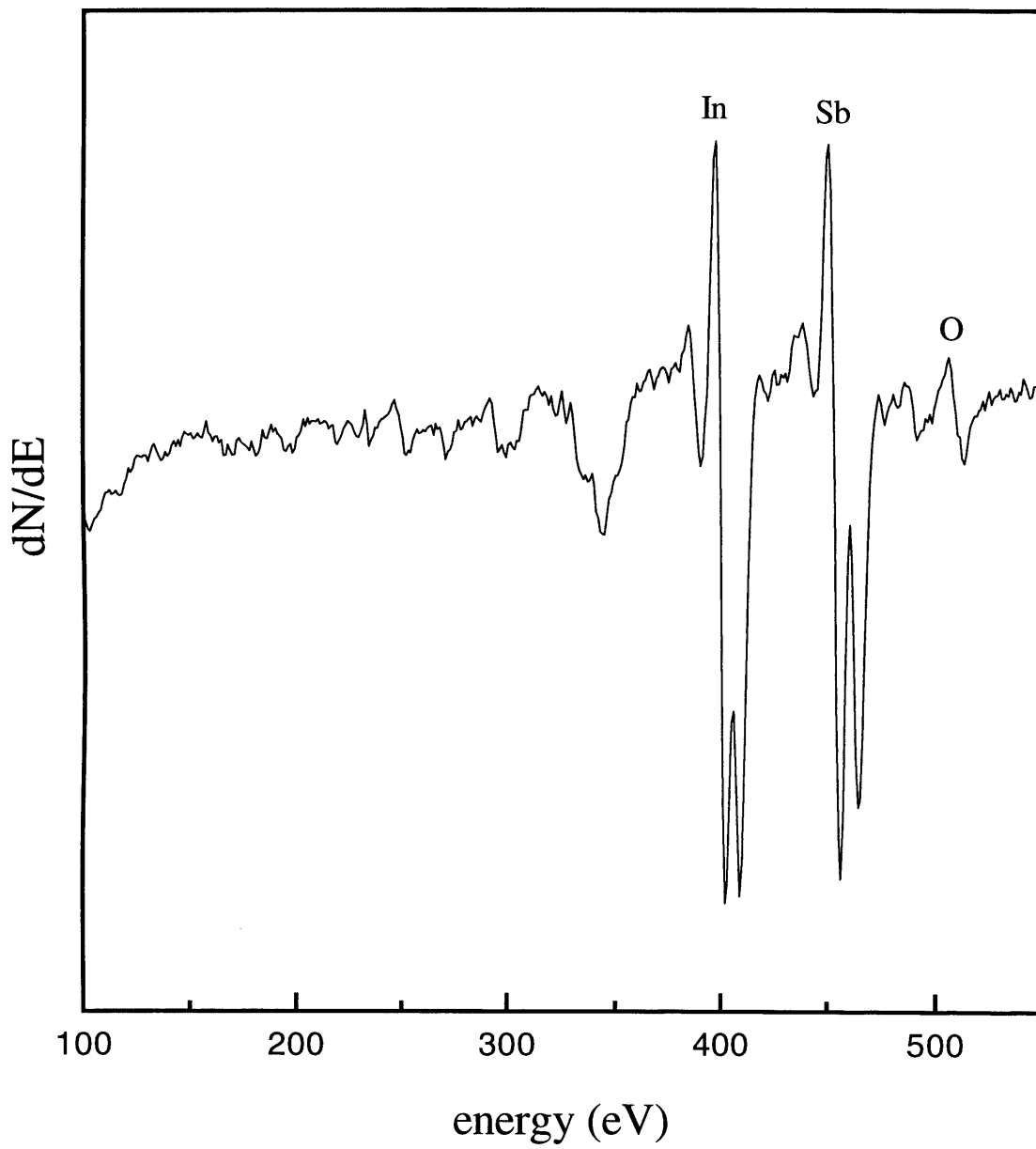
Fig 4.3: *AES spectrum of a partially cleaned InSb(001) sample.*

monitored during growth. An Auger spectrum for a partially cleaned InSb(001) surface is shown in fig. 4.3. The In and Sb peaks arise from MNN transitions.

4.4 Surface X-ray Diffraction measurements.

4.4.1 Synchrotron radiation.

The X-ray measurements described in this thesis were performed at synchrotron radiation facilities due to the high intensity of radiation they provide. The beamline stations used were the wiggler station 9.4 at the Synchrotron Radiation Source (SRS), Daresbury and the W12 beamline at DCI, LURE, Paris, both of which are specifically set-up for surface X-ray diffraction.

Both machines are storage rings which accumulate and store electrons that have been pre-accelerated and transported from an injection system. The injection system used at the SRS consists of five stages [9]:

i)   an electron gun to create a stream of electrons;

ii)   a primary acceleration stage consisting of a linear accelerator (linac) where the stream of electrons are bunched into short electron packages (bunches) and accelerated to approximately half the speed of light, with a corresponding energy of 12 MeV;

iii)   a secondary acceleration stage, or booster synchrotron, where the bunches are accelerated at constant speed ($v \sim c$) to higher energies ($\sim$ 600 MeV);

iv)   an extraction system from the injector composed of fast switching magnets (kickers), special bending magnets and a transfer line to the storage ring

v)   a system for injection into the storage ring composed of bending magnets and kickers.

The storage ring itself is shown schematically in fig. 4.4 and consists of a series of straight sections joined together to form a closed loop in which a high vacuum is maintained. When a sufficient number of electrons have been accumulated in the storage ring the energy of the stored electrons is raised from 600 MeV to the final energy of 2 GeV.

Bending dipole magnets are situated at each corner of the storage ring, each of which produce a field in the vertical direction. Electrons passing through the magnetic field are therefore bent through a circular arc by means of the Lorentz force. The electrons then pass through a straight section consisting of focusing quadrupole magnets separated by so-called drift spaces. The effect of the quadrupole magnets is to keep the electron bunch ($\sim 10^{10}$ electrons) close together in the plane perpendicular to the direction of motion. There are usually many electron bunches in the storage ring at any one time. The SRS has up to 160 electron bunches in the storage ring which are $\sim$ 50-100 ps in length and 2ns apart. The number of electron bunches in the storage ring can also be reduced in order to create a 'gapped' beam ($\sim$ 130 continuous bunches). Each electron bunch also loses energy due to betatron oscillations both in the horizontal and the vertical plane. To keep the electron numbers from decaying rapidly each bunch receives an electromagnetic 'kick' from a radio frequency (RF) cavity to increase the energy of the electron bunch, keeping the electrons in the circular orbit.

The trajectory of the electron bunches is therefore a closed circular orbit in which the electrons are accelerated at speeds very close to that of light (v $\sim$ c). This has the effect of changing the energy distribution of the electrons from the classical toroidal distribution to a highly collimated beam concentrated in the direction of the electron velocity (in the frame of reference of the laboratory). The beam current, however, will gradually decay due to loss of electrons. It is therefore necessary to refill the storage ring by re-injecting electrons approximately every twenty four hours. The SRS at Daresbury Laboratory has a beam energy of 2.0 GeV and a typical beam current of 200 mA.

Bending magnet

Electron bunch

Storage ring

Focusing magnet

Synchrotron
radiation

20 - 40 mrad

Experimental
Station
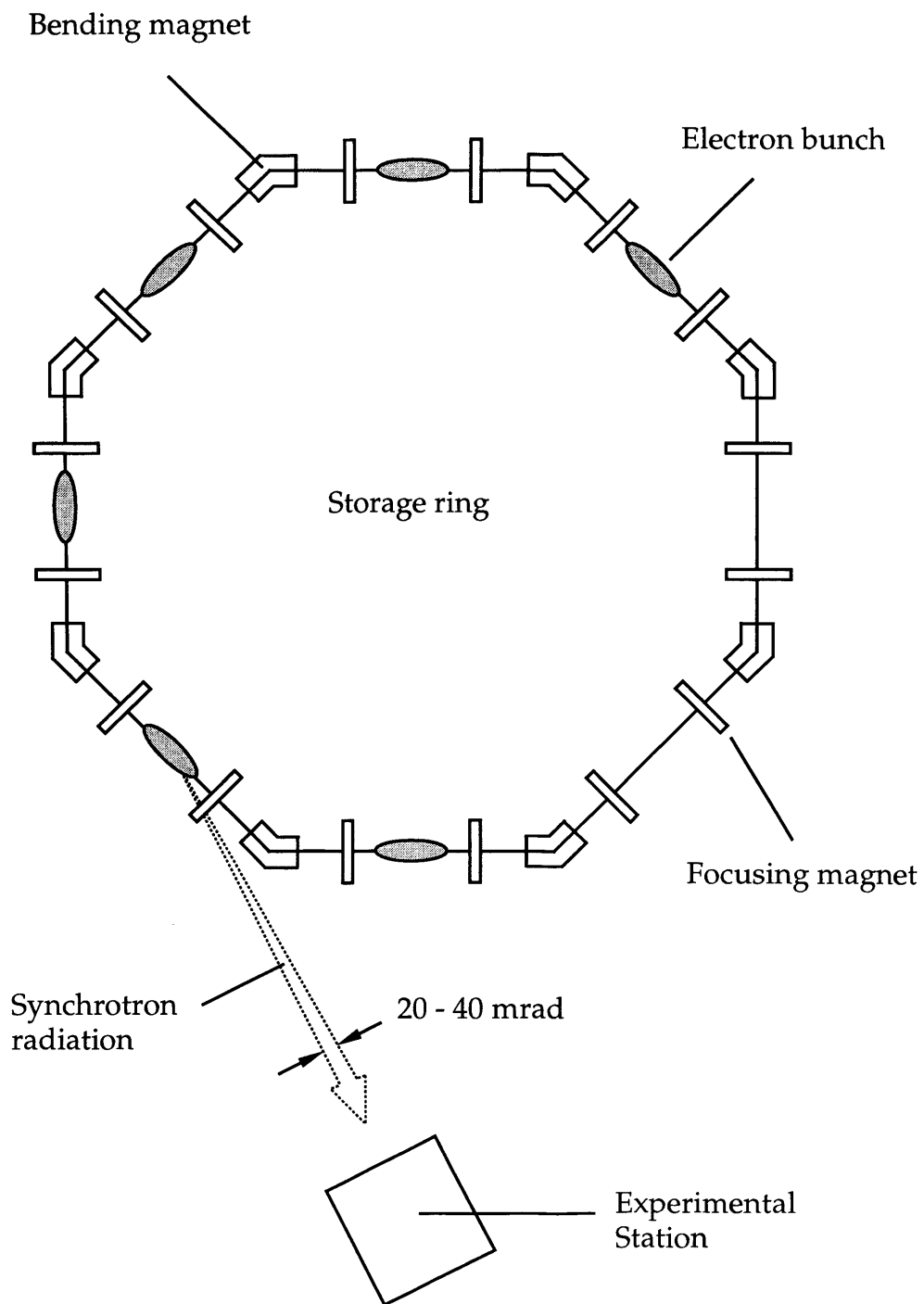
Fig. 4.4: *Schematic diagram of a storage ring. Some of the electron bunches have been omitted to represent a gapped beam.*

4.4.2   X-ray Beamline 9.4.

Insertion devices placed along the straight sections of the storage ring are used to deliver the radiation from the storage ring into purpose built beamline stations. Beamline 9.4 is shown schematically in fig. 4.5 and uses radiation provided by an insertion device known as a wiggler. A wiggler magnet is a succession of alternating polarity magnetic poles that produce a field of 5.0T in the vertical plane and hence a sinusoidally varying field in the horizontal plane. The magnet is designed such that the alternating electron deflections cancel out and no net bending of the beam is produced. This allows the magnet to be placed in a straight section of the storage ring with little disturbance to the electron orbit. As the magnetic field in the wiggler is higher than the bending magnetic field, the electrons are forced to follow a path whose radius of curvature is smaller than that of the bending magnets, resulting in a radiation spectrum shifted to lower wavelengths, and therefore, higher energies.

The emergent fan of radiation from the wiggler is collimated by an arrangement of a water-cooled mask and four-jaw slits, before being focused by a platinum coated toroidal mirror onto a water cooled channel cut Si(111) monochromator [10]. This allows X-rays of a certain wavelength (in the continuous range 0.7 - 1.8Å) to be selected. A further set of four-jaw slits defines a 1 x 1 mm^2 beam that is incident on the sample.

A small air-filled ion chamber placed at the end of the beamline is used to measure the total incident flux. This allows the X-ray measurements to be normalised for variations in the incident intensity. The X-ray beam passes through a Be window and is incident on the sample. The scattered radiation passes through the opposite side of the same Be window and is collected by a liquid nitrogen cooled, solid state Ge detector. The scattered beam is defined by two sets of four-jaw slits, separated by an evacuated pipe capped with mylar windows, placed in front of the detector.

Ge solid-state
detector

ion chamber
beam monitor

beam-defining
slits

water-cooled,
channel-cut
monochromator

collimating
slits
sample

4 jaw
slits

4 jaw slits

toroidal
mirror

filter

wiggler
source

water-cooled
mask

38.0 m   36.5 m   18.2 m   0 m
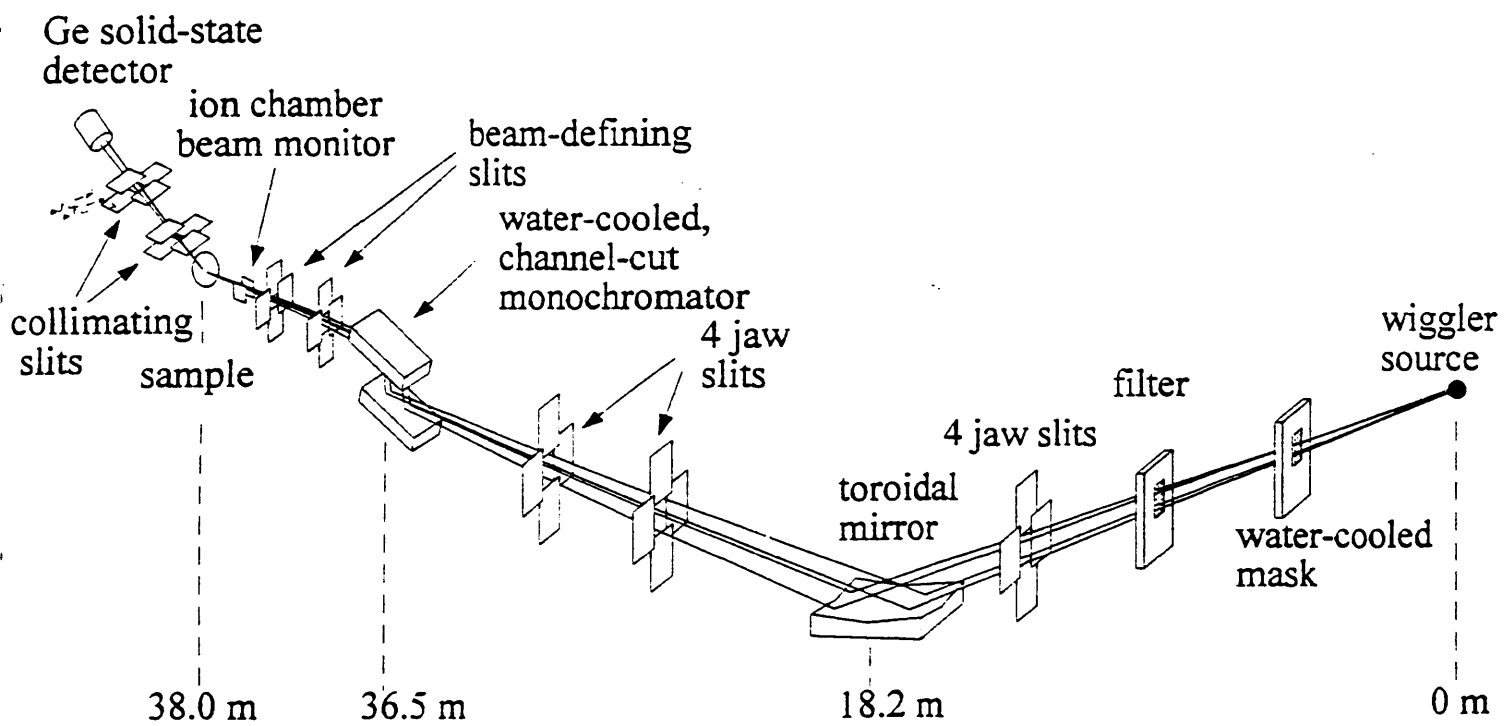
Fig. 4.5: *Schematic of beamline 9.4 of the SRS. Daresbury.*

4.5 Diffractometry.

4.5.1 Six-Circle Diffractometer.

The six-circle diffractometer used for the SXRD measurements is shown schematically in fig. 4.6. A vertical scattering geometry is necessary because of near 100% horizontal polarisation of the X-ray beam which would cause near zero values of intensity at scattering angles close to 90°.

The position and orientation of the sample is directly controlled by use of the χ, ϕ and ω circles. The χ-circle is not a full circle and actually consists of two arcs limited to movements of approximately $\pm 20°$. The χ-arcs are used to rock the sample. The ϕ-circle rotates the sample through a full 360° about its surface normal. The ω-circle moves the χ and ϕ circles simultaneously. The movement of the entire diffraction table is controlled by the horizontal α-circle allowing the angle of incidence to be set independently. The δ and γ circles are used to control the position of the detector. The δ-circle rotates the detector about the horizontal axis of the diffractometer and the γ-circle rotates it about a vertical axis. The γ-circle is not a full circle, but allows the detector to be moved to a second position, 15° along an arc centred on the sample in a direction perpendicular to the surface. Two partially overlapping of reciprocal space can therefore be measured, so the γ-circle effectively increases the accessible region of reciprocal space along the out-of-plane λ-axis, the necessary sensitivity required to measure the extended out-of-plane region being provided by the χ and α circles. The α-circle has a resolution of ten thousand steps per degree, and the other four motorised circles a resolution of eight thousand steps per degree. The diffractometer is computer controlled and offers highly accurate positioning of the sample. In addition, the x and z axes of the sample are computer driven with a resolution of one thousand steps per millimetre.
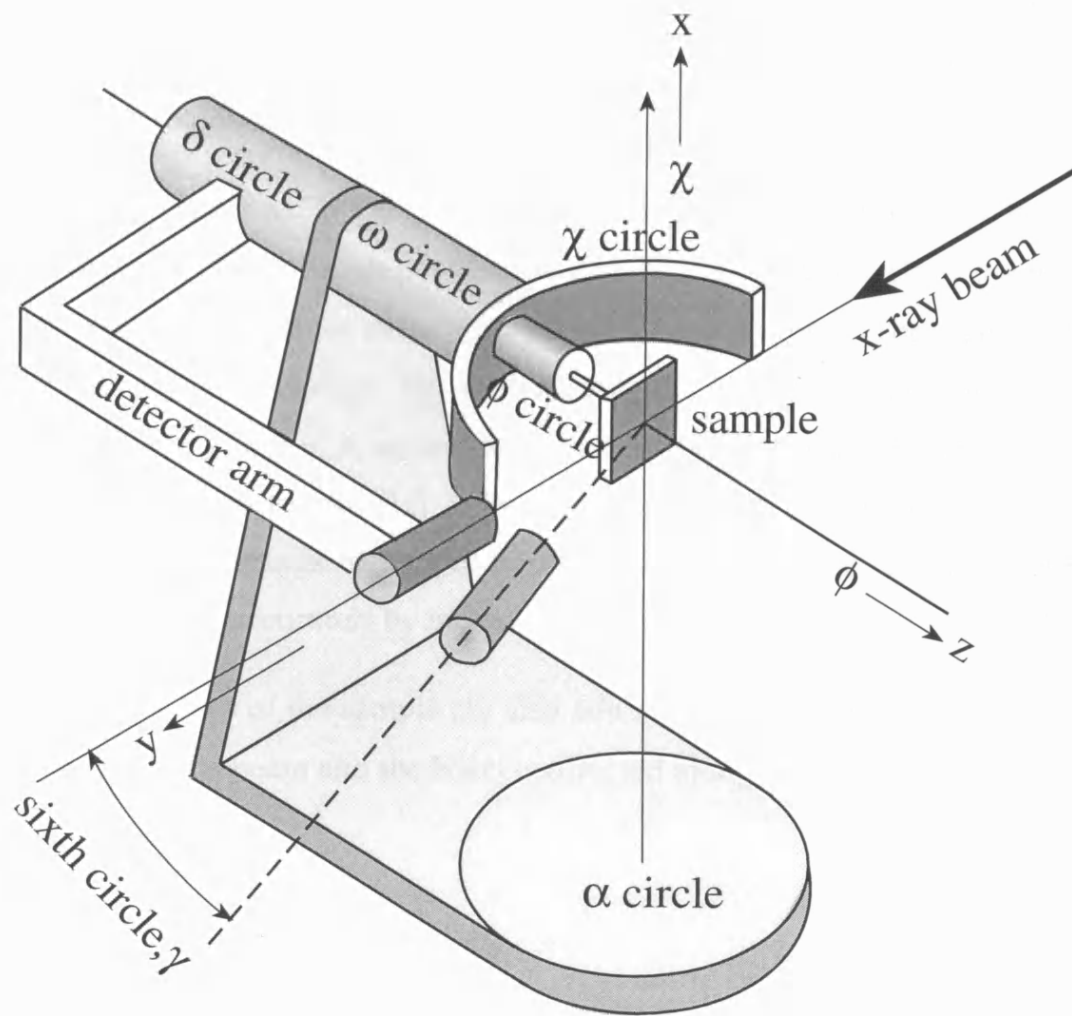
Fig. 4.6: *Schematic diagram of the 6-circle diffractometer on station 9.4 at the SRS, Daresbury.*

4.5.2 Sample alignment.

The sample alignment is carried out in two separate stages. The first step involves aligning the sample such that the surface normal is set parallel to the horizontal axis of the diffractometer. This is achieved by reflecting a low divergence laser from the sample surface. The χ and ϕ circles are adjusted such that a full rotation of the ω-circle causes negligible movement (< 1mm) of the reflected laser spot on a screen placed approximately 4m from the sample.

The second step involves crystallographic alignment using the X-ray beam and two bulk Bragg peaks. A rough position for a given bulk hkλ reflection can be calculated using the χ and ϕ values deduced from the laser alignment. The true position of the reflection is then found by maximising the scattered intensity with careful adjustment of χ and ϕ. A second reflection is also found using the same procedure. This allows a UB matrix [11] to be calculated. The UB matrix relates the angular diffractometer settings to reciprocal space lattice positions. The UB matrix can be calculated more accurately by including more Bragg reflections.

The z and x axes of the sample are also adjusted such that the sample surface sits in the centre of the beam and the beam is directed along the $\delta = 0°$ axis.

4.5.3 Experimental measurements.

The structure factors required for the determination of surface atomic structures are derived from the measurement of the integrated intensity of a series of hkλ reflections. The diffracted intensities are measured by moving to a particular value of hkλ and rotating the crystal about the diffractometer ϕ-axis, which corresponds to a rotation about the sample surface normal. In this way all the diffracted intensity associated with a diffraction rod of finite width is collected. The scattered radiation is recorded by a fixed detector with an angular acceptance, defined by the slits, of 0.82° in-plane (vertical) and 0.25° out-of-plane (horizontal).

For all non-specular reflections the angle of incidence was kept fixed at $\beta_{in} = 1°$, which is well above the critical angle for InSb (0.19°) and avoids any problems caused by total external reflection.

A ϕ-scan of the (1, 1.75, 0.2) fractional-order reflection of the InSb(001)-c(8x2) surface, obtained using the above procedure, is shown in fig. 4.7. The integrated intensity is calculated by first normalising each reflection to the incident flux. A Lorentzian curve is then fitted to the peak in order to obtain a linear background. After subtraction of the background, the peak is integrated numerically.

An in-plane data set is measured by repeating the above method over a large range of h and k at a constant value of λ (typically $\lambda = 0.2$). Diffraction rods are conversely measured as a function of λ at constant values of h and k.

4.5.4   Correction factors.

In order to obtain the structure factors from the measured integrated intensities, certain correction factors need to be applied. They are a direct consequence of the experimental geometry and are related to the diffractometer angles.

All the necessary correction factors have been introduced in eq. (3.39) which is rewritten as

$$I_{int} = r_e^2 \frac{I_0}{\omega} \frac{\lambda^2}{A_u} AF_{Lor}P|F_{hkl}|^2 \Delta\gamma . \qquad (4.1)$$

As we are only interested in the relative values of the structure factors we can ignore the constant terms and rearranging for F_{hkl} we can write
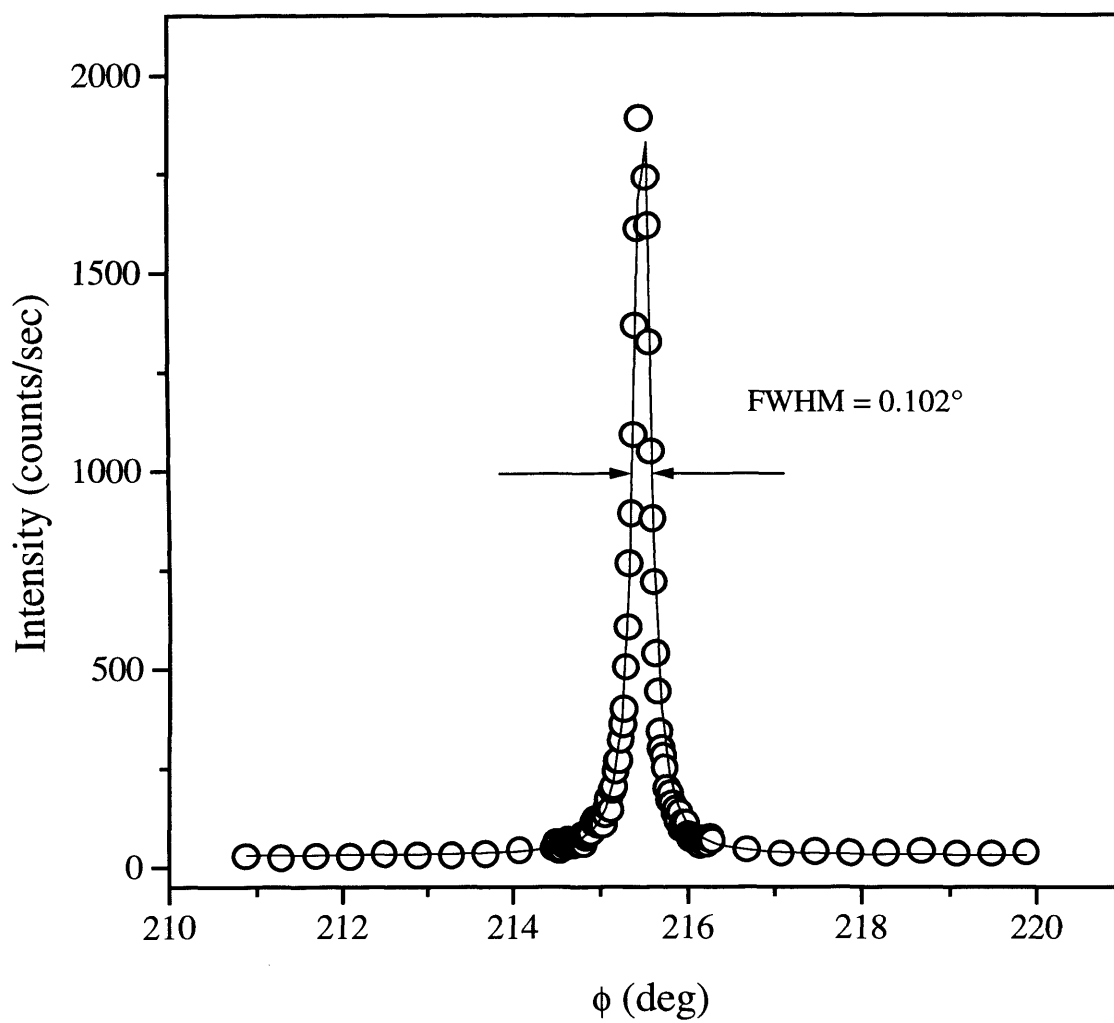
Fig. 4.7: *The (1, 0.75, 0.2) fractional order peak from the clean*
InSb(001)-c(8x2) reconstructed surface.

$$|F_{hkl}|^2 = \frac{I_{int}}{AF_{Lor}P}, \qquad\qquad (4.2)$$

where A is the active sample area, F_{Lor} is the Lorentz factor and P is the polarisation factor. The constant terms are accounted for in the analysis using a scale factor.

The active sample area is the area of the sample surface which is both illuminated by the incident beam and 'seen' by the detector. The size of the active area is therefore defined by the end of beam slits and the first set of detector slits. The active sample area is shown schematically in fig 4.8. As all measurements, except for the reflectivities, were taken using at an angle of incidence $\beta_{in} = 1°$, the sample was always flooded in the horizontal direction.

For the specular rod, the incident and exit angles are symmetrically increased during the measurements, so the sample is not always flooded in the horizontal direction and this special case is discussed elsewhere [12].

The active sample area is infact a parallelogram, the area of which is given by

$$A = v_1 v_2 \sin\delta, \qquad\qquad (4.3)$$

where v_1 and v_2 are the vertical slit settings and δ is the projection of the scattering angle onto the surface plane. As $\beta_{out} = 1°$, we can use the approximation $\delta \sim 2\theta$. Again, as we are using a scale factor we can ignore the constant terms and the area correction to the integrated intensity is merely
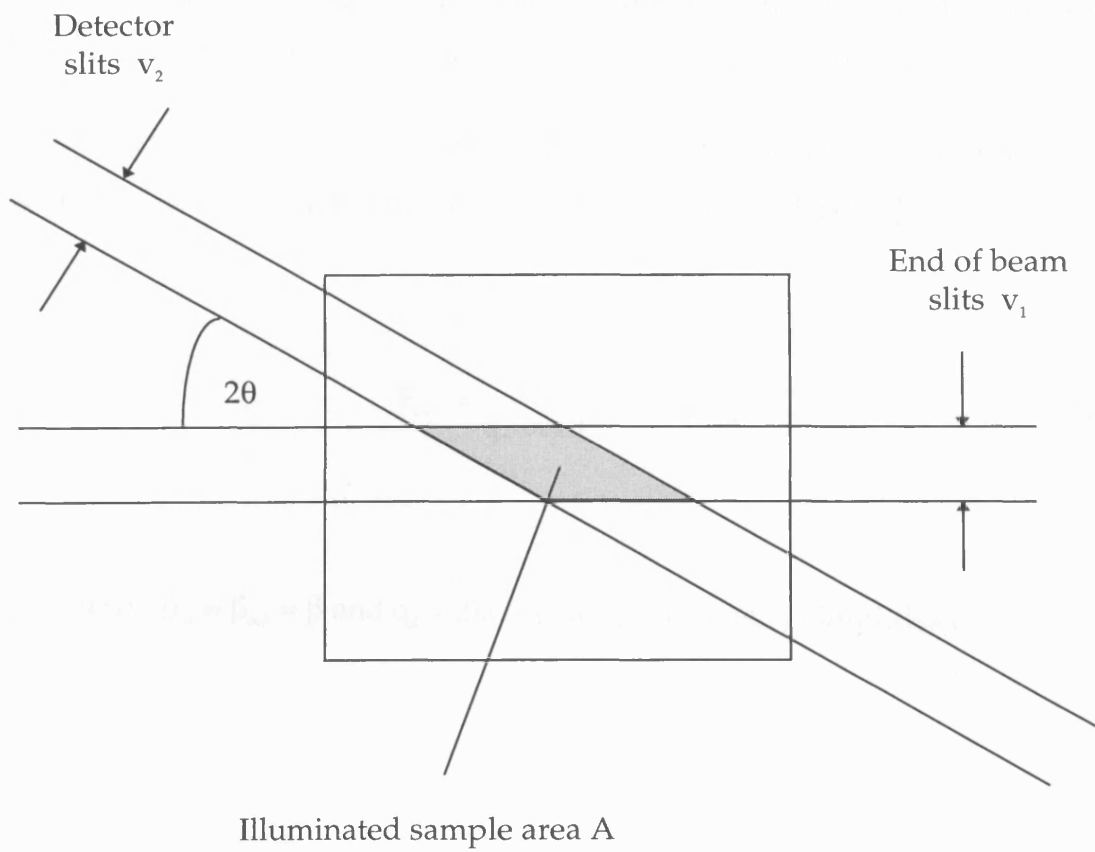
Fig. 4.8: *Schematic showing the in-plane illuminated sample area.*

$$A = \frac{1}{\sin\delta}.$$

(4.4)

It is also noted that this correction is only valid when the diagonal length, d, is not greater than the sample diagonal. In this case (small h and k) another correction needs to be made for the proportion of the beam falling off the sample.

The Lorentz factor corrects for the angle at which the Ewald sphere intersects a diffraction rod. Using the geometry in fig. 3.3 it can be defined as [13]

$$F_{Lor} = \frac{k}{q_{\parallel} \cos\theta}.$$

(4.5)

In our geometry, $\beta_{in} = \beta_{out} = \beta$ and $q_{\parallel} = 2k\cos\beta\sin\theta$ and eq. (4.5) simplifies to

$$F_{Lor} = \frac{1}{\cos\beta\sin 2\theta}.$$

(4.6)

Synchrotron radiation is heavily polarised in the horizontal plane which necessitates the use of a polarisation correction factor, which becomes increasingly important as we move away from a vertical scattering geometry. It is dependent only on the incident and exit angles and not the position of the sample. In consequence it is derived in terms of the angles α and δ. The resulting factor can be written

$$P = \frac{1}{\sin^2\delta + \cos^2\delta\cos^2\alpha}.$$

(4.7)

The final structure factor is calculated by using equations (4.4), (4.6) and (4.7) in eq. (4.2) and taking the square root.

4.6   Symmetry equivalents.

For each of the in-plane data sets collected in this thesis, a complete set of symmetry equivalent reflections was also measured. This was done as any small misalignments or slight changes in the angle of incidence can give rise to a systematic error. This systematic error can, however, be reduced by averaging the intensities from symmetry equivalent reflections. Typical systematic errors are around 10% [14].

If ε is the relative systematic error, the total uncertainty σ_{hkl}^{total} on I_{hkl} is approximately given by [14]:

$$\sigma_{hkl}^{total} = \left[\left(\varepsilon I_{hkl}\right)^2 + \left(\sigma_{hkl}^{stat}\right)^2\right]^{\frac{1}{2}} , \qquad (4.8)$$

where σ_{hkl}^{stat} is the statistical error associated with the curve fitting.

For the two reconstructed surfaces studied, i.e. the c(4x4) and the c(8x2) surfaces, the symmetry space group is c2mm. Hence, each (h,k,λ) reflection has three separate symmetry equivalents, $(-h,k,\lambda)$, $(h,-k,\lambda)$ and $(-h,-k,\lambda)$. However, due to the limited time available coupled with the size of the data sets measured, it was only possible to measure one set, the $(-h,-k,\lambda)$ of symmetry equivalents for each of the reconstructions. The $(-h,-k,\lambda)$ symmetry equivalents are particularly useful as we can make use of the Friedel rule which states:

$$\left|F_{hk\bar{l}}\right| = \left|F_{\bar{h}\bar{k}l}\right| \qquad (4.9)$$

We can therefore obtain, to a first approximation, the structure factors at $\lambda = 0$, which allow us to calculate the Patterson function.

Furthermore, we can obtain a rod scan of the (hk) reflection as a function of negative λ by measuring the (-h,-k) reflection as a function of positive λ.

4.7 χ^2-agreement of fit.

Determination of the atomic positions of all of the InSb(001) surfaces studied in this thesis was achieved by directly comparing the experimental structure factors with theoretical structure factors calculated using eq. (3.17).

The precise surface structure was refined by optimising the agreement between the experimental and theoretical structure factors using a reduced χ^2 test. The reduced χ^2 formula is shown below:

$$\text{reduced}\,\chi^2 = \frac{1}{N-p}\sum_{hkl}\frac{\left(\left|F_{hkl}^{calc}\right| - \left|F_{hkl}^{exp}\right|\right)^2}{\sigma_{hkl}^2} \tag{4.10}$$

where N is the total number of structure factors

   p is the number of free parameters in the theoretical model

   σ_{hkl} is the uncertainty associated with $\left|F_{hkl}^{exp}\right|$

The reduced χ^2 value differs from the standard χ^2 value by a factor of $1/(N-p)$. The reason for this is that the χ^2 distribution is a function of v, the number of free parameters. For a particular value of v the appropriate χ^2 distribution is denoted by χ^2 (v) where, in general, v is given by the number of comparisons N minus the number of free parameters p. The parameter χ^2/v is known as the *reduced* χ^2 value.

A full treatment and justification of the reduced χ^2 test is given by Bevington [15]. The χ^2 test is common in the analysis of X-ray diffraction data. Typical values for χ^2 can be found in many X-ray diffraction studies and are comparable with those found in this thesis, see for example [12,13,16-20].

References.

[1]   C. Norris, J.S.G. Taylor, P.R. Moore, N.W. Harris and M. Miller, *Daresbury Annual Report* (1986/7) 124.

[2]   P.H. Fuoss and I.K. Robinson, Nucl. Instr. Meth. **222** (1984) 171.

[3]   J.S.G. Taylor, C. Norris, E. Vlieg, M. Lohmeier and T.S. Turner, Rev. Sci. Instr. **67** (7) (1996) 2658.

[4]   J.S.G. Taylor and J. Newstead, J. Phys E: Sci. Instrum. **20** (1987) 1288.

[5]   S. Brennan and P. Eisenberger, Nucl. Instr. Meth. **222** (1984) 164.

[6]   E. Vlieg, A. van't Ent, A.P. Jongh, H. Neerings and J.F. van der Veen, Nucl. Instr. Meth. A **262** (1987) 522.

[7]   S.D. Evans, L.L. Cao, R.G. Egdell, R. Droopad, S.D. Parker and R.A. Stradling, Surf. Sci. **226** (1990) 169.

[8]   M.K. Gardiner, *PhD thesis*, University of Leicester (1983).

[9]   A. Primer, *Synchrotron Radiation Sources*, edited by H. Winick, World Scientific, Singapore (1994).

[10]   R. Cernik and M. Hart, Nucl. Instr. Meth. A **281** (1989) 403.

[11]   E. Vlieg, J.F. van der Veen, J.E. MacDonald and M. Miller, J. Appl. Cryst. **20** (1987) 330.

[12]   P. Steadman, *PhD thesis*, University of Leicester (1997).

[13]   E. Vlieg, *PhD thesis*, FOM Institute, Amsterdam (1987).

[14]   R. Fiedenhans'l, Surf. Sci. Rep. **10** (1989) 105.

[15]   P.R. Bevington, *Data Reduction and Error Analysis for the Physical Sciences*, McGraw Hill, New York (1969).

[16]   P.B. Howes, C. Norris, M.S. Finney, E. Vlieg and R.G. van Silfhout, Phys. Rev. B **48** (1993) 1632.

[17]   R.G. van Silfhout, J.F. van der Veen, C. Norris and J.E. Macdonald, Faraday
        Discuss. Chem. Soc. **89** (1990) 169.

[18]   J. Bohr, R. Fiedenhans'l, M. Nielsen, M. Toney, R.L. Johnson and I.K.
        Robinson, Phys. Rev. Lett. **54** (1985) 1275.

[19]   M. Lohmeier, H.A. van der Vegt, R.G. van Silfhout, E. Vlieg, J.M.C. Thornton,
        J.E. Macdonald and P.M.L.O. Scholte, Surf. Sci. **275** (1992) 190.

[20]   G. Charlton, P.B. Howes, C.L. Nicklin, P. Steadman, J.S.G. Taylor, C.A.
        Muryn, S.P. Harte, J. Mercer, R. McGrath, D. Norman, T.S. Turner and G.
        Thornton; Phys Rev Lett. **78**, (1997) 495-498.

Chapter 5.

Atomic structure of the InSb(001)-c(4x4) reconstruction.

The atomic structure of the Sb-terminated InSb(001)-c(4x4) reconstruction has been determined using X-ray diffraction. A total of 132 in-plane reflections were used to determine the structure in the surface plane. Out-of-plane structure was calculated by measuring intensity profiles along four integer-order and two fractional-order diffraction rods. The primitive unit cell of the c(4x4) phase consists of groups of three symmetric Sb dimers chemisorbed onto a complete Sb layer. The groups are found to be incomplete in ~1/3 of the cases. The calculated bond length of the central dimer is 2.91±0.02Å. The outer dimers are extended with a separation of 3.14±0.02Å. The bond angles are indicative of sp^3-type bonding. The data suggests that the reconstruction is limited mainly to the top layer, with only slight relaxation of the underlying bulk layers.

5.1 Introduction.

InSb is attracting increasing attention due to its potential application in near infra-red detection [1] and high speed opto-electronics [2]. A factor determining the performance of devices which employ thin, epitaxially grown, layers is the atomic arrangement of the surface on which deposition occurs. It can influence the form of the growth and the degree of order at a heterointerface. A detailed knowledge of the structure of the clean surface, prior to epitaxial growth, is therefore essential. For III-V based devices the group V terminated (001) surface is the most important technologically since most devices are grown on this face.

In contrast to the (001) surface of GaAs there have been relatively few fundamental studies of the (001) surface of InSb [3-11]. As described in chapter 2, RHEED measurements by Oe *et al* [3] and Noreika *et al* [4], identified several surface reconstructions of the InSb(001) surface and a phase diagram with substrate temperature and surface stoichiometry as parameters was established, (fig. 2.2). The most ordered phases are the In rich c(8×2) phase produced by argon bombardment and annealing and the c(4×4) phase, the subject of this chapter, produced by Sb adsorption in the temperature range 280-360°C; the precise temperature depends on the Sb flux.

Using high energy electron diffraction (HEED) and core-level photoemission spectroscopy (PES), John *et al* [5] proposed that the c(4×4) involves a complete Sb layer covered by 3/4 of a monolayer of Sb. Atomic resolution scanning tunnelling micrographs of the c(4×4) reconstruction produced by McConville *et al* [10] are displayed in fig. 5.1. The images clearly reveal a surface layer consisting of groups of six circular features which are attributed to Sb atoms which form three dimers.

The structure of the InSb(001)-c(4×4) surface thus appears to be similar to c(4×4) structures produced on other III-V (001) surfaces in conditions of excess pressure of the group V element [12,13,14,15]. In each case the reconstruction involves extra group V atoms which form a regular array of blocks of dimers; the dimers being aligned along the bulk [110] axis of the underlying substrate. An important question
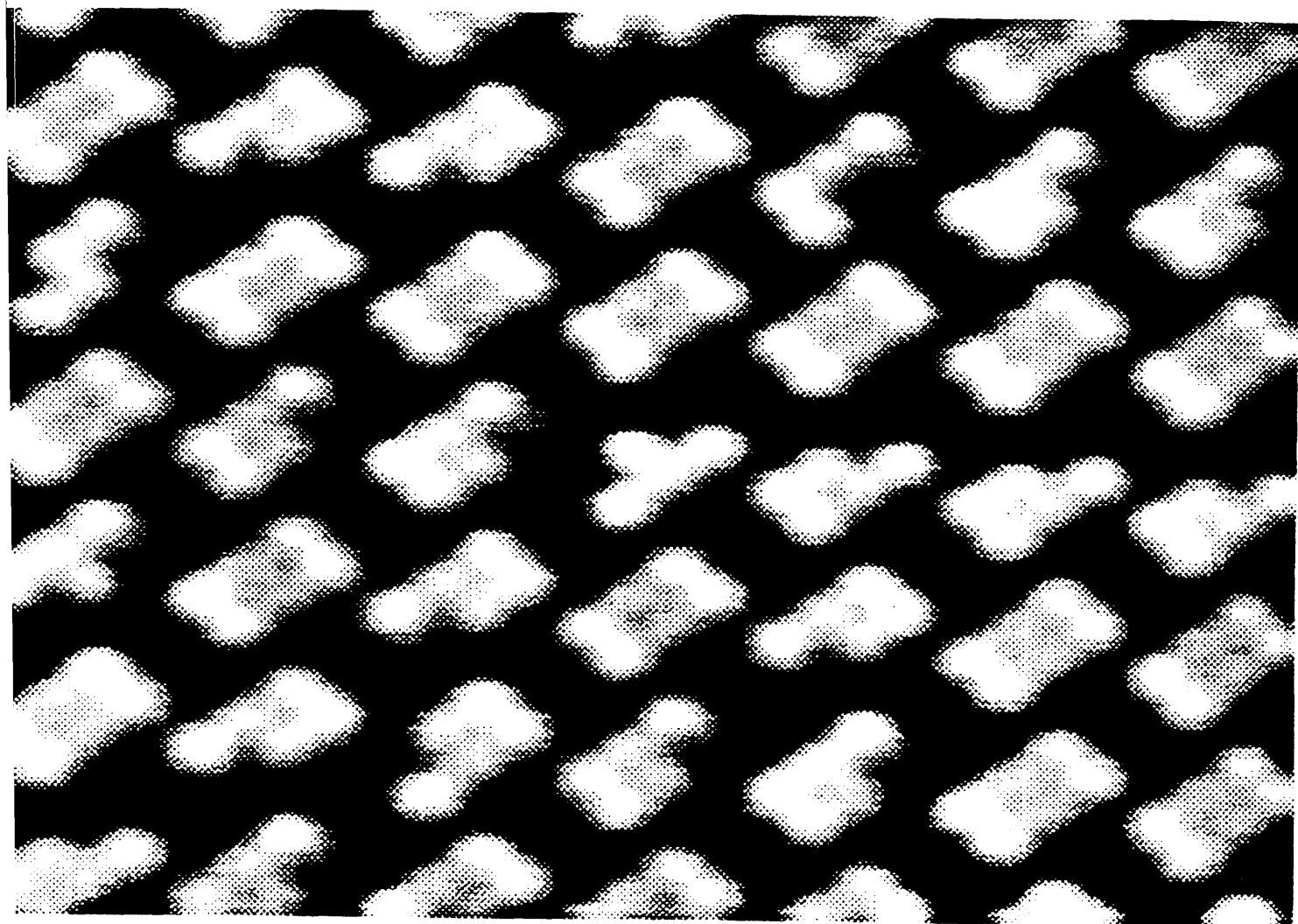
Fig 5.1: *High resolution filled state STM images of the InSb(001)-c(4x4) reconstruction [10].*

that has arisen concerns the number of dimers involved in the basic unit. Larsen *et al* [12] proposed that for GaAs(001) two different structures, one involving single dimers and the other blocks of two dimers, coexisted. Sauvage-Simkin *et al* [14] suggested a mixture of structures involving two and three dimers to account for the wide range of stoichiometry over which the structure is observed. STM results by Avery *et al* [16] for GaAs and McConville *et al* [10] for InSb, however, indicate that the variation in coverage is associated with vacancies in a three dimer model and that two fundamentally different structures do not coexist.

Dimerisation is a common feature of the (001) face of elemental and zinc blende type semiconductors. It reduces the surface energy by removing unpaired bonds and is balanced by strain that is induced in the layers below to which the dimer atoms are chemisorbed. A complete understanding of the reconstruction demands a detailed knowledge of the atomic positions, not only of the chemisorbed layer, but deeper into the bulk. STM cannot, in general, provide information beyond the topmost layer. Little is known of the bonding geometry of the InSb(001)-c(4x4) surface; there are no reports to date of dimer bond lengths or of the bond angles between the dimers and the underlying substrate. The composition and geometry of the underlying layers are also undetermined.

We report the first surface X-ray diffraction (SXRD) study of the atomic structure of the InSb(001)-c(4x4) reconstruction. SXRD is now established as a powerful probe of surface crystallography and has been successfully used to solve quantitatively the structure of many clean and adsorbate covered semiconductor surfaces [17,18]. Three SXRD studies of the equivalent surface of GaAs have, however, been reported. Sauvage-Simkin *et al* [14] suggested that the As-As dimer length was 3-5% longer than the interatomic separation in bulk As, 2.51Å. A later report by Lamelas *et al* [19] for the 2x4 structure, attributed to a disordered form of the c(4x4) structure, put the value much closer. They also identified a small movement in the underlying As layer. Payne *et al* [20] agreed that the c(4x4) structure is a mixture of two and three dimer domains and suggested, in the latter case, that the outer dimer bond length is significantly less than that of bulk As value .

In the present study a large data set has been collected which includes both in-plane and out-of-plane measurements. It has enabled an accurate full three-dimensional model of the InSb(001)-c(4×4) reconstruction to be determined for the first time.

5.2   Experimental.

The measurements were made on Beamline 9.4 of the Synchrotron Radiation Source (SRS) at Daresbury Laboratory, UK. Radiation from the 5.0T superconducting wiggler was focused by a platinum coated, toroidal mirror onto an InSb(001) sample held in an ultra high vacuum (UHV) chamber. A wavelength of 0.9Å was selected using a water cooled Si(111) channel-cut monochromator; the scattered radiation was recorded by a solid-state Ge detector. Slits in front of the detector fixed the angular acceptance to be 0.82° in-plane (vertical) and 0.25° out-of-plane (horizontal).

The InSb(001) sample with dimensions 8x8x0.5mm^3 was cut from a wafer supplied by MCA Wafer Technology. The wafer was cleaned and etched in a mixture of lactic, nitric and hydrofluoric acids, as described in section 4.3, before being loaded into a UHV chamber in which it was capped with a protective overlayer, approximately 1000Å thick, of amorphous Sb [21]. The small square sample was bonded to a Mo backing plate using a thin In seal, fig 4.2, before being mounted in the SXRD environmental chamber which was coupled via a differentially pumped rotary seal to a 6-circle diffractometer [22]. The base pressure in the chamber was ~ 1x10^{-10} mbar.

The thick native oxide layer was removed with a single cycle of argon ion bombardment (800eV, 1µA, 45 mins) and annealing (250°C, 20 mins). Thereafter, the sample was held in an Sb-flux deposited from a Knudsen evaporation source. The sample was heated to 300°C for 20 mins in order to desorb the amorphous cap. The Sb-flux was necessary to prevent the surface becoming In-rich. After closing the shutter on the vapour source and cooling the sample to room temperature, a clear c(4x4) LEED pattern was observed.

For the analysis of the diffracted intensity the atomic structure of the InSb(001) surface is described by a tetragonal unit cell defined by three base vectors a_i. The vectors are related to the conventional face centred cubic unit cell by :

$$\mathbf{a}_1 = \frac{1}{2}[1\bar{1}0]_{cubic} \qquad \mathbf{a}_2 = \frac{1}{2}[110]_{cubic} \qquad \mathbf{a}_3 = [001]_{cubic}$$

<div align="right">(5.1)</div>

where : $\qquad\qquad |\mathbf{a}_1| = |\mathbf{a}_2| = \frac{\sqrt{2}}{2}a_0 \qquad |\mathbf{a}_3| = a_0$

where a_0 is the InSb bulk lattice constant, 6.479Å.

Using this convention $\mathbf{a}_1$ and $\mathbf{a}_2$ are both parallel to the surface and $\mathbf{a}_3$ is directed normal to the surface. The corresponding reciprocal lattice vectors are:

$$\mathbf{b}_1 = \frac{1}{2}(2\bar{2}0)_{cubic} \qquad \mathbf{b}_2 = \frac{1}{2}(220)_{cubic} \qquad \mathbf{b}_3 = \frac{1}{2}(002)_{cubic}$$

<div align="right">(2)</div>

where $\qquad\qquad |\mathbf{b}_1| = |\mathbf{b}_2| = \frac{2\sqrt{2}\pi}{a_0} \qquad$ and $\qquad |\mathbf{b}_3| = \frac{2\pi}{a_0}$

The momentum transfer vector $\mathbf{Q}$ is defined by the Miller indices (hkl) with $\mathbf{Q} = h\mathbf{b}_1 + k\mathbf{b}_2 + \lambda\mathbf{b}_3$. General reflections are labelled by (hkλ) and in-plane reflections ($\lambda \sim 0$) by (hk).

The sample surface was aligned as described in section 4.5.2. The surface normal was measured to be within 0.2° of the (001) crystallographic axis. Diffracted intensities

were measured by rotating the crystal about the diffractometer ϕ-axis (corresponding to a rotation about the sample surface normal) with the detector fixed. Integrated intensities were obtained by numerically integrating the peaks after background subtraction. The corresponding structure factors were calculated from the integrated intensities by correcting for the Lorentz factor, the polarisation factor and the illuminated surface area. As the sample was always flooded in the horizontal plane the area correction was always $\sin 2\theta$, where 2θ is the in-plane scattering angle. Symmetry equivalent reflections agreed within 5%, the associated error with each reflection being calculated by summing the squares of the systematic and statistical errors and taking the square root [23].

A total of 132 in-plane reflections were measured of which 116 were fractional-order and 16 integer-order. Other reflections were too weak to be determined accurately. The in-plane reflections were measured at an λ value of 0.2. The angle of incidence, β_{in} , was kept equal to the exit angle β_{out} at ~ 0.8° which is well above the critical angle for InSb (0.19°) and thus avoids complications due to total external reflection. Out-of-plane measurements were made perpendicular to the surface as a function of λ along four integer-order and two fractional-order rods. In this instance, the angle of incidence was fixed at $\beta_{in}= 1°$, the exit angle, however, was allowed to vary. The procedure for measuring the specular rod is different to that for the integer-order rods, (section 8.2).

During data collection the (1, 1/2, 0.2) reflection was regularly scanned in order to monitor any surface degradation. The intensity was found to decay exponentially with a half-life of approximately 50 hrs without a change in the width. This was most likely caused by contamination producing a deconstruction of the c(4x4) arrangement.

5.3 Results.

The atomic structure of the surface unit mesh is determined by comparison of the measured structure factor amplitudes, $|F_{hkl}|$, with the predictions of given models. The structure factor of a particular reflection is given by eq. (3.17), which is rewritten below :

$$F_{hkl} = \sum_j f_j \exp\left[\frac{-B_j Q^2}{16\pi^2}\right] \exp\left[2\pi i\left(hx_j + ky_j + \lambda z_j\right)\right] \tag{5.3}$$

where Q is the momentum transfer and the sum extends over all atoms in the unit cell. f_j is the atomic scattering factor, and $\{x_j\ y_j\ z_j\}$ the positional coordinates of the jth atom. B_j is the isotropic Debye-Waller factor, given by :

$$B_j = 8\pi^2 <u_j^2> \tag{5.4}$$

where $<u_j^2>$ is the mean square vibrational amplitude. Throughout the analysis we have used the bulk value for $B = 0.7\ \text{Å}^2$ [25]. It is found B has a small effect on the fitting and is therefore held constant during the analysis.

In-plane positions are initially determined using the reflections at low $Q_{parallel}$ ($\lambda=0.2$). The out-of-plane structure is then obtained by measuring both fractional and integer order reflections as a function of λ. In this way the full three-dimensional model of the c(4x4) reconstruction is established.
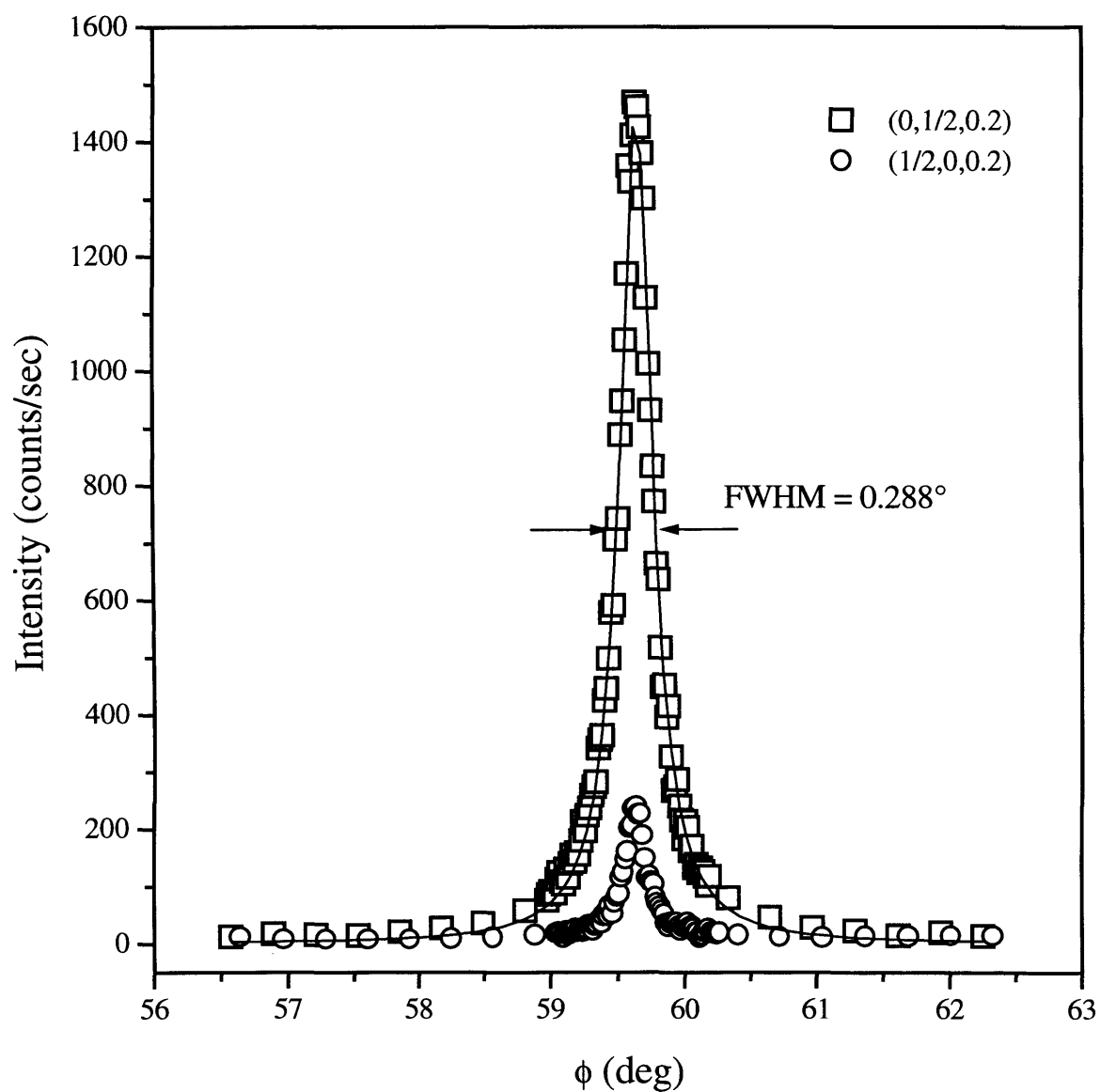
Fig 5.2: *The (0,1/2,0.2) and (1/2,0,0.2) fractional-order reflections.*

The clear differences in intensity indicate the lack of four-fold symmetry exhibited by the reconstrcution. The two curves are centred at the same phi-value for comparison. The fitted curve is Lorentzian.

5.3.1 In-plane structure.

A total of 116 fractional-order and 16 integer-order reflections were used to determine the in-plane structure. The (1/2, 0, 0.2) fractional-order reflection is shown in fig. 5.2. It is fitted with a Lorentzian curve with a FWHM of $0.288°$ which corresponds to a correlation length of 580Å. As the space group is c2mm, reflections were recorded over opposite quadrants in reciprocal space in the hk plane. The absence of four fold symmetry is clearly demonstrated by comparing the (1/2, 0, 0.2) with (0, 1/2, 0.2) reflection shown in fig. 5.2.

To determine the structure we first calculate the two dimensional fractional-order Patterson function :

$$P(\mathbf{r}) = \sum_{hk} |F_{hk0}|^2 \cos(2\pi(hx + ky)) \qquad (5.5)$$

where the sum extends over the two-dimensional hk plane. The in-plane structure factors $|F_{hk0}|$ are estimated by averaging the measured structure factor amplitudes at (h, k, 0.2) and (h, k, -0.2). The latter is equivalent to $|F_{-h\,-k\,0.2}|$ by the Friedel rule. When averaged in this way the 116 reflections reduced to 58 inequivalent reflections.

The calculated Patterson map is shown in fig. 5.3. For clarity only positive values are plotted. The Patterson function reveals principal interatomic correlations which, since only fractional-order reflections were included in the sum, are defined by the reconstructed surface and not the underlying bulk. The strongest peaks in the plot are the self correlation peaks due to the c(4x4) symmetry. In addition, there are two extra features, marked by the orthogonal vectors I and II, which can be identified with interatomic correlations within the unit mesh. The simplicity of the plot suggests a well defined local arrangement. Vector I corresponds to an interatomic separation of 2.95Å. This is close to the nearest neighbour distance in bulk antimony
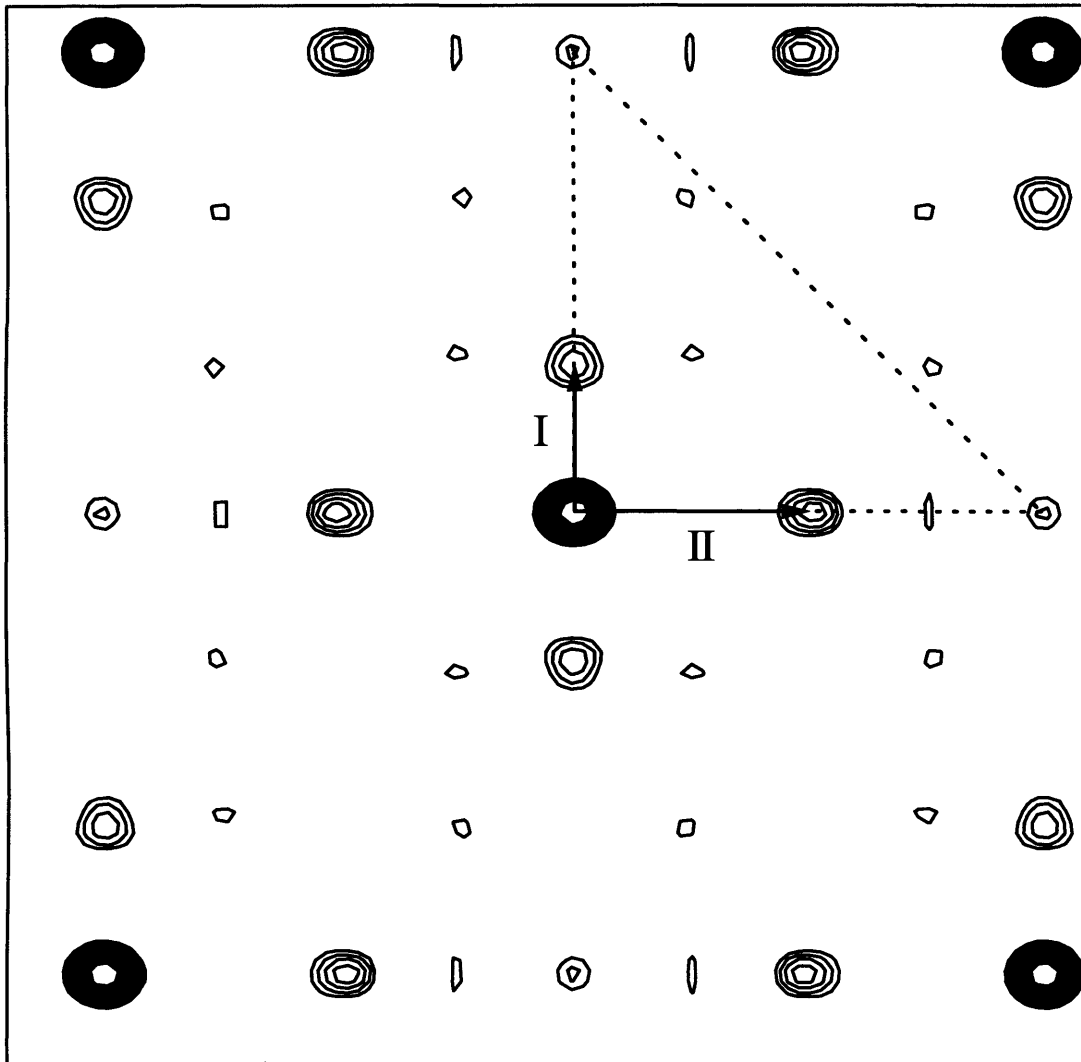
Fig. 5.3: *Patterson map of the c(4x4) reconstructed surface calculated from the averaged fractional-order structure factors. For clarity, only positive peaks are shown. The arrows to the non-self correlation peaks indicate dominant interatomic correlations. The dotted lines mark the irreducible part of the unit cell.*

2.87Å [26] and is attributed to the distance between Sb atoms within a dimer. The dimer is aligned along the [110] axis of the bulk structure. The length of vector II is 4.5Å which is close to the interatomic distance along the bulk [1$\bar{1}$0] axis of InSb, 4.58Å. We can therefore, associate vector II with the displacement between adjacent dimers.

Two possible models of the InSb(001)-c(4x4) structure are shown in fig. 5.4. The lower figure is the structure suggested by John *et al* [5] and has a repeating arrangement of groups of three Sb dimers on top of an Sb-terminated bulk. The upper figure has groups of two Sb dimers and is equivalent to the structure suggested to coexist on the GaAs(001) surface [14,20]. The Patterson map is consistent with both arrangements as both vectors I and II occur in the local atomic arrangement. The weak feature in fig. 5.3 at twice the distance of vector II could be due to the separation of atoms at the edges of the three dimer unit in fig. 5.4(b). The strength of the feature marked by vector II strongly suggests that a structure involving only one dimer is unlikely.

The atomic structure was determined by directly comparing the experimental structure factors with theoretical structure factors calculated using a particular model. The fitting was achieved using a χ^2 minimisation procedure as outlined in section 4.7. The fitting was carried out using an analysis package called ROD, developed by and used with the permission of Elias Vlieg of the FOM Institute, Amsterdam, Holland. The package allows not only the positions of the atoms in the surface model to be varied in all three dimensions, but also allows the occupancy of the atomic sites to be varied. The program also allows a β-roughness parameter [35] to be calculated.

To confirm which of the dimer arrangements occur we compared the estimated intensities at $\lambda = 0$ with the values calculated for the different models. The dimer distance was set to the value suggested by the Patterson map and the bulk Debye-Waller factor included. Allowing only a scale factor to vary, the one dimer and two dimer models yielded χ^2 values of 12.3 and 9.3 respectively. The best fit, however, was achieved with the three dimer model which gave a χ^2 value of 5.2. For

[110]

[1̄10]

Top layer Sb   2nd layer Sb
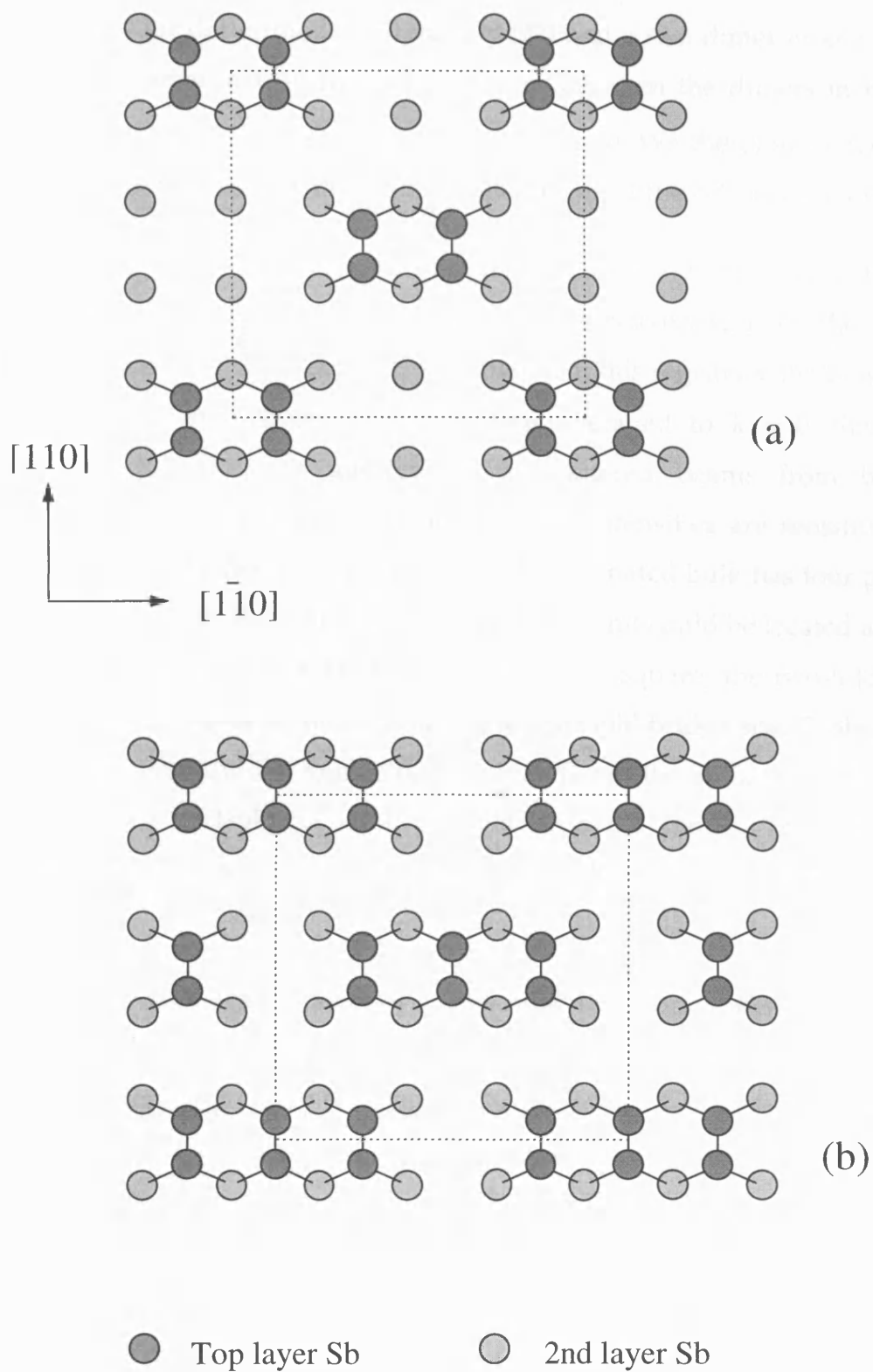
Fig. 5.4: *Proposed models for the c(4x4) reconstruction of the InSb(001) surface. (a) two dimer clusters and (b) three dimer clusters. The dashed lines mark the centred surface unit cell in each case. The crystallographic axes of the bulk cubic structure are also shown.*

completeness, a four dimer model, Chadi *et al* [27] and a two dimer model in which the dimers were separated by twice the distance between the dimers in fig. 5.4(a) were also tried, but yielded a χ^2 of over 20 in each case. We therefore conclude that the three dimer arrangement is the basic building block of the c(4x4) reconstruction.

The arrangement of the dimers on the underlying substrate suggested by John *et al* [5] and shown in fig. 5.4(b) is the one which most effectively satisfies the available bonds of the Sb-terminated substrate. Confirmation of this registry with the substrate is provided by the 16 integer-order reflections averaged to $\lambda = 0$. Since these reflections are the result of interference of scattered beams from both the reconstructed surface and the underlying bulk, the intensities are sensitive to the relative positions of the two components. The Sb-terminated bulk has four positions of high symmetry where the centre of the three dimer unit could be located as shown in fig. 5.6. These are the four-fold centre, A, of the Sb square, the two-fold site, B, vertically above an In atom in the third layer, the two-fold bridge site, C, above an In atom in the fifth layer and the four-fold site, D, on top of the Sb in the second layer. The results shown in table 5.1 confirms that A is the centre. The best-fit and experimental structure factors for the integer order reflections are displayed in table 5.2.

The in-plane structure was refined by comparing the model with the measured intensities at $\lambda = 0.2$. The heights of the atoms were fixed at the bulk InSb values, the Sb dimers in the top (first) layer being at the height of the next In layer of the bulk. The in-plane positions of the dimers were initially set at the value suggested by the Patterson map. The dimer atoms were allowed to relax along the orthogonal axes parallel and perpendicular to the dimer direction in a way which maintained the c2mm symmetry. Lateral relaxations of the underlying second (Sb) and third (In) layers were also included. Increasing the number of atoms involved in the reconstruction to the fourth (Sb) and fifth (In) layers did not improve the fit. In the first three layers there are eleven independent positional variables which are shown in fig. 5.5. The movements of the other atoms are determined by the symmetry group. The resulting best fit gave a χ^2 of 2.14; the significant displacements are shown in fig. 5.5. Other displacements, less than 0.01Å, are not included. The fit
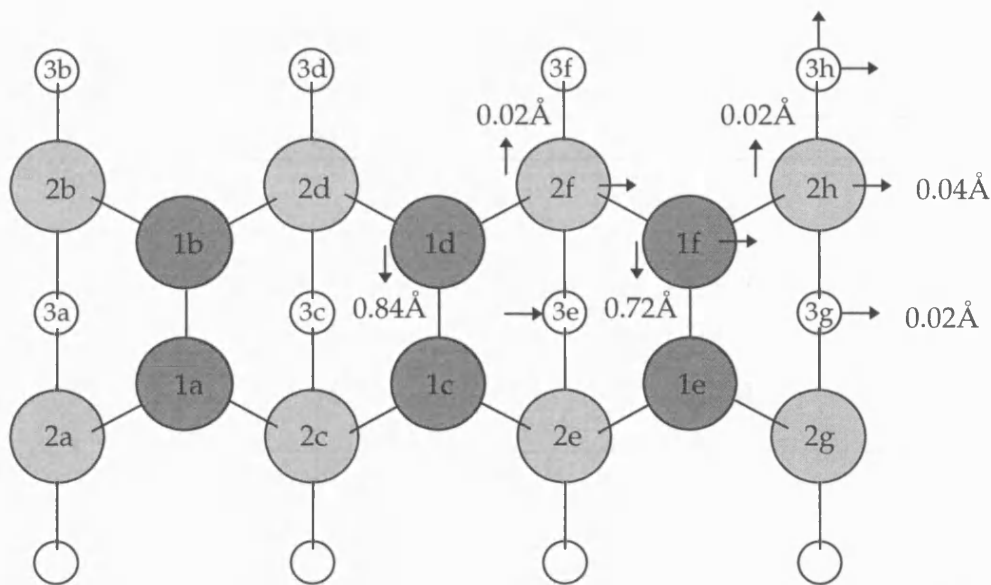
Fig 5.5 : *The first three layers of the c(4x4) surface. The arrows denote the eleven independent positional variables. The best-fit displacements are shown. Unassigned arrows correspond to negligible displacements*
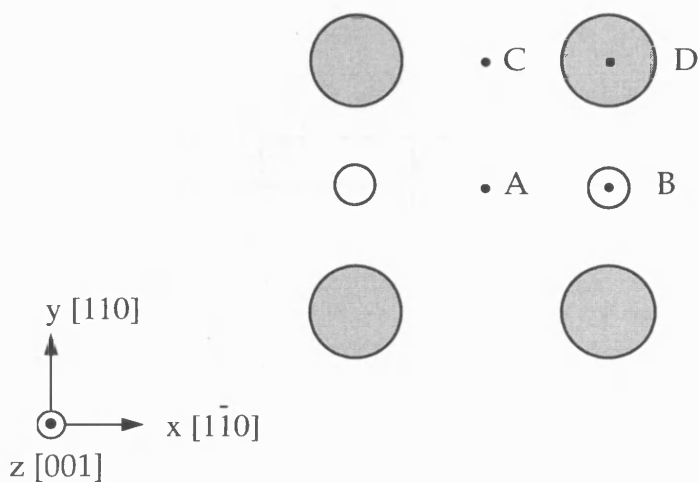
Fig 5.6 : *Four positions, A-D, of high symmetry where the centre of the three dimer cluster could be positioned. For clarity, the dimer cluster is not shown.*

Site	χ^2
A	4.7
B	115.4
C	29.5
D	121.4

Table 5.1 : *Values of χ^2 for the agreement of the integer-order intensities with the measured values given by the various registries possible for the three dimer cluster. The results clearly indicate position A to be correct.*

h	k	$|F^{calc}_{hk}|$	$|F^{exp}_{hk}|$	σ_{hk}
1	0	18.20	16.50	1.0
0	1	27.52	23.12	2.1
1	1	9.43	15.35	1.9
2	1	22.52	24.05	2.2
2	0	161.96	167.18	5.6
1	2	68.69	66.87	3.9
3	0	12.16	15.96	2.4
0	3	31.21	28.38	2.4

Table 5.2 : *Experimental in-plane integer-order reflections measured at $\lambda = 0.2$. The calculated values for the dimer cluster centred on position A are also included.*

h	k	$\|F_{hk}^{calc}\|$	$\|F_{hk}^{exp}\|$	σ_{hk}
0	1/2	24.10	21.14	4.62
0	3/2	41.89	43.75	3.76
0	5/2	18.43	22.72	2.57
0	7/2	14.17	14.50	0.72
1/4	1/4	15.40	11.31	1.73
1/4	3/4	3.96	5.01	1.80
1/4	5/4	12.78	19.65	3.09
1/4	7/4	14.74	11.69	1.05
1/4	11/4	10.43	16.06	3.13
1/4	13/4	10.01	8.45	1.95
1/4	15/4	3.30	1.98	1.14
1/2	1/2	4.86	6.37	2.42
1/2	3/2	13.00	13.67	2.68
1/2	2	4.85	10.81	4.08
1/2	3	10.69	6.45	2.58
1/2	7/2	3.47	10.12	5.22
3/4	1/4	13.91	10.21	1.79
3/4	3/4	2.44	3.54	1.15
3/4	5/4	9.68	9.53	1.96
3/4	7/4	12.44	16.82	2.20
3/4	9/4	4.58	8.53	2.05
3/4	11/4	8.31	6.16	2.60
3/4	13/4	13.58	12.60	3.66
1	1/2	22.11	20.36	1.58
1	3/2	39.32	23.00	6.15
1	5/2	17.39	19.21	1.91
1	7/2	14.12	19.83	6.17
5/4	1/4	13.94	19.87	2.70
5/4	3/4	3.04	8.15	1.78
5/4	5/4	12.75	12.79	2.01
5/4	7/4	11.20	22.50	3.47
5/4	9/4	3.91	7.79	5.66
5/4	11/4	4.94	5.89	4.10
3/2	1	12.87	15.62	2.62
3/2	3/2	9.89	10.37	2.79
3/2	5/2	12.32	11.92	2.68
7/4	1/4	14.06	12.97	1.61
7/4	3/4	3.77	3.71	3.89
7/4	5/4	15.11	14.34	2.48
7/4	7/4	12.55	18.48	2.76
7/4	9/4	3.05	0.00	2.61
7/4	11/4	7.05	9.61	1.94
2	1/2	18.82	24.98	2.01
2	3/2	35.84	37.18	2.35
9/4	1/4	10.21	9.61	1.94
9/4	3/4	5.24	0.00	2.74
5/2	0	6.51	7.45	2.32
5/2	1/2	3.47	6.10	2.34
5/2	1	7.89	8.50	2.89
5/2	3/2	12.84	12.31	2.32
11/4	1/4	9.96	7.73	2.30
11/4	3/4	6.03	6.77	2.69
11/4	5/4	5.13	9.09	2.68
11/4	7/4	11.27	11.55	2.37
11/4	11/4	10.74	10.79	2.51
3	1/2	16.79	10.53	2.54
3	5/2	14.81	13.89	2.51
13/4	1/4	10.76	7.66	2.96

Fig. 5.3: *Experimental in-plane fractional-order structure amplitudes measured at $\lambda = 0.2$ with associated errors. The calculated best-fit values for the final model are also included.*

further improves to $\chi^2 = 1.97$ by allowing the occupancy of the dimer atoms to relax as suggested by the STM studies [10,16]. The best-fit and experimental structure factors for one quadrant are shown in table 5.3. The central dimer separation of 2.91±0.02Å is close to the nearest neighbour distance of bulk Sb (2.87Å). The outer dimers are slightly extended with a separation of 3.14±0.02Å. The occupancy of the outer dimers is significantly lower than unity, (0.92). This implies that, on average, approximately one in every three blocks of dimers has an outer dimer atom missing. This is consistent with the STM images [10], fig. 5.1, which shows a similar proportion of the dimer blocks with one or more atoms absent. It is likely, following the measurements on GaAs (001) by Avery *et al* [16] that the occupancy is strongly dependent on the preparation conditions.

5.3.2   Out-of-plane structure.

The atomic coordinates perpendicular to the reconstructed surface are determined from an analysis of the scattered intensity distribution as a function of λ along the rods normal to the surface plane. The four measured non-specular integer-order rods (or crystal truncation rods, CTRs) are shown in fig. 5.7. The rods are essentially featureless with the only sharp changes in intensity at the bulk Bragg peaks. Similarly, the two measured fractional-order rods (fig. 5.8) are almost flat over a range of 3 reciprocal lattice units. This implies that the reconstruction is limited to a depth of less than $a_0/3$. It supports the analysis of the in-plane reflections which shows that the reconstruction is dominated by the top layer dimerisation and that the underlying structure is similar to that of the bulk arrangement. The error bars are calculated in the same way as for the in-plane data, taking both statistical and systematic errors into account. An oblique view of the structure is shown in fig. 5.9; the atom notation corresponding to that of fig. 5.5. For clarity, only two dimers, the central (1c,d) and one outer (1a,b) are shown. In fitting the rods, the x and y atomic coordinates derived from the in-plane measurements were assumed. The height of the central dimer (1c,d) was allowed to move vertically and independently of the outer dimers which were constrained to move together. All the Sb atoms in the
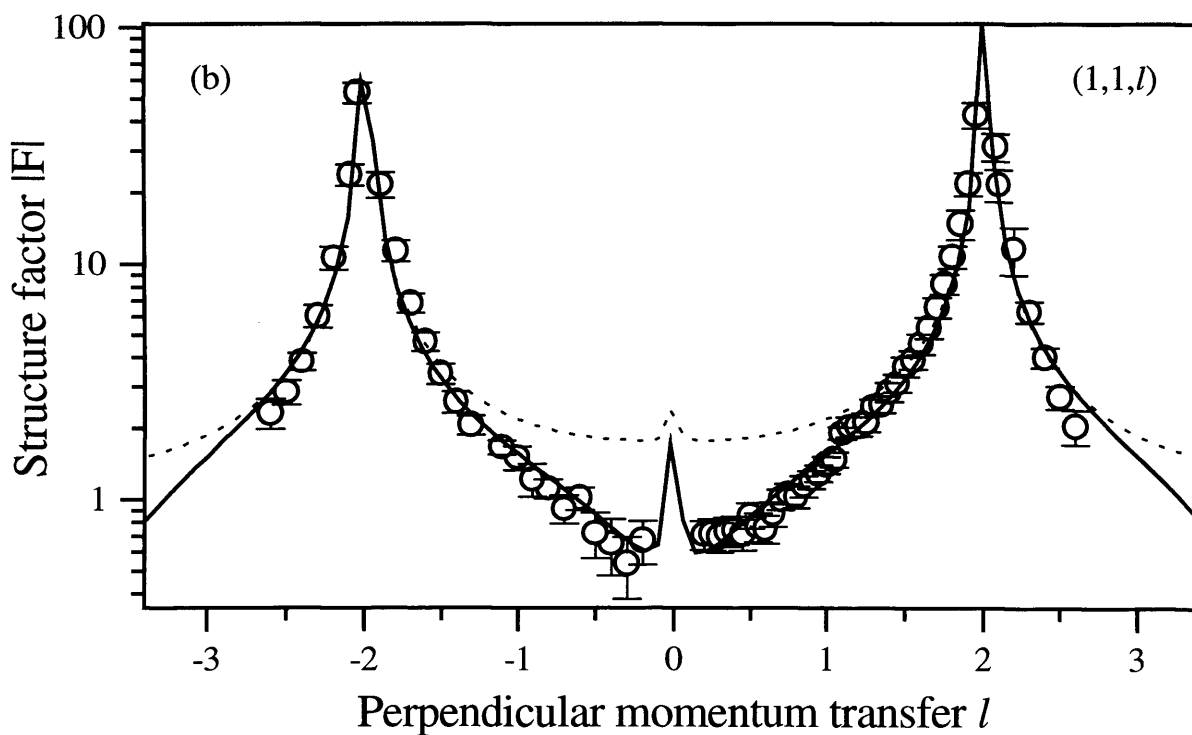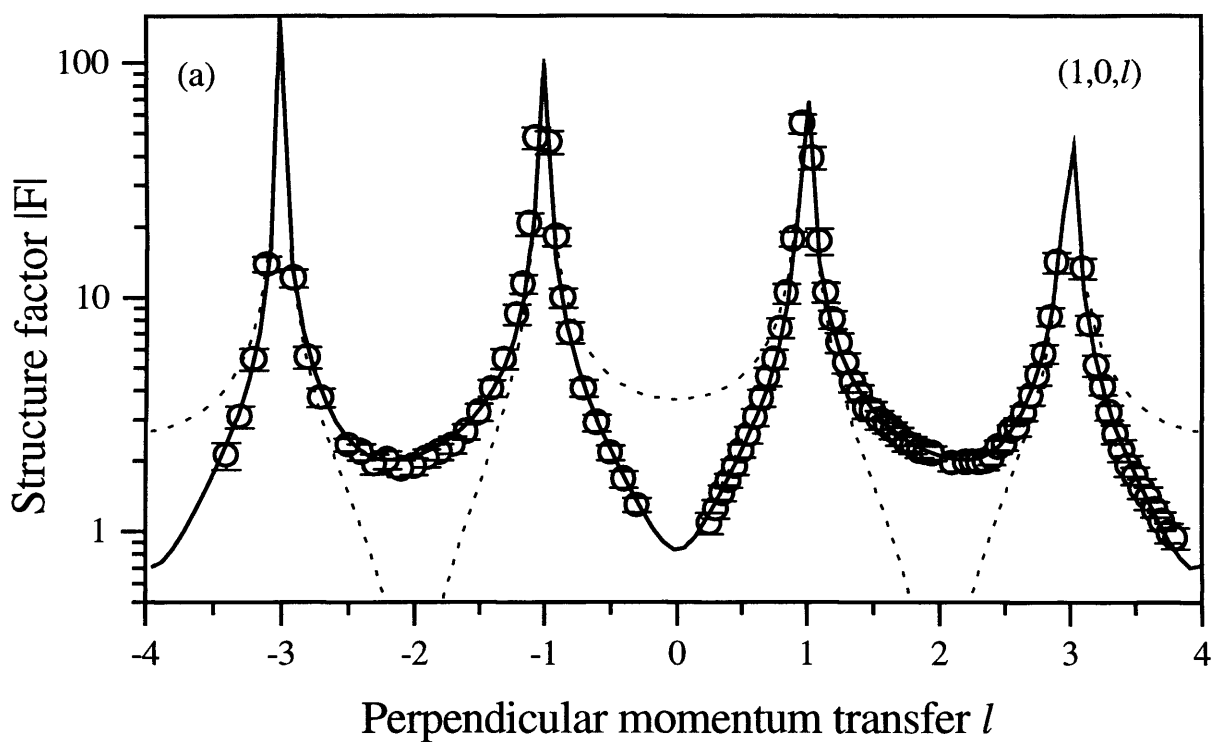
Fig 5.7 : *Structure factor amplitude profiles along two integer-order rods,*
(a) the (1,0,l) rod and (b) the (1,1,l) rod. The solid line is the best fit to the data;
the dotted line is the structure factor calculated using only the bulk crystal.
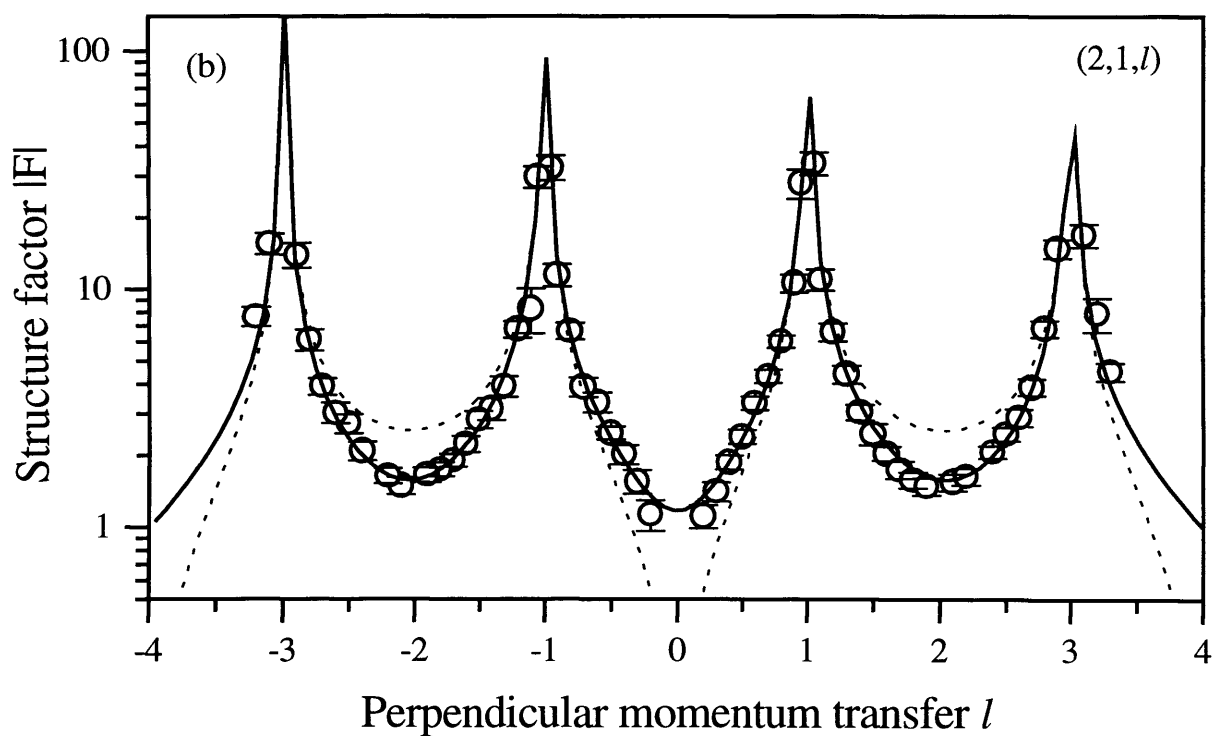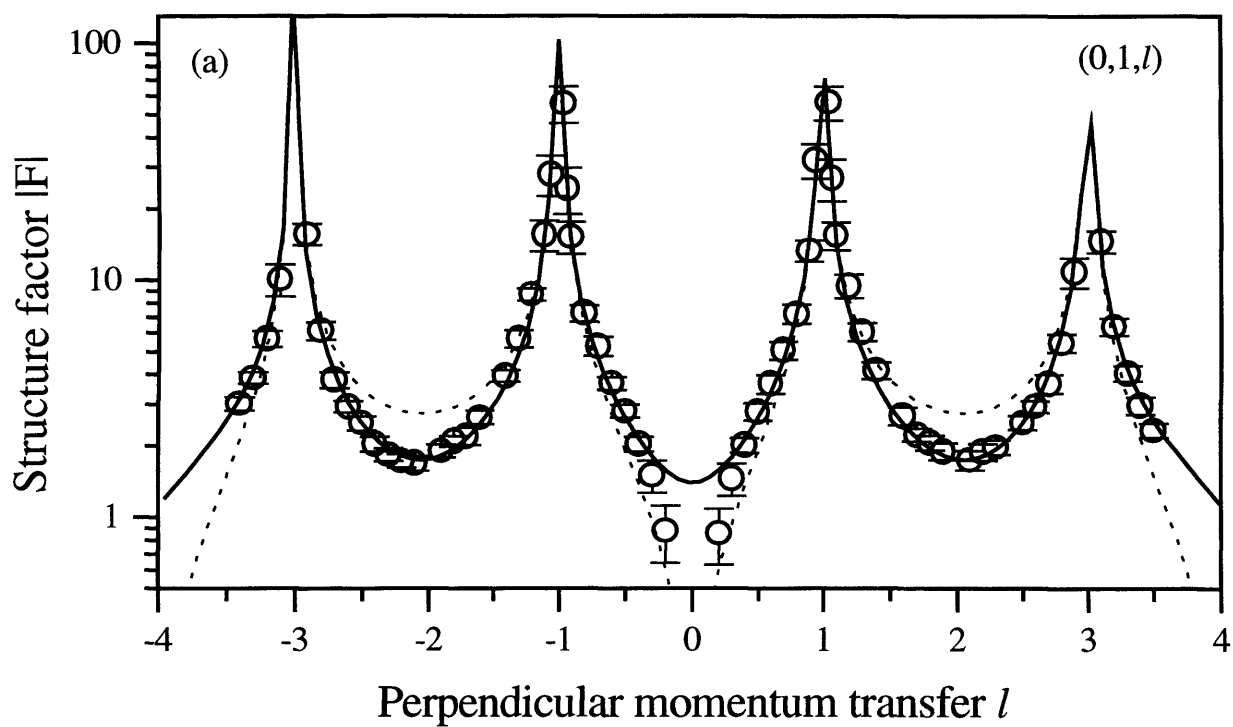
Fig 5.8: *Structure factor amplitude profiles along the (0,1,l) and the (2,1,l) integer order rods. The solid line is the best fit to the data.*
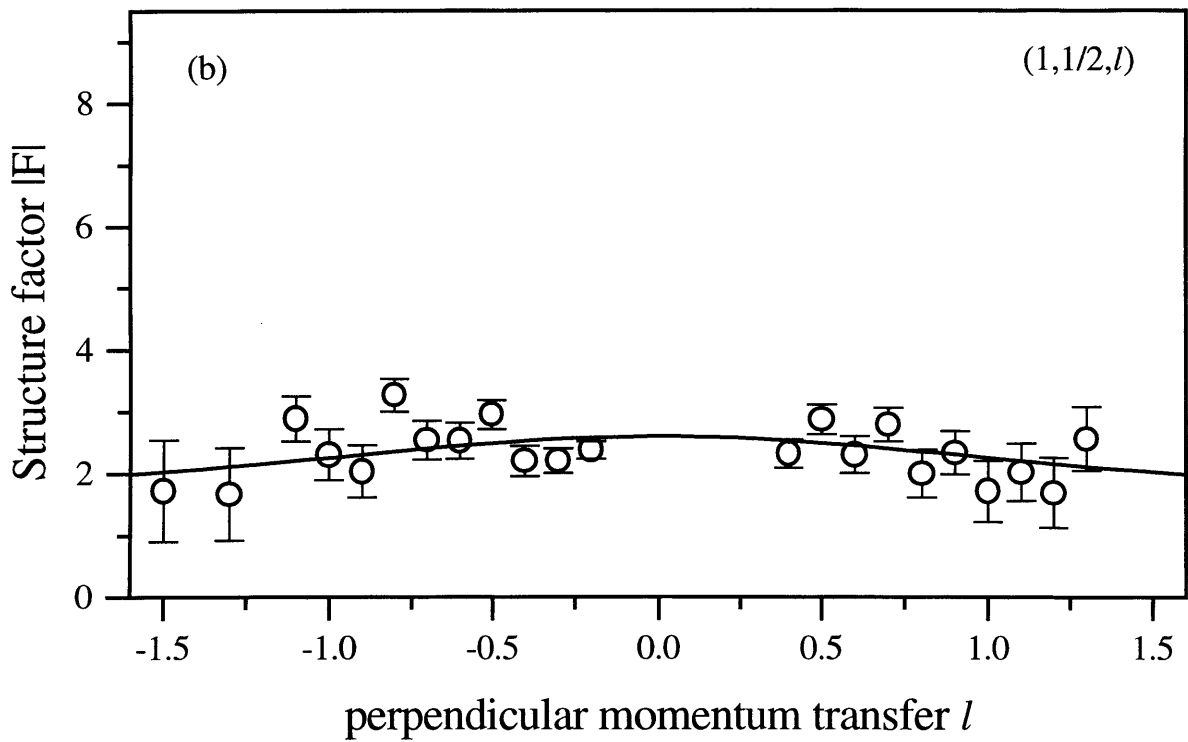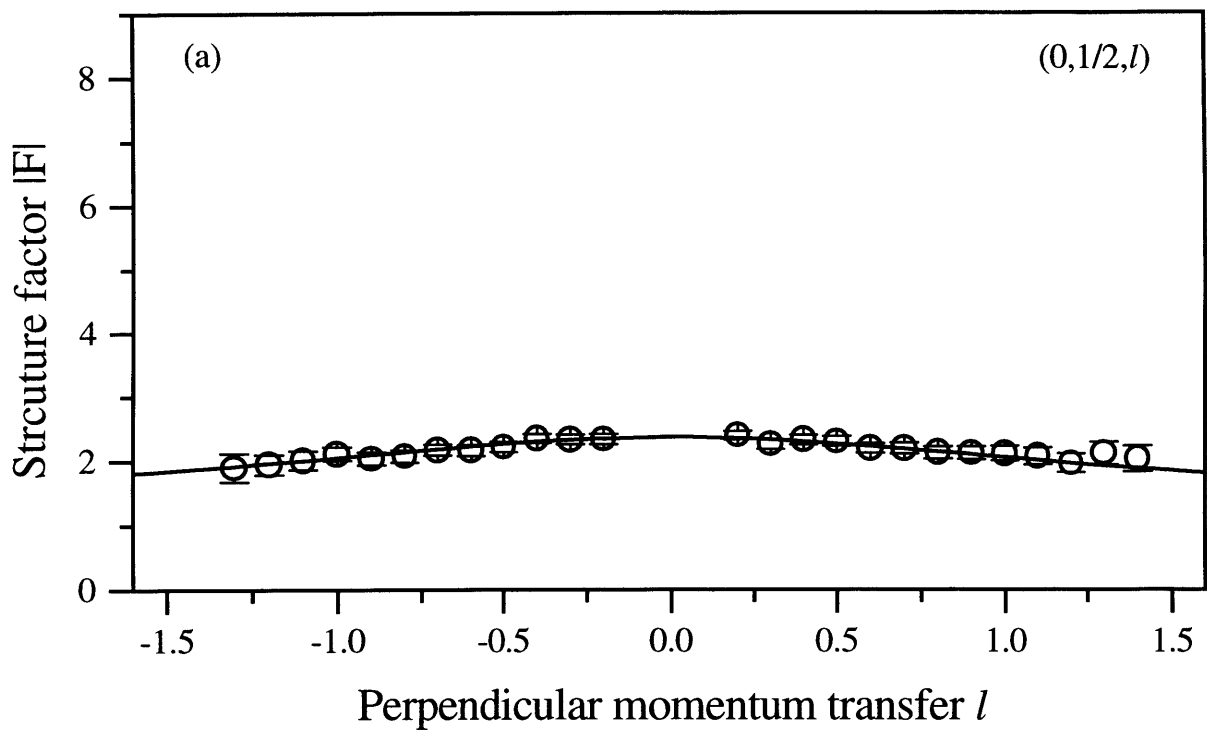
Fig 5.9: *Structure factor amplitude profiles along two fractional-order rods, (a) the (0,1/2,l) and (b) the (1,1/2,l) rod. The solid line is the best fit to the data.*

second layer, which are in similar bonding positions, were fixed together at the same height which was allowed to relax. The In atoms 3c and 3e lie vertically below the central axis of the dimer block and are not equivalent to atoms 3d and 3f which lie between the dimer blocks. We therefore allowed the rows 3c,e and 3d,f to relax independently. The vertical movement of each row was accompanied by an equal movement of the Sb row directly below to preserve the bond lengths between layers 3 and 4. All the rods were fitted simultaneously with a global scale factor and a roughness parameter β [28]. The best fits are shown in figs. 5.7 and 5.8 and are listed in Table 5.4. The χ^2 value for the fit is 1.70.

The vertical movements are small. The relaxation of the inner and outer dimers were the same and within the experimental error. Including asymmetry within a dimer did not improve the fit. There is a small inward movement of the second layer (Sb) and a buckling of the third (In) and fourth (Sb) layers of 0.15 ± 0.03Å. The average bond length between the Sb dimer atoms and the Sb atoms in the second layer was 2.93 ± 0.03Å which is again close to the bulk Sb-Sb separation. The corresponding bond angles range from $103.4°$ to $106.2°$.

Finally, the in-plane data was fitted again using the new heights derived from the out-of-plane measurements. There was no improvement in the agreement confirming our decision to analyse the data separately and consistent with a reconstruction essentially limited to the uppermost dimerised layer.

5.4   Discussion.

The results and fitting clearly favour a model for the InSb(001)-c(4x4) reconstruction which consists of regularly repeating groups of three Sb dimers on top of a complete Sb layer. This model was originally proposed for InSb(001) by John *et al* [5] from an analysis of core-level photoemission data. It is consistent with STM images, which show the same basic structure is common to InSb(001) [10] and other III-Vs, such as GaAs [13] and AlSb [15]. Models involving either a complete group V layer [27] or
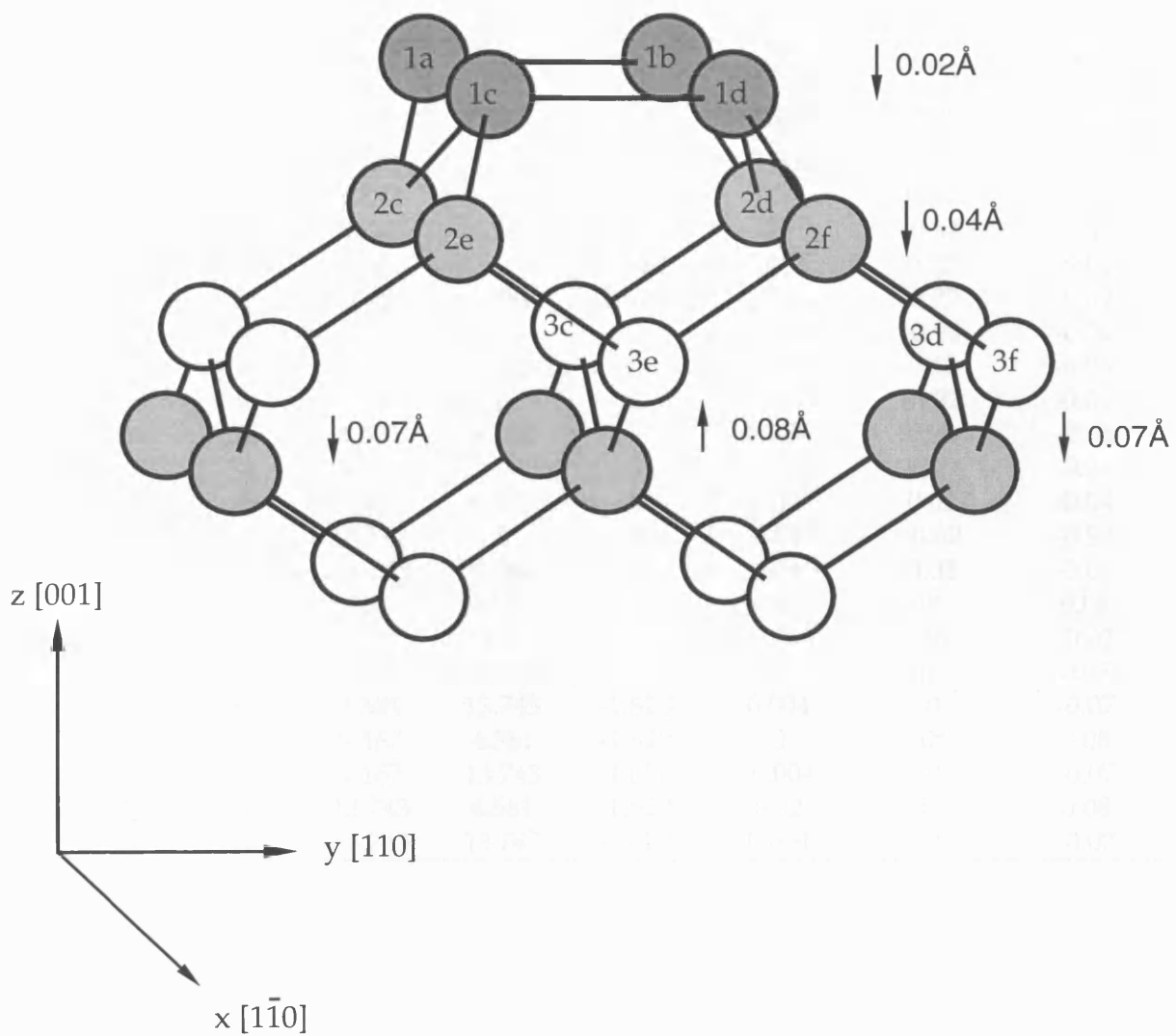
Fig. 5.9 : *Oblique view of the c(4x4) surface. For clarity only two of the three dimers are shown. The nomenclature is the same as in Fig. 5.5. The arrows denote the perpendicular atomic displacements. The crystallographic axes of the bulk cubic structure are also shown.*

Atom n°	Atom type	x	y	z	Δx_{exp}	Δy_{exp}	Δz_{exp}
1a	Sb	2.291	0	1.620	-0.006	0.72	-0.02
1b	Sb	2.291	4.581	1.620	-0.006	-0.72	-0.02
1c	Sb	6.872	0	1.620	0*	0.84	-0.02
1d	Sb	6.872	4.581	1.620	0*	-0.84	-0.02
1e	Sb	11.453	0	1.620	0.006	0.72	-0.02
1f	Sb	11.453	4.581	1.620	0.006	-0.72	-0.02
2a	Sb	0	0	0	-0.04	-0.02	-0.04
2b	Sb	0	9.162	0	-0.04	0.02	-0.04
2c	Sb	4.581	0	0	0.007	-0.02	-0.04
2d	Sb	4.581	9.162	0	0.007	0.02	-0.04
2e	Sb	9.162	0	0	-0.007	-0.02	-0.04
2f	Sb	9.162	9.162	0	-0.007	0.02	-0.04
2g	Sb	13.743	0	0	0.04	-0.02	-0.04
2h	Sb	13.743	9.162	0	0.04	0.02	-0.04
3a	In	0	4.581	-1.620	-0.02	0*	0.08
3b	In	0	13.743	-1.620	-0.004	0	-0.07
3c	In	4.581	4.581	-1.620	0	0*	0.08
3d	In	4.581	13.743	-1.620	0.004	0	-0.07
3e	In	9.162	4.581	-1.620	0	0*	0.08
3f	In	9.162	13.743	-1.620	-0.004	0	-0.07
3g	In	13.743	4.581	-1.620	0.02	0*	0.08
3h	In	13.743	13.743	-1.620	0.004	0	-0.07

Table 5.4: *The atomic coordinates of the best-fit c(4x4) model. x, y and z are the atomic positions in Å in the bulk InSb structure. Atom 2a is taken to be the origin. Δx_{exp}, Δy_{exp} and Δz_{exp} are the best-fit atomic displacements in Å. Fixed values are denoted by an asterisk. As the in-plane experimental accuracy is ±0.02Å, the only significant displacements are those 0.02Å or greater, as marked in Fig. 5.5.*

blocks of single dimers [12] gave significantly poorer agreements to the X-ray data and are ruled out.

In common with the other SXRD studies on GaAs(001) [14,20] we find the overall occupancy of the top dimer layer to be slightly lower than the nominal 75%. We interpret this as a partial occupancy of the outer dimer sites; approximately 1/3 of the dimer blocks have an outer dimer site unoccupied. This is consistent with STM images of both InSb(001) and GaAs(001). We do not propose a mixture of domains of two and three dimer units as invoked to explain the SXRD measurements of GaAs(001) [14,20].

From our analysis we derive an Sb-Sb dimer length of $3.14\pm0.02\text{\AA}$ for the outer dimers, which is approximately 8% greater than the bulk Sb nearest neighbour distance of $2.91\text{\AA}$. This result is similar to the findings of Sauvage-Simkin *et al* [14] for the As-terminated c(4x4) reconstruction of GaAs(001), who found the As-As bond of the dimer to be 3-5% larger than in bulk As. In our case, however, the centre dimer is shorter with a separation of $2.91\pm0.02\text{\AA}$, which is closer to the bulk Sb nearest neighbour distance. Payne *et al* also found the outer and centre dimers to have different separations on GaAs(001). In their case, however, the centre dimer was longer than the outer dimers. The idea of non-equivalent dimers is supported by STM pictures [10] which show the images of the central atoms to be significantly less intense than those of the outer atoms. A difference in the interatomic separation would be reflected in a difference in the electronic structure and thus the transition probability for electron tunnelling .

Each dimer atom is bonded to two Sb atoms in the first bulk layer. The bond lengths between these atoms are calculated to be between 2.90 and $2.93\text{\AA}$ with corresponding average bond angles of $104.8\pm1°$. This value is closer to the ideal value of $109.47°$ for sp^3 hybrid orbitals than that of $90°$ for $p_x p_y p_z$ orbitals. It is therefore suggested that the group V dimer atom electrons remain in sp^3 orbitals with three of the sp^3 electrons contributing to the bonding. The remaining sp^3 electron forms a lone-pair orbital with the remaining s electron, similar to the arrangement suggested from the STM results [10]. The bonding is different to that suggested for the InSb(111)-c(2x2)

reconstruction [29], however that surface has a structure very different from the dimer arrangement of this study. Other evidence suggests that sp^3 hybrids are generally present for Sb bonding with delta-doping of Si(001) with Sb [30] showing sp^3 hybrids are possible. Lohmeier *et al* [31] have reported that Sb dimers form a (2x1) reconstruction on the Ge(001) surface. In their case the Sb dimer was asymmetric and laterally shifted with one atom having sp^3-type bonds and the other 90° p-type bonds. The findings do, however, suggest sp^3-type bonds are possible for Sb dimer atoms.

The structure is characterised by a relatively small subsurface relaxation; the atomic arrangement below the first (dimer) layer is close to that of bulk InSb. The lateral distortions in the second and third layers are accommodated by the perpendicular buckling of the third and fourth layers. The origin of this small distortion is the bonding between the Sb atoms in the dimer layer and the Sb atoms in the second layer. Each dimer atom achieves three nearest neighbours with bond lengths which are close to the bulk Sb value 2.87Å without a large movement of the Sb atoms in the second layer from their bulk InSb positions. Differences in electronegativities and covalent radii can also lead to strain [32], but these factors should not be important here as the outer layers are entirely composed of Sb. Since In and Sb atoms are close in the periodic table, their X-ray factors (away from absorption edges) are almost identical. We therefore, cannot definitely rule out models containing both atom types in the second layer, such as the one proposed by Falta *et al* [33]. The bond lengths, however, strongly support the proposal that the two outermost layers are entirely populated by Sb.

Finally we note that the Sb rich c(4x4) surface is the one used as a starting surface for epitaxial growth. The In rich c(8x2) reconstruction, produced by argon bombardment and annealing, is similarly well ordered with large domain sizes and could also be considered as a starting surface. Unlike the c(4x4) structure, the c(8x2) reconstruction extends further into the substrate [13,34], (chapter 7), which leads to a more disturbed interface and poorer growth.

5.5 Summary.

The structure of the InSb(001)-c(4x4) surface has been determined using SXRD. It has been shown that the c(4x4) surface is formed by the chemisorbtion of ~3/4 of a monolayer of Sb on top of an Sb terminated bulk. The reconstruction is dominated by a regular array of blocks of three Sb dimers supported on top of a complete Sb layer. This is in agreement with other experimental studies of the c(4x4) surface of InSb and other III-V semiconductors. The dimer atoms are bonded to three other Sb atoms with a bond length close to the value of the near neighbour distance in the rhombohedral Sb bulk. The measured bond angles indicate sp^3 type bonding. The disturbance of the structure below the dimer layer is small.

References.

[1]   C.Y. Wei, K.L. Wang, E.A. Taft, J.M. Swab, M.D. Gibbons, W.E. Davern and D.M. Brown, IEEE Trans. Electron Devices **27** (1980) 170.

[2]   K. Asauskas, Z. Dobrovolskis and A. Krotkus, Sov. Phys. Semicond. **14** (1980) 1377.

[3]   K. Oe, S. Ando and K. Sugiyama, Jap. J. Appl. Phys. **19** (1980) L417.

[4]   A.J. Noreika, M.H. Francombe and C.E.C. Wood, J. Appl. Phys. **52** (1981) 7416.

[5]   P. John, T. Miller and T.C.Chiang, Phys. Rev. **B39** (1989) 1730.

[6]   R.G. Jones, N.K. Singh and C.F. McConville, Surf. Sci. **208** (1989) L34.

[7]   A.G. de Oliveira, S.D. Parker, R. Droopad and B.A. Joyce, Surf. Sci. **227** (1990) 150.

[8]   B.F. Mason, S. Laframboise and B.R. Williams, Surf. Sci. **258** (1991) 279.

[9]   M.O. Schweitzer, F.M. Leibsle, T.S. Jones, C.F. McConville and N.V. Richardson, Surf. Sci. **280** (1993) 63.

[10] C.F. McConville, T.S. Jones, F.M. Leibsle and N.V. Richardson, Surf. Sci. **303** (1994) L373.

[11] W.K. Liu and M.B. Santos, Surf. Sci. **319** (1994) 172.

[12] P.K. Larsen, J.H. Neave, J.F. van der Veen, P.J. Dobson and B.A. Joyce, Phys. Rev. **B27** (1983) 4966.

[13] D.K. Biegelsen, R.D. Bringans, J.E. Northrup and L.-E. Swartz, Phys. Rev. **B41** (1990) 5701.

[14] M. Sauvage-Simkin, R. Pinchaux, J. Massies, P. Calverie, N. Jedrecy, J. Bonnet and I.K. Robinson, Phys. Rev. Lett. **62** (1989) 563.

[15] P.M.Thibado, B.R. Bennett, B.V. Shanabrook and L.J. Whitman, submitted to J. Crystal Growth, July 96.

[16] A.R. Avery

[17] R. Feidenhans'l, J.S. Pedersen, J. Bohr, M. Nielsen, F. Grey and R.L. Johnson, Phys. Rev. **B38** (1988) 9751.

[18] R.G. van Silfhout, J.F. van der Veen, C. Norris and J.E. Macdonald, Faraday Discuss. Chem. Soc. **89** (1990) 169.

[19] F.J. Lamelas, P.H. Fuoss, D.W.Kisker, G.B. Stephenson, P. Imperatori and S. Brennan, Phys. Rev. **B49** (1994) 1957.

[20] A.P. Payne, P.H. Fuoss, D.W. Kisker, G.B. Stephenson and S. Brennan, Phys Rev **B49** (1994) 14427.

[21] S.D. Evans, L.L. Cao, R.G. Egdell, R. Droopad, S.D. Parker and R.A. Stradling, Surf. Sci. **226** (1990) 169.

[22] J.S.G. Taylor, C. Norris, E. Vlieg, M. Lohmeier and T.S. Turner, Rev. Sci. Instr. **67** (7) (1996) 2658.

[23] I.K. Robinson, *Handbook on Synchrotron Radiation*, volume III, North-Holland, Amsterdam, 1989.

[24] B.E. Warren, *X-ray Diffraction*, Addison-Wesley, Reading, 1969.

[25] International Tables of Crystallography, Vol. A, Reidel Publ. Co., Boston (1983) 4th Rev. Ed. edited by Theo Hahn.

[26] R.W.G. Wyckoff, Crystal Structures, Interscience Publishers, New York, 2nd Ed. 1969.

[27] D.J. Chadi, C. Tanner and J. Ihm, Surf. Sci. **120** (1982) L425.

[28] I.K. Robinson, Phys. Rev. **B33** (1986) 3830.

[29] J. Bohr, R. Feidenhans'l, M. Nielsen, M. Toney, R. L. Johnson and I.K. Robinson, Phys. Rev. Lett. **54** (1985) 1275.

[30] W.F.J. Slijkerman, P.M. Zagwijn, J.F. van der Veen, A.A. van Gorkum, and G.F.A. van de Walle, Appl. Phys. Lett. **55** (1989) 963.

[31] M. Lohmeier, H.A. van der Vegt, R.G. van Silfhout, E. Vlieg, J.M.C. Thornton, J.E. Macdonald and P.M.L.O. Scholte, Surf. Sci. **275** (1992) 190.

[32] R.D. Meade and D. Vanderbilt, Phys. Rev. Lett. **63** (1989) 1404.

[33] J. Falta, R.M. Tromp, M. Copel, G.D. Pettit and P.D. Kirchner, Phys. Rev. Lett. **69** (1992) 3068.

[34] S.L. Skala, J.S. Hubacek, J.R. Tucker, J.W. Lyding, S.T. Chou and K.Y. Cheng, Phys. Rev. B48 (1993) 9138.

[35] I.K. Robinson, Phys. Rev. Lett. **57** (1986) 2714.

Chapter 6.

Order-disorder phase transition of the

InSb(001)-c(4x4) reconstruction.

Surface X-ray diffraction has been used to study the c(4x4) reconstruction of the InSb(001) surface through its phase transition to the *asymmetric*(1x3) phase at about 350°C. The evolution of the integrated intensity and lineshape of the c(4x4) specific surface reflection as a function of temperature indicates that the surface undergoes a continuous order-disorder transition with a critical transition temperature T_t.

The results clearly suggest that the surface disordering is a result of a definite change in structure associated with the desorption of Sb dimer atoms in distinct isolated regions, rather than a general reduction in the domain size. It is found that T_t is proportional to the applied flux of antimony, and the transition is fully reversible under the external antimony flux.

6.1   Introduction.

The reversible disordering transition of the InSb(001)-c(4x4) surface has been investigated using X-ray diffraction. The antimony rich c(4x4) reconstruction of the clean InSb(001) surface has been extensively studied [1-5] since its discovery by RHEED [6]. The c(4x4) surface phase exists between a temperature of ~ 250-370°C and the basic atomic structure is no longer seriously disputed, fig. 5.5. A complete structural analysis of the c(4x4) reconstruction is described in detail in chapter 5.

The surface phase diagram for the InSb(001) surface is shown in fig. 2.2. It can be seen that an *asymmetric*(1x3) surface phase exists in place of the c(4x4) phase at elevated temperatures. This phase will be referred to as the A(1x3) phase hereafter. The existence of the A(1x3) phase was first reported by Oe *et al* [6] who observed diffuse and unevenly spaced third order streaks in their diffraction patterns in a high temperature region, (substrate temperature T_s > 360°C), when the Sb/In ratio was greater than unity. These findings were supported by later RHEED measurements performed by Noreika *et al* [7] and De Oliveira *et al* [8] for the same InSb surface. The latter group proposed a model based on repeating subunits of a (2x4) structure to explain the A(1x3) surface structure; the threefold periodicity being generated by domain formation and the amount of splitting explained by the degree of Sb coverage. The splitting of the half order streak into two unevenly spaced third order streaks in the RHEED patterns is believed to arise due to a surface phase transition from the highly ordered c(4x4) structure to a significantly less ordered A(1x3) structure. Disordering in the surface region will generally cause a decrease in the diffracted beam intensity. The RHEED patterns therefore provide direct evidence of surface disordering during the formation of an A(1x3) surface.

High resolution STM measurements of both the c(4x4) phase and the A(1x3) phase of the InSb(001) surface have been presented by McConville *et al* [3]. The STM images of the c(4x4) surface consist of individual sets of regular features which exist over the entire range of sampling (400Å x 400Å), indicative of an ordered phase. In contrast, the images of the A(1x3) phase indicate the surface has significant short range disorder with Sb atoms aligned in short uneven chains, the length of which vary in

size from as small as three or four atoms up to several tens of atoms in length. The results also show the A(1x3) phase exists on the same surface, but in a distinct region, as the indium rich c(8x2) surface phase. Similar coexistence of the c(4x4) and A(1x3) phases is not observed. Helium atom scattering, (HAS), measurements performed by Mason et al [9], however, show definite coexistence of c(4x4) and A(1x3) phases. In addition, the results indicate the latter surface phase forms at much lower temperatures than indicated by the published surface phase diagrams. The HAS measurements were carried out at different antimony fluxes.

There are, in general, two mechanisms that can be applied to explain the disordering of surfaces of solids as a function of temperature: surface roughening [10] and surface melting [11]. Thermal roughening of crystal surfaces has been studied for a wide range of materials including both semiconductors and metals [12-16]. Thermal roughening transitions have been found to occur at temperatures well below the melting point of the bulk crystal. A theory that a surface melts at a temperature below the melting point has also been proposed [11]. The conditions for surface melting require the sum of the free-energies of the solid/liquid and liquid/vapour interfaces to be less than that of the solid/vapour interface; in effect enabling the surface to create a liquid layer upon itself. This process is observable as a continuous disordering transition just below the melting point of the bulk crystal [17].

An in situ X-ray diffraction study of the disordering of the InSb(001)-c(4x4) surface phase is presented here. As surface structures with different two-dimensional periodicities diffract in separate parts of reciprocal space, surface X-ray diffraction is a especially useful technique to simultaneously monitor the decay of a particular phase and the onset of another.

6.2   Experimental.

The measurements were carried out on the W12 surface diffraction beam line at the LURE-DCI synchrotron radiation facility (Orsay, France) [18]. Radiation from a five pole wiggler of 5T was directed through a two crystal monochromator equipped

with a sagitally focusing Si(111) crystal which focused a beam of 1 mrad horizontal onto the sample. The available energy range of the beam was 6.5-20 keV from which a wavelength of 0.9Å (~ 14 keV) was selected. The flux intercepted by the sample under grazing incidence was ~ 10^9 photons per second.

The InSb(001) sample of dimensions 10 x 10 x 0.5 mm^3 was cut from an antimony capped wafer prepared as described in section 5.2. The sample was bonded to a Mo block using a thin In seal and loaded into the preparation stage of an MBE chamber. The native oxide layer on the sample was removed by argon ion bombardment (P_{Ar} = 5 x 10^{-5} mbar, 3 μAcm^{-2}, 30 min) and annealing (250°C, 25 min). The sample was transferred into the diffractometer stage of the MBE chamber with a base pressure of ~3 x 10^{-10} mbar. The amorphous Sb cap was removed by holding the sample under an antimony flux (T_{cell} = 420°C) and heating (T_s = 320°C, 25min). After shutting off the vapour source and cooling the sample to room temperature, X-ray diffraction measurements confirmed the surface phase to be c(4x4).

In-plane (hk) X-ray fractional order reflections were taken over three quadrants in reciprocal space. The grazing angle of incidence used was β_{in} = 0.47° which is above the critical angle for InSb (0.19°). The results were found to be consistent with those previously recorded for the c(4x4) surface (Chapter 5). The sample was returned to 300°C and the antimony flux (T_{cell} = 420°C) applied. The same set of in-plane X-ray reflections were taken and were consistent with those taken at room temperature.

An intense in-plane reflection at (2, 1.5, 0.07), as defined by the conventional tetragonal surface unit cell, (section 5.2), was measured by rotating the crystal about the sample surface normal. The integrated intensity of the reflection was obtained by numerically integrating the peak after linear background subtraction. Several reflections over the period of about an hour were taken establishing the intensity of the reflection was time independent. The temperature was then increased in steps of ~ 2°C. At each step, the temperature was allowed to stabilise (~ 30 min) and the (2, 1.5, 0.07) reflection scanned as before. This procedure was repeated until the peak intensity could no longer be distinguished above the background level. The reflection was scanned in the same way on cooling the sample back to ~ 300°C. Scans along the

(2, k, 0.07) and (h, 1, 0.07) reciprocal space lattice axes were also taken at each temperature step, over a wide temperature range (330°C - 450°C), in order to monitor any formation of an A(1x3) or c(8x2) surface phase.

The entire procedure was repeated with the same sample held under a lower incident antimony flux (T_{cell} = 380°C) and in the absence of an antimony flux, the substrate temperature being adjusted accordingly.

6.3 Results.

The decay in intensity of the (2, 1.5, 0.07) fractional-order reflection of the c(4x4) surface is shown as a function of both temperature and antimony flux in figs. 6.1(a)-(c). The curves have been offset for clarity, the measured background level of each curve being of the order of 200 counts per second. For each temperature, the position of the detector was corrected to allow for any small thermal expansion of the InSb lattice. It is evident from fig. 6.1 that there is a narrow temperature range over which the peak height disappears into the background. It is expected that the transition temperature T_t from an ordered c(4x4) phase to a disordered phase would lie within this range.

A quantitative analysis was performed by fitting Lorentzian lineshapes to the curves in fig. 6.1. The initial correlation length of each reconstruction is calculated from the width of the first measured reflection using the formula $L = 2/\Delta Q$, where ΔQ is the full width half maximum (FWHM). The results are shown in Tab. 6.1. The integrated intensities of the (2, 1.5, 0.07) reflection are shown as a function of substrate temperature for each of the three antimony flux rates in fig. 6.2. The shape of the curves indicate that the InSb(001) surface exhibits a continuous surface phase transition with a critical transition temperature T_t. For such a continuous lateral disordering transition, the intensity of the scattered beam falls to zero as described by the function [19] :
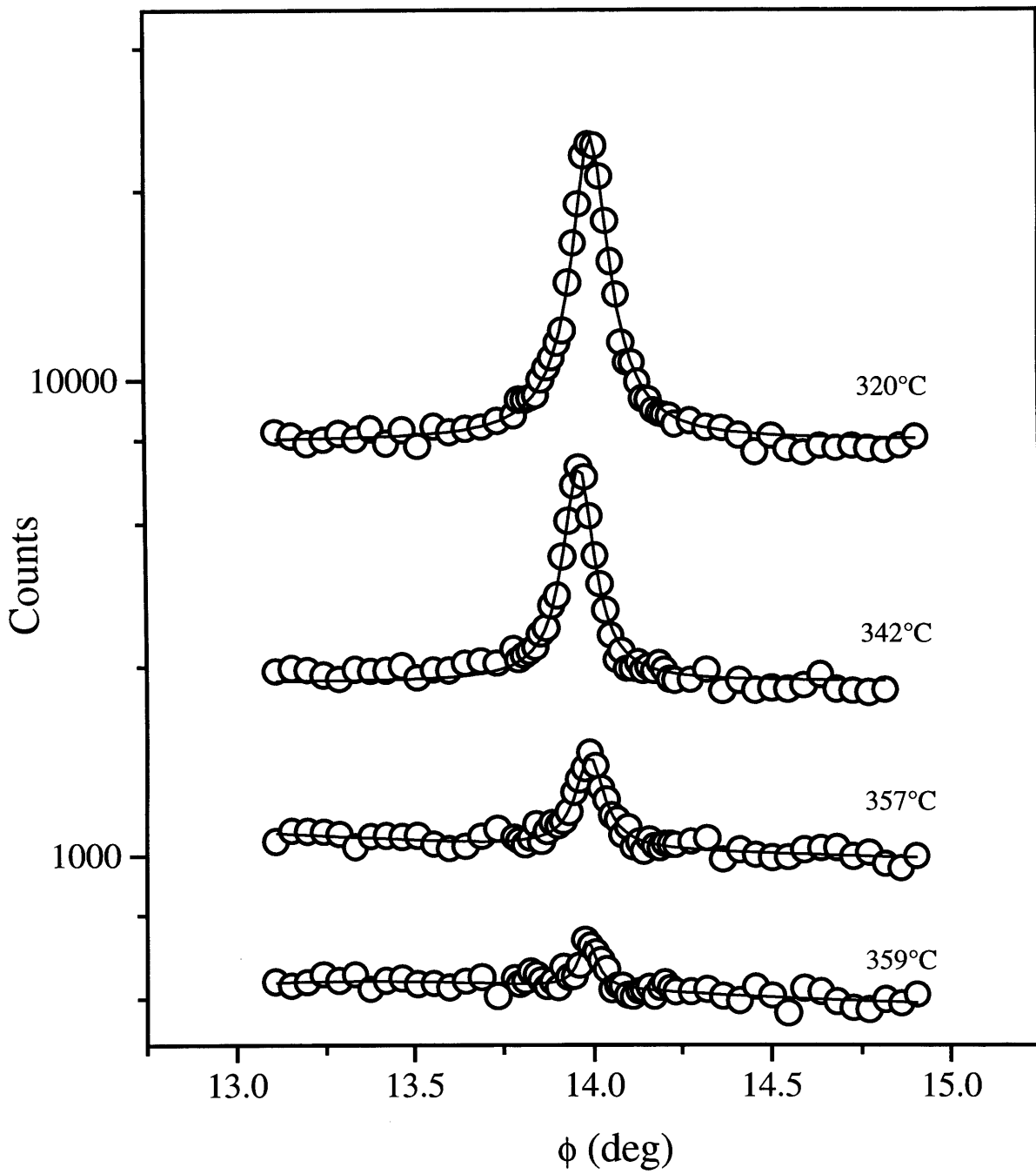
Fig. 6.1(a): *Variation of the (2, 1.5, 0.07) reflection peak with temperature under a high Sb flux, (cell temperature = 420°C)*
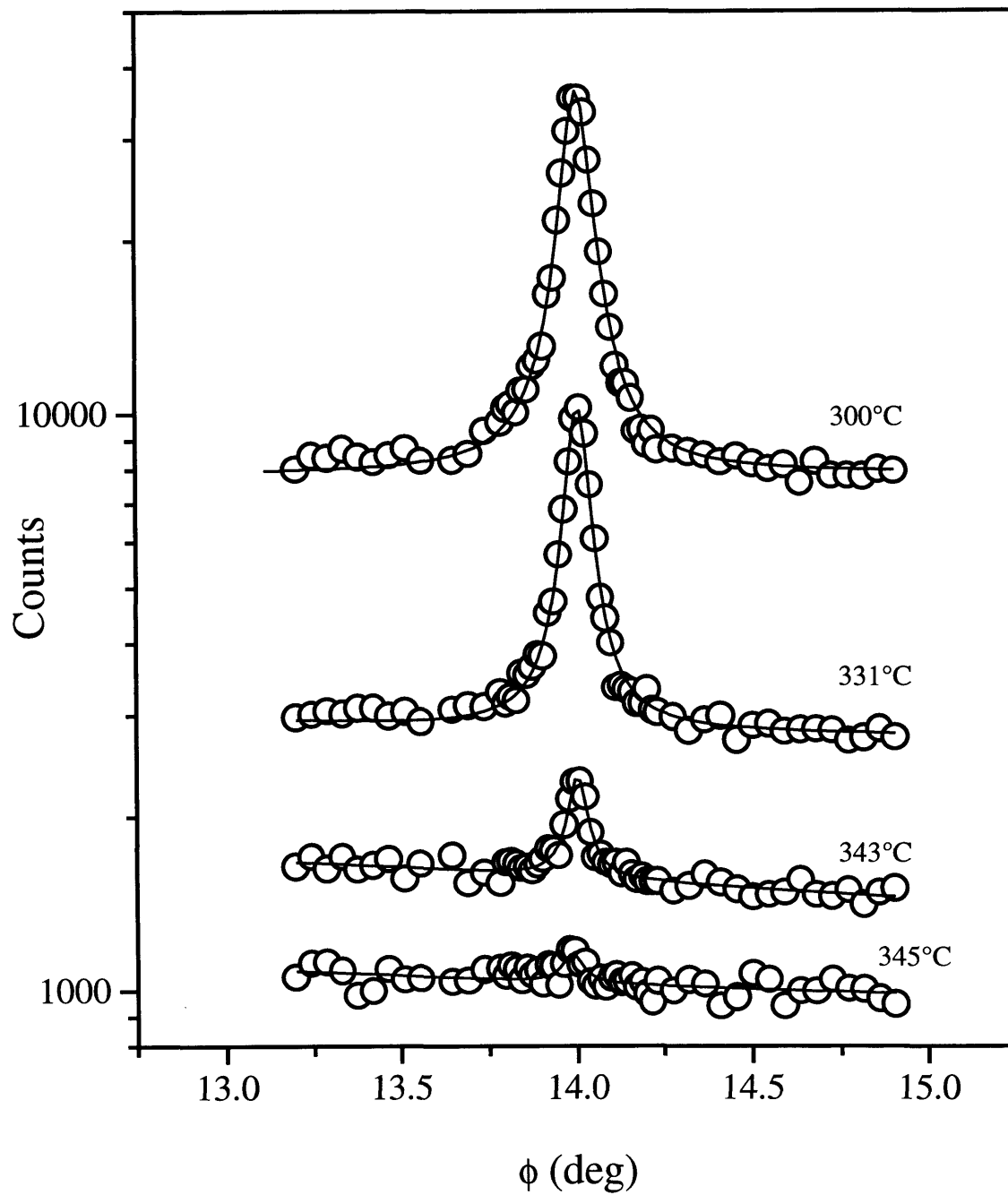
Fig. 6.1(b): *Variation of the (2, 1.5, 0.07) reflection peak with temperature under a low Sb flux (cell temperature = 420°C)*
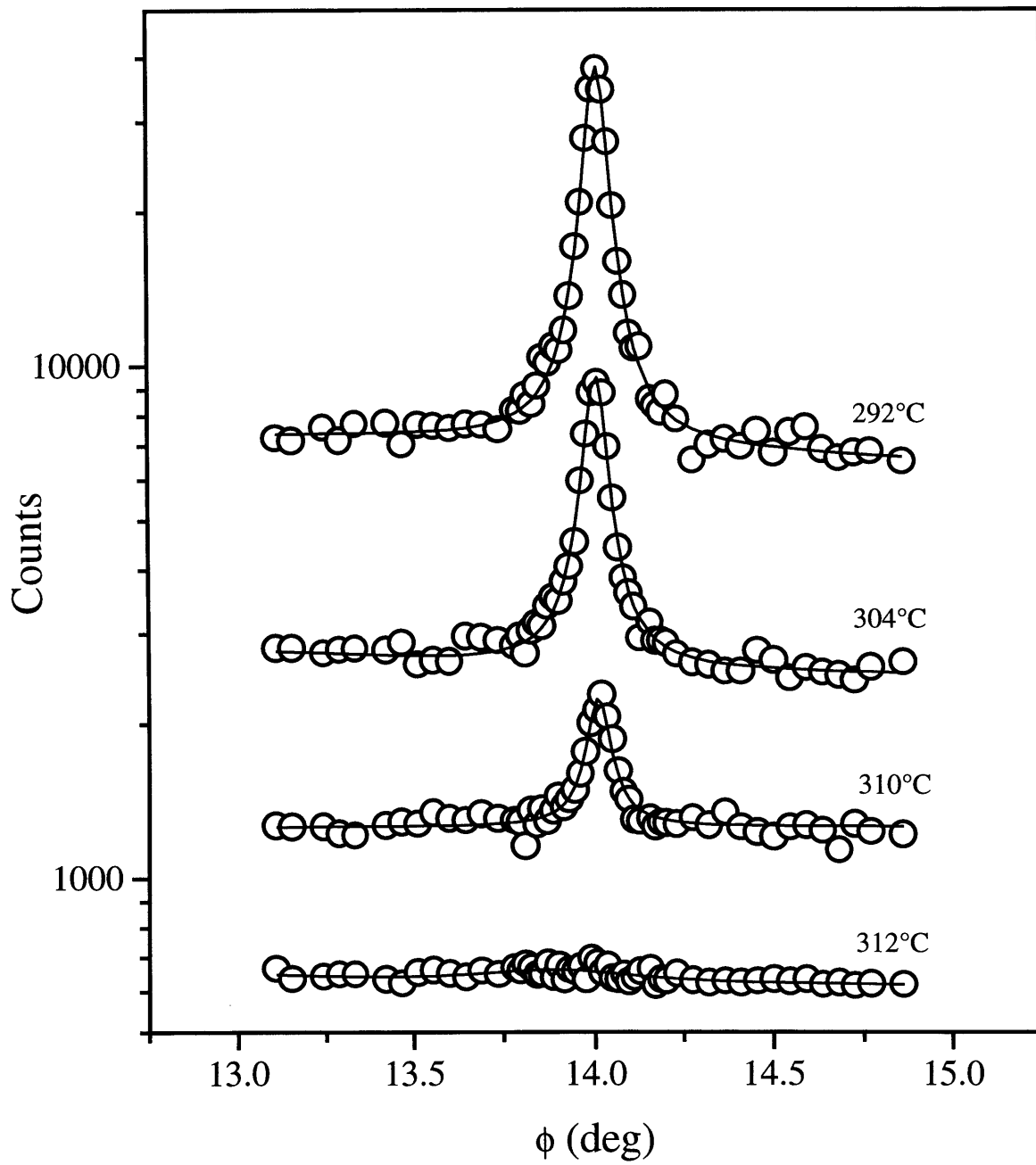
Fig. 6.1(c): *Variation of the (2, 1.5, 0.07) reflection peak with temperature with no external Sb flux applied.*

$$\left(1 - \frac{T}{T_t}\right)^{2\beta} \tag{6.1}$$

where T is the absolute temperature, T_t is the transition temperature and β is a critical exponent associated with the transition.

Including the effect of thermal vibrations, the integrated intensity becomes

$$I_{int} = I_0 \exp(-2MT)\left(1 - \frac{T}{T_t}\right)^{2\beta} \tag{6.2}$$

where the Debye-Waller constant M, is related to the root mean square thermal vibration of the atoms by:

$$\langle u^2 \rangle^{\frac{1}{2}} = \left(\frac{2MT}{q^2}\right)^{\frac{1}{2}} \tag{6.3}$$

and q is the momentum transfer.

The solid lines in fig. 6.2 are the fits to the data given by eq. (6.2). The resulting values of M are $0.0018 \pm 0.002 K^{-1}$ corresponding to a root mean square atomic displacement of $\langle u^2 \rangle^{\frac{1}{2}} = 0.30 \pm 0.02$Å at 300K in comparison to the bulk value of 0.17Å [20]. It is noted that the transition temperature T_t increases with the incident flux rate with calculated values of 359.4°C, 345.4°C and 312.2°C for the high, low and zero flux rates respectively. These results are also displayed in Tab. 6.1. It can also be seen from fig. 6.2 that the transition between the c(4x4) phase and the disordered phase is
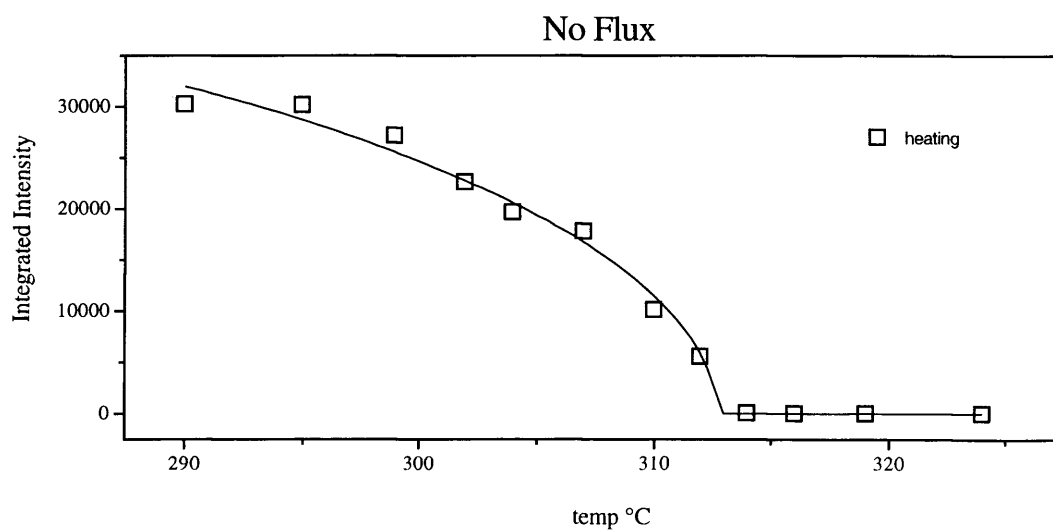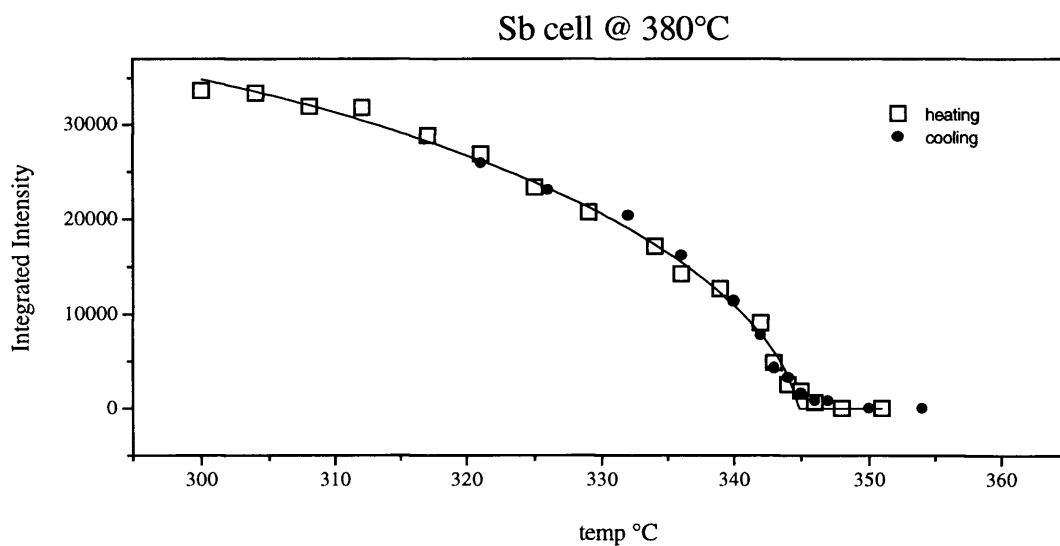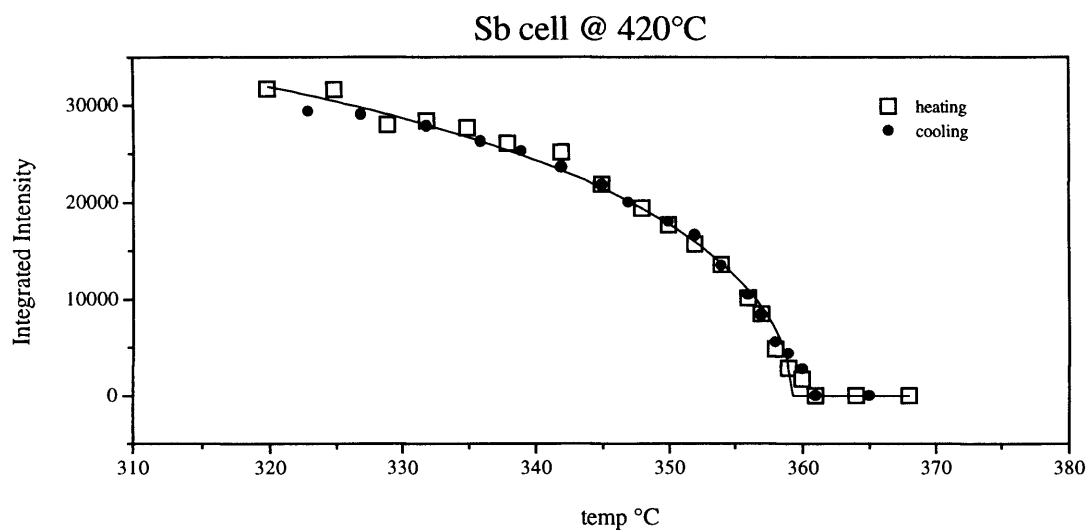
Fig 6.2: *Integrated intensities of the (2, 1.5, 0.07) reflection as a function of temperature. The solid lines are fits using the equation described in the text.*

Flux rate	Initial Correlation Length	Transition Temperature
High (T_{cell} = 420°C)	525Å	359.4°C
Low (T_{cell} = 380°C)	560Å	345.4°C
Zero	580Å	312.2°C

Table 6.1: *Critical transition temperatures for the phase transition of the InSb(001)-c(4x4) surface. The initial surface correlation length is also included.*

fully reversible on cooling the sample under the Sb flux. This is highlighted by the fact that the same sample was used for all the measurements. The c(4x4) surface phase was recovered from the disordered phase obtained under zero flux conditions by cooling under an external Sb flux (T_{cell} = 400°C).

The evolution of the width of the diffracted peaks with temperature is shown in fig. 6.3. It can be seen that the FWHM remains constant, within experimental error, with increasing temperature until very close to the transition temperature, T_t , where there is a sharp rise in the FWHM. The large error close to T_t reflects the fall in intensity of the diffraction peak. This result suggests the correlation length of the reconstruction remains approximately constant below T_t despite the fall in peak intensity, which implies that the destruction of the c(4x4) surface phase occurs in distinct isolated regions rather than in an overall reduction of domain size.

Reciprocal space lattice scans taken at various temperatures along the (2, k, 0.07) axis with an external Sb flux incident on the sample, (T_{cell} = 420°C), are shown in figs. 6.4 (a) - (f). Fig. (a) shows only a strong 1/2 order diffraction peak, characteristic of the c(4x4) surface. In fig. (b) the quarter order peak has fallen slightly in intensity and a small ~1/3 order feature, characteristic of an A(1x3) phase is present. This peak is referred to as a 1/3 order peak herein, but it is noted that as the reconstruction is an asymmetric one the peak is not a true 1/3 order peak. Figs. (c) and (d) show a broad weak, but definite, 1/3 order feature exists in addition to the rapidly decaying 1/2 order peak. This provides us with direct evidence of the coexistence of c(4x4) and A(1x3) surface domains. In figs. (e) and (f) the 1/2 order peak has disappeared into the level of the background and the 1/3 order peak is broad and weak in intensity indicative of a disordered surface (T_s ~ 370°C).

Finally, reciprocal lattice scans in the h and k directions were taken at higher temperatures, in steps of 3°C, up to T_t + 90°C (~ 450°C). The resulting scans, however, were flat with no outstanding features. After the annealing at T_t + 90°C macroscopic damage was observed on the sample implying permanent gross In nucleation had occurred.
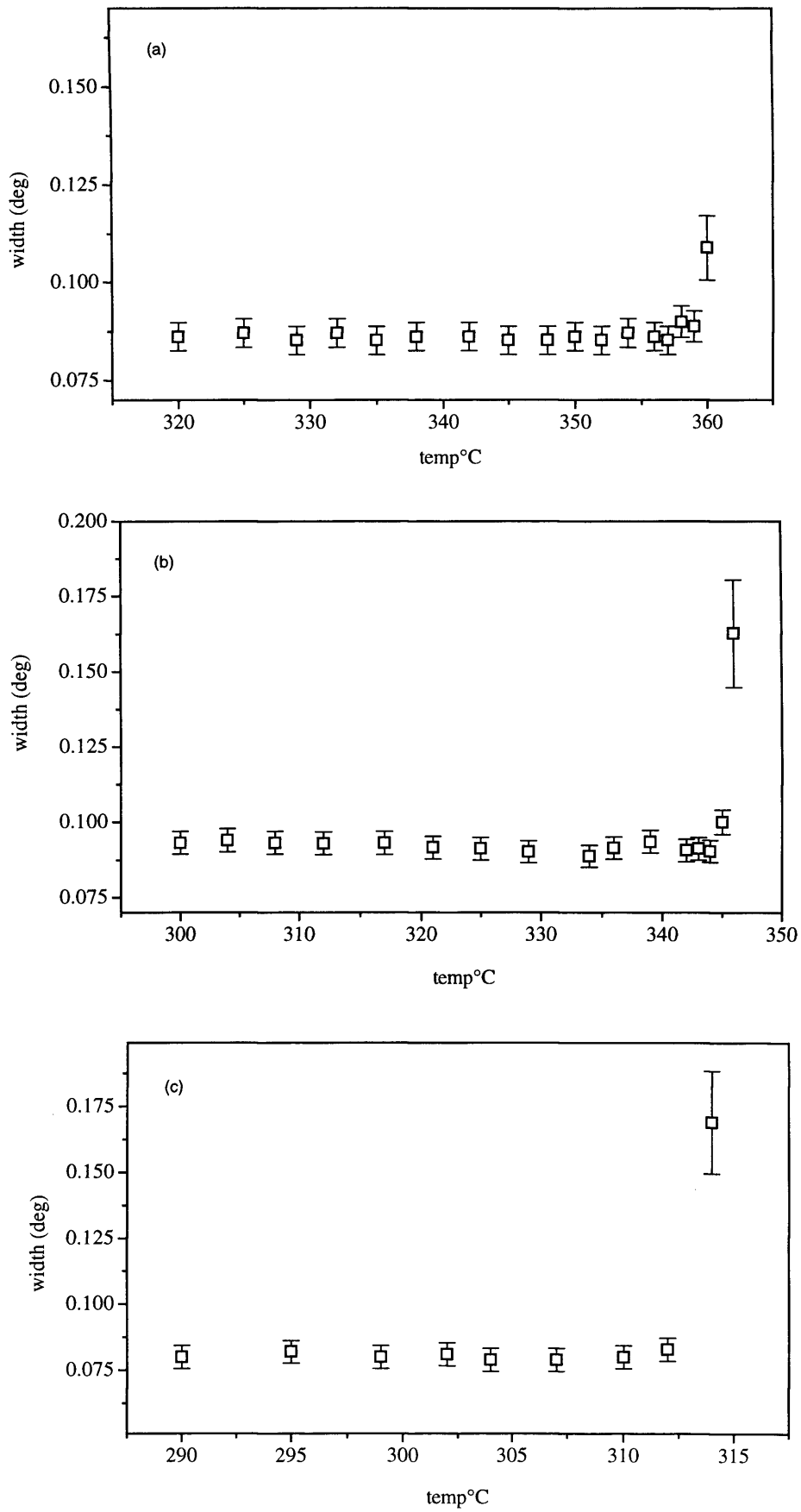
Fig. 6.3: *Variation of the full width of the (2, 1.5, 0.07) reflection as a function of temperature for: (a) high Sb flux, (b) low Sb flux and (c) no Sb flux.*
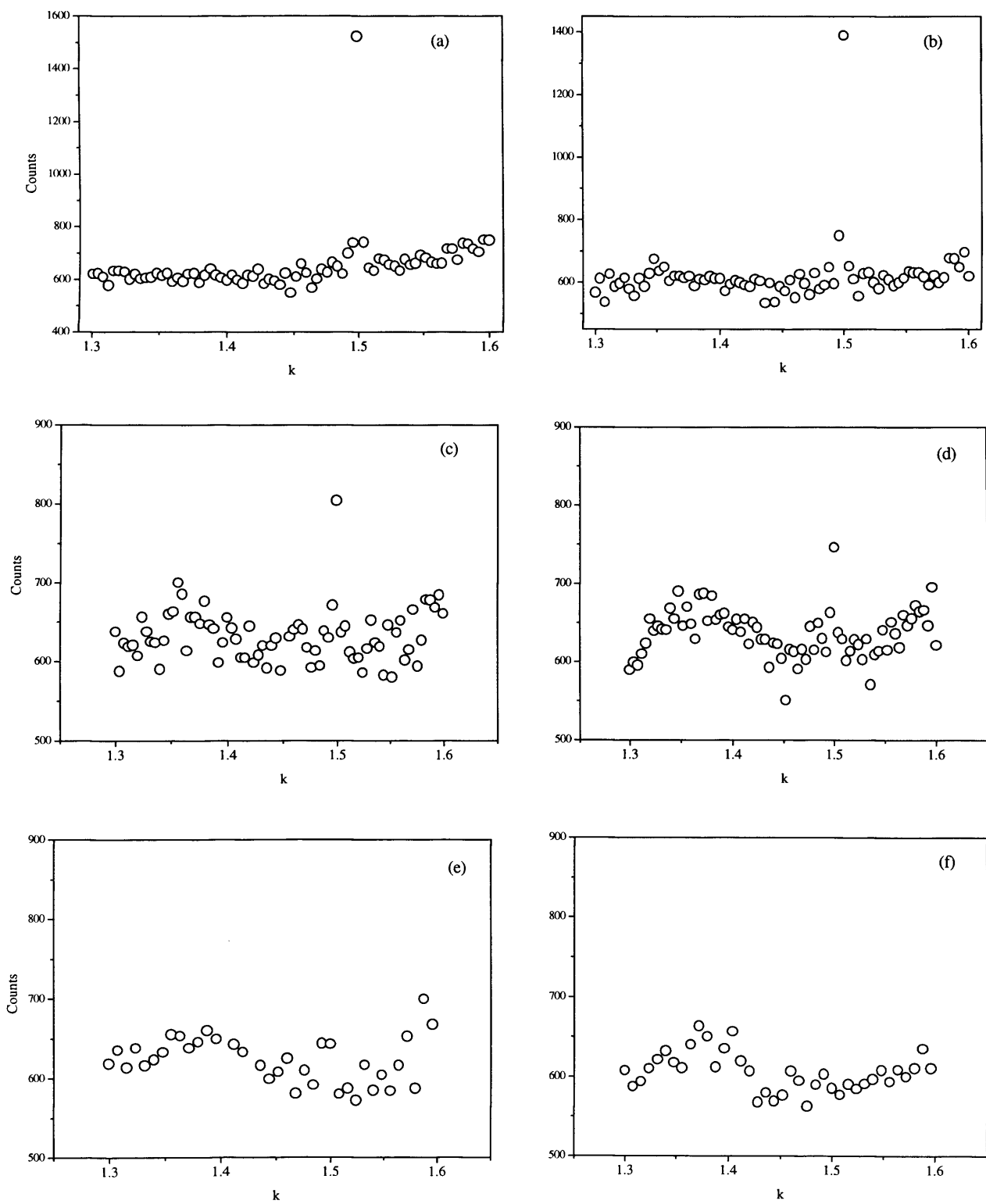
Fig. 6.4: *Reciprocal space lattice scans along the (2, k, 0.07) axis.*
(a) 355°C, (b) 357°C, (c) 358°C, (d) 359°C, (e) 360°C and (f) 362°C.

6.4   Discussion.

The results indicate that the InSb(001) surface undergoes a continuous phase transition from an ordered c(4x4) phase to a disordered phase when heated both under and in the absence of an external antimony flux. The transition is proposed to be due to thermal disordering; increasing temperature causing progressive desorption of the Sb dimer atoms. The resulting surface is disordered, however, the transition is fully reversible under an external antimony flux. The transition is not reversible when no antimony flux is applied.

It is found that although the diffracted peak intensity falls continuously over the range studied, the half-width of the reflection, and hence the correlation length of the reconstruction, remains approximately constant. The half-width only rises when the integrated intensity of the reflection has dropped to less than 5% of its initial value. This is in stark contrast to the order-disorder transition observed on the W(001) surface by Robinson *et al* [13] who found that although the peak intensity decreased significantly over the temperature range studied, the integrated intensity of the peak remained approximately constant. This was achieved as the width of the peak increased with temperature resulting in a set of peaks with almost constant volume. The reason why the above order-disorder transition gave notably different results to the study presented here is the fact that in the above study there is no local change in structure (as the structure factor remains roughly constant). For the order-disorder transition here, there is a definite change in structure associated with the gradual desorption of the Sb dimer atoms.

The c(4x4) to A(1x3) transition is similar to the (2x1) to (1x1) deconstruction studied on germanium [12,13] and in particular, the results are similar to the findings of a study of the same surface of GaAs by Etgens *et al* [21] who measured the phase transformation from a c(4x4) to a (2x4) surface phase. In contrast to our study, Etgens *et al* did not find the measured phase transition to be reversible, however in their study a group-V overpressure was not incident on the sample. Etgens *et al* found that between 250°C and 350°C the integrated intensity of the (0, 3/2, 0.03) reflection constantly decreased whereas the linewidth remained constant. This result was

interpreted as a progressive disordering induced by random desorption of As dimers as As_2 molecules in the chemisorbed layer. In this way an initially mixed surface with a two and three dimer structural basis [22] reverts to a single phase with the lower As coverage. We similarly propose that the falling peak intensity but constant width of the reflection is due to the desorption of Sb dimer atoms in isolated regions, thereby maintaining the general c(4x4) symmetry of the reconstruction and the overall size of the domains.

We have already shown [1], (chapter 5), that the occupancy of the uppermost layer Sb dimers of the c(4x4) reconstruction is less than unity and therefore desorption of Sb atoms at higher temperatures merely leads to reduced occupancy of Sb atoms in the uppermost layer and a corresponding lower coverage. The half-width only significantly increases close to the transition temperature as the extent of desorption of the Sb atoms in the dimers is large enough to almost completely destroy the c(4x4) reconstruction. The phase transition measured by Etgens *et al* [21] was from an ordered As-rich c(4x4) surface to a similarly well ordered As-rich (2x4) surface. This was not, however, the case in our study as neither the group-V rich (2x4) nor the c(2x8) surface are present on InSb(001). However, the published phase diagram for InSb(001) [6], fig. 2.2, suggests that an Sb-rich A(1x3) surface should exist in place of the (2x4) surface phase.

The evolution of the 1/3 order diffraction peak, characteristic of the A(1x3) reconstruction, is shown in fig. 6.4. The peak is both weak in intensity and broad indicating that the resulting A(1x3) surface is poorly ordered. The 1/3 order peak does, however, exist at the same time as the stronger 1/2 order peak indicative of the formation of two separate surface phases. LEED and helium atom scattering measurements carried out by Mason *et al* [9] provided strong evidence that different surface domains coexist on the (001) surface of InSb. In particular, the A(1x3) and c(4x4) surfaces were clearly found to be present at the same time. They also report that there is no evidence of the A(1x3) structure gaining in intensity at the expense of the c(4x4) structure which is in contrast to our findings. In addition, Mason *et al* [9] propose that the A(1x3) appears at much lower temperatures (~ 280°C) than

indicated by the published phase diagrams. We do not find this to be the case with the onset of a 1/3 order peak only occurring at $T_s \sim 360°C$. Close inspection of their results shows, however, that the A(1x3) surface is more well formed on annealing to $T \sim 340°C$.

Well defined Sb-stabilised A(1x3) surfaces were produced by Liu and Santos [23] on annealing an InSb(001) substrate up to temperatures $T_s = T_t + 60°C$ in an antimony flux. Scanning electron microscopy (SEM) revealed the resulting surfaces were smooth and virtually featureless. Surfaces studied below this temperature, but above T_t, were found to be rough and characterised by large In droplets. On reaching $T_s = T_t + 60°C$ the condensed In droplets gain sufficient surface mobility to combine with the external Sb flux forming a smooth layer of InSb, the resulting surface periodicity being A(1x3).

In consequence, reciprocal space lattice scans were performed on our InSb(001) sample over both h and k axes from $T_t - 20°C$ up to $T_t + 90°C$, where irreversible In nucleation occurred. No sharp A(1x3) reconstruction was observed anywhere in this temperature range. A 1/3 order diffraction peak was only observed at $T_s \sim T_t + 5°C$. A possible reason for the lack of formation of a sharp A(1x3) reconstruction is that the incident Sb flux rate was not high enough to enable complete formation of an A(1x3) surface at the substrate temperatures used. It is, however, well documented that the A(1x3) reconstruction is a poorly ordered surface [3,5,7] and strong fractional order diffraction peaks would not be expected.

6.5 Summary.

The InSb(001)-c(4x4) surface reconstruction has been found to undergo a continuous thermal disordering transition with a critical transition temperature T_t, which varies as a function of an external antimony overpressure. The transition is found to be fully reversible under the applied Sb flux.

It is proposed that the phase transformation is brought about by random desorption of Sb dimer atoms in isolated regions and the overall c(4x4) surface symmetry is thus maintained until close to the transition temperature.

References.

[1]   N. Jones, C. Norris, C.L. Nicklin, P. Steadman, J.S.G. Taylor, C.F. McConville and A.D. Johnson, Surf. Sci. **398** (1998) 105.

[2]   P. John, T. Miller and T.C. Chiang, Phys. Rev. **B39** (1989) 1730.

[3]   C.F. McConville, T.S. Jones, F.M. Leibsle, S.M. Driver, T.C.Q. Noakes, M.O. Schweitzer and N.V. Richardson, Phys. Rev. **B50** (1994) 14965.

[4]   T.S. Jones, C.F. McConville, F.M. Leibsle and N.V. Richardson, Surface Review and Letters, Vol. 1, No. 4 (1994) 513.

[5]   R.G. Jones, N.K. Singh and C.F. McConville, Surf. Sci. **208** (1989) L34.

[6]   K. Oe, S. Ando and K. Sugiyama, Jap. J. Appl. Phys. **19** (1980) L417.

[7]   A. J. Noreika, M.H. Francombe and C.E.C. Wood, J. Appl. Phys. **52** (1981) 7416.

[8]   A.G. de Oliveira, S.D. Parker, R. Droopad and B.A. Joyce, Surf. Sci. **227** (1990) 150.

[9]   B.F. Mason, S. Laframboise and B.R. Williams, Surf. Sci. **258** (1991) 279.

[10]   J.D. Weeks, *Ordering in Strongly Fluctuating Condensed Matter Systems*, edited by T. Riste (Plenum, New York, 1980).

[11]   J.K. Kristensen and R.M.J. Cotterill, Phil. Mag. **36** (1977) 437.

[12]   E.G. McRae and R.A. Malic, Phys. Rev. Lett. **58** (1987) 1437.

[13]   A.D. Johnson, C. Norris, J.W.M. Frenken, H.S. Derbyshire, J.E. MacDonald, R.G. van Silfhout and J.F. van der Veen, Phys. Rev. **B44** (1991) 1134.

[14]   I.K. Robinson, A.A MacDowell, M.S. Altman, P.J. Estrup, K. Evans-Lutterodt, J.D. Brock and R.J. Birgeneau, Phys. Rev. Lett. **62** (1989) 1294.

[15]   G.A. Held, J.L. Jordan-Sweet and P.M. Horn, Phys. Rev. Lett. **59** (1987) 2075.

[16]   S.G.J. Mochrie, Phys. Rev. Lett. **59** (1987) 304.

[17]   A. Trayanov and E. Tosatti, Phys. Rev. Lett. **59** (1987) 2207.

[18]   P. Calverie, J. Massies, R. Pichaux, M. Sauvage-Simkin, J. Frouin, J. Bonnet
       and N. Jedrecy, Rev. Sci. Instrum. **60** (1989) 2369.

[19]   L. Onsager, Phys. Rev. **65** (1945) 117.

[20]   International Tables of Crystallography, Vol. A, Reidel Publ. Co., Boston
       (1983) 4th Rev. Ed. edited by Theo Hahn.

[21]   V.H. Etgens, M.Sauvage-Simkin, R. Pinchaux, J. Massies, N. Jedrecy,
       A. Waldhauer and N. Grieser, Surf. Sci. **320** (1994) 252.

[22]   M. Sauvage-Simkin, R. Pinchaux, J. Massies, P. Calverie, N. Jedrecy, J. Bonnet
       and I.K. Robinson, Phys. Rev. Lett. **62** (1989) 563.

[23]   W.K. Liu and M.B. Santos, 7th Intl. Conf. Narrow Gap Semiconductors,
       January 8-12, 1995, Santa Fe.

Chapter 7.

Atomic structure of the InSb(001)-c(8x2) reconstruction.

A surface X-ray diffraction study of the indium rich InSb(001)-c(8x2) reconstruction is reported, which gives for the first time a detailed picture of the atomic structure. A total of 96 in-plane (hk) reflections were used to determine the structure in the surface plane. The out-of-plane atomic positions were found by measuring along three crystal truncation rods (CTRs) where the total intensity distribution is the result of interference between bulk and surface contributions. The detailed analysis disproves the missing dimer model proposed from earlier PES and STM measurements. It shows that the reconstruction is deeper than the Sb-rich c(4x4) and is composed of chains of In atoms running along the [110] axis, separated by pairs of Sb dimers on top of the Sb-terminated bulk. The proposed structure is consistent with recent STM images and represents a significant departure from the models previously suggested for the c(8x2) reconstruction on any of the III-V (001) surfaces.

7.1. Introduction.

The (001) surface of III-V compound semiconductors exhibits many reconstructions characterised by large unit meshes. The appearance of a given reconstruction depends on the preparation conditions and, in particular, on the ratio of the group III and group V atoms at the surface. The structures have been the focus of much activity over the past two decades due to their complexity and the extensive use of the (001) surface for the epitaxial growth of III-V heterostructures for electronic applications. A detailed knowledge of the atomic structure is essential to understand the bonding and strain at the surface as well as the epitaxial growth process itself. Surface reconstructions will influence the assembly of arriving atoms and, in consequence, the morphology of the resulting interface.

Indium antimonide has attracted much interest because of its unusual electronic structure and potential application for high speed electronics and IR detectors. RHEED measurements [1,2] identified several surface reconstructions of the InSb(001) surface and established a phase diagram with substrate temperature and surface stoichiometry as parameters, fig. 2.2. In order of decreasing antimony concentration, the principal reconstructions are 1x1, c(4x4), A(1x3) and c(8x2). Of these the Sb-rich c(4x4) and the In-rich c(8x2) have been the most intensively studied. There is now a strong consensus that the c(4x4) reconstruction is composed of groups of antimony dimers aligned along the [110] bulk axis on top of an antimony terminated and largely undisturbed bulk structure, (chapter 5). By contrast, there remains considerable debate about the c(8x2) reconstruction.

Using high energy electron diffraction and core-level photoemission, John *et al* [3] proposed an arrangement of indium dimers in groups of three on top of an antimony terminated bulk. The model is shown in fig. 7.1(a). One dimer is missing from the basic 4x2 unit reducing the coverage of the surface to 3/4 of a monolayer (ML); the c(8x2) symmetry is achieved by displacement of adjacent dimer blocks along the [110] axis. This model, the so-called *missing dimer* model, was proposed to be consistent with atomic resolution STM measurements of Schweitzer *et al* [4] and McConville *et al* [5]. The filled state STM images of McConville *et al* are shown in fig.
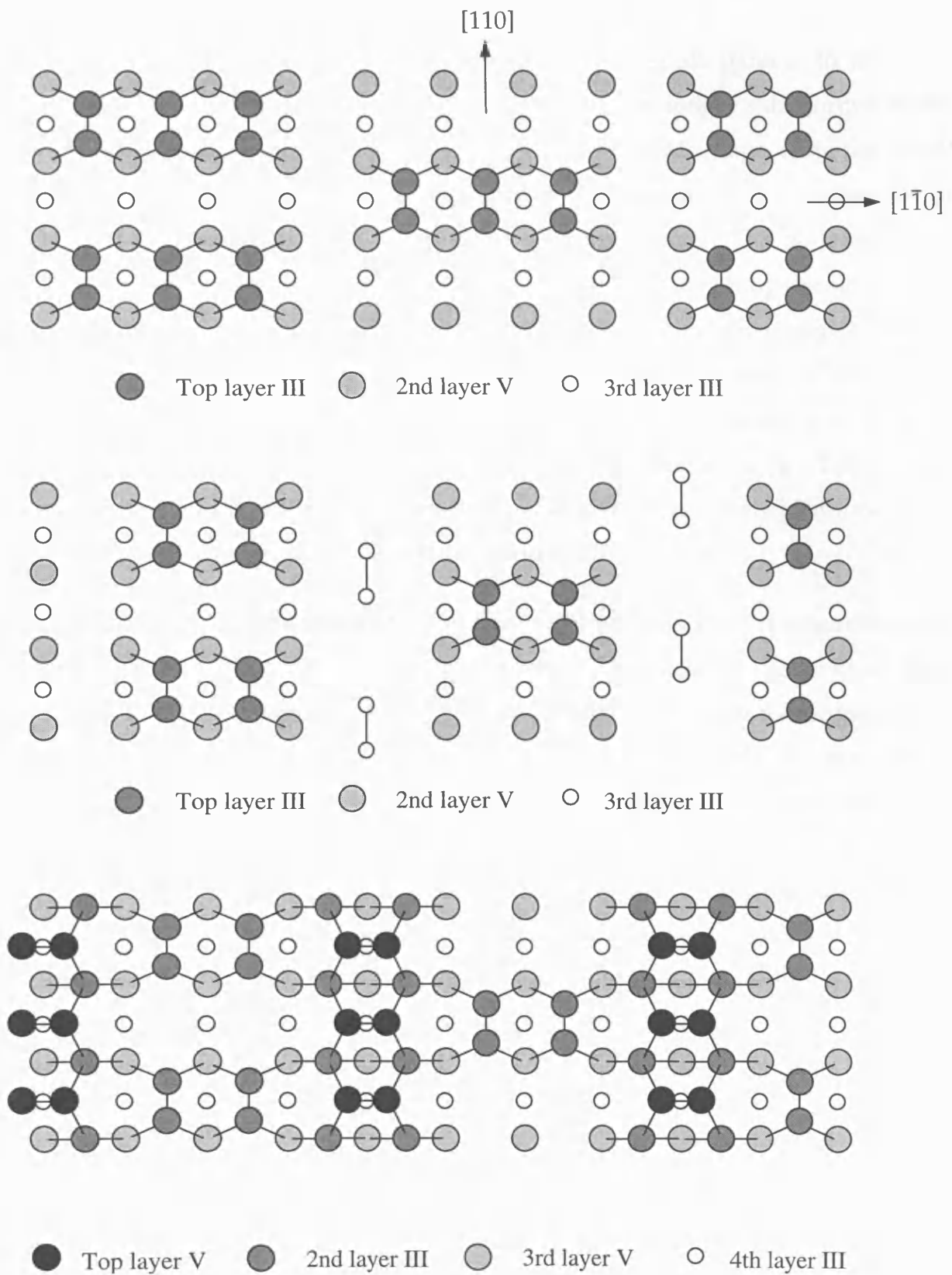
Fig. 7.1: *Possible models proposed for the c(8x2) reconstruction of the (001) surface of III-V semiconductors. The models are described in detail in the text.*

7.2 and reveal the presence of well ordered rows of spots parallel to the [110] direction with an apparent 4x1 unit cell aligned with the longer side normal to the rows. The seeming conflict of a 4x1 unit cell in the STM image with the c(8x2) symmetry of the diffraction pattern was resolved by associating the double row of spots with lone pair orbitals of Sb atoms in the second layer. This is, however, in contrast with the STM images of the InSb(001)-c(4x4) surface [14] by the same team, where the electrons associated with the uppermost layer atoms were imaged. A more recent STM study by Varekamp *et al* [6] has also questioned this interpretation of the c(8x2) reconstruction. High resolution images obtained with positive and negative biasing confirmed that the basic unit is indeed 4x2. In addition, single bright rows lying between, and running parallel to, the double rows were clearly identified. They were not attributed to a specific structural feature of the surface.

A c(8x2) reconstruction is found on other III-V (001) surfaces. Fig. 7.1 summarises the principal models proposed for this reconstruction. The basic arrangement of three group III dimers in the model of John *et al* for InSb(001) is the same as suggested by Frankel *et al* [7] for the c(8x2) structure on GaAs(001). It is the analogue of the arrangement proposed for the As-rich (2x4) and c(2x8) reconstructions on GaAs(001) by Chadi [8] and Pashley *et al* [9]. The model of Ohkouchi *et al* [10] for InP(001) is similar to that of John *et al* but has groups of two In dimers and two missing dimers and a corresponding lower coverage. The model shown in fig. 7.1(b) is that proposed by Biegelsen *et al* [11] for GaAs(001). The model is like that of Ohkouchi *et al*, but there are As vacancies in the second layer and Ga dimers in the third layer oriented along the [110] axis. The third model, fig. 7.1(c), was suggested by Skala *et al* [12] for GaAs(001). It is significantly different from the other two in that it proposes the top layer is composed of group V dimers separated by pairs of group III dimers in the second layer. Kendrick *et al* [13] described a similar model for InAs(001). It contains two In dimers in the third layer and one In dimer in the top layer. The dimerisation of the group V atoms seen in fig. 7.1(c) is removed by the inclusion of the group III dimer in the top layer. Like the Skala model, the c(8x2) symmetry is obtained by shifting the blocks of two group III dimers by one atom spacing along the [110] axis.
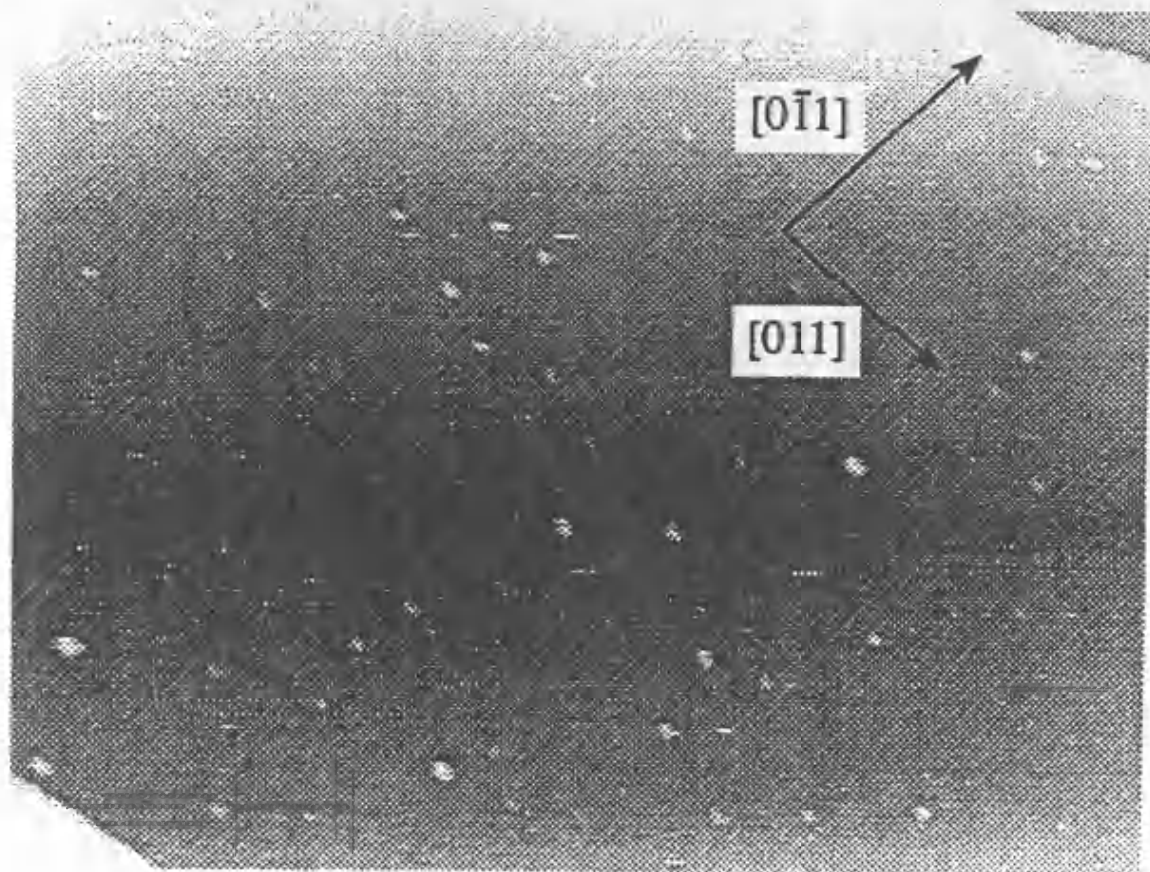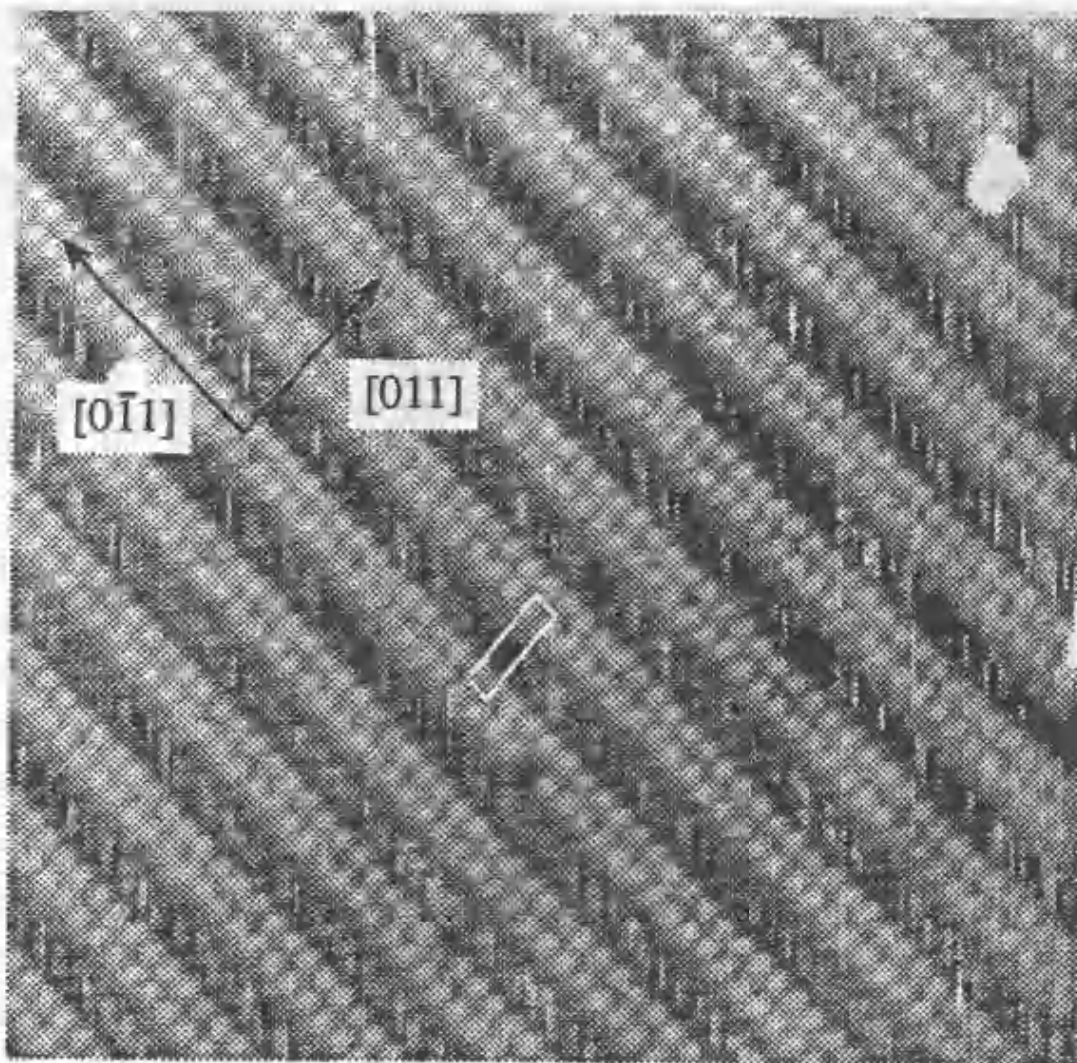
Many of the suggested structures have been derived from STM images which have limited resolution and sensitivity to deeper layers. Although there is not a universally accepted model of the c(8x2) reconstruction on the (001) surface of the III-V semiconductors, experience of the c(4x4) structure [3,14-17] would suggest that many of the features will be common. The structures shown in fig. 7.1 are therefore the obvious starting point for any new analysis of a c(8x2) reconstruction on a III-V (001) surface.

We report a surface X-ray diffraction (SXRD) study of the atomic structure of the InSb(001)-c(8x2) reconstruction. A large data set, including both in-plane and out-of-plane reflections, has been collected. It allows, for the first time, a detailed atomic picture of this important reconstruction to be produced None of the existing models of the c(8x2) reconstruction fully explain the data; the proposed model being closest to that of Skala *et al* [12]. The basic unit contains pairs of Sb dimers on top of an Sb terminated bulk with a local bonding similar to that found on the c(4x4) reconstruction and in bulk antimony [18]. The dimer pairs are separated by rows of In atoms with a nearest neighbour separation close to that of the bulk In structure.

7.2. Experimental.

The X-ray measurements were carried out on beamline 9.4 at the SRS, Daresbury, the details of which are described in section 5.2. The measurements of the c(8x2) reconstruction were taken immediately after those of the c(4x4) reconstruction, both studies being performed on the same InSb(001) sample.

The InSb(001) sample, with dimensions shown in fig. 4.2, was mounted in the LUXC environmental chamber; the base pressure in the chamber was ~ $1x10^{-10}$ mbar. The native oxide layer was removed with a single cycle of argon ion bombardment (800eV, $1\mu A/cm^2$, 45 min) and subsequent annealing (250°C, 20 min). The amorphous Sb cap was desorbed by heating at 300°C for 20 minutes under an Sb flux resulting in a good c(4x4) reconstruction, (chapter 5). Further argon ion bombardment (800eV, $1\mu Acm^{-2}$, 30 min) and annealing (380°C, 25 min), with the external Sb flux switched

off produced, on cooling to room temperature, a sharp c(8x2) LEED pattern. It is noted that the same sharp LEED pattern has also been obtained without the intermediate c(4x4) structure. Reciprocal space lattice scans along both the h and k axes are shown in fig. 7.3. The quarter-order peaks in 7.3(a) clearly indicate the formation of a c(8x2) reconstruction. A corresponding x2 periodicity is seen in fig. 7.3(b).

The X-ray angle of incidence was fixed at 1° for both in-plane and out-of-plane measurements. Fig. 7.4 shows a scan through the (5/4, 1, 0.2) reflection. It is fitted with a Lorentzian curve that has a full-width-half-maximum of 0.0657°, corresponding to a surface correlation length of ~ 900Å, approximately twenty-five (8x2) unit cells. A total of 96 in-plane reflections were measured to help determine the in-plane surface structure, of which 80 were fractional-order and 16 integer-order. Other reflections were too weak to be determined accurately. The space group of the c(8x2) reconstruction is c2mm and reflections were therefore measured over opposite quadrants of the hk plane in reciprocal space.

During data collection the (3/4, 1, 0.2) fractional-order reflection was regularly scanned in order to monitor any surface degradation. The peak intensity was found to decay by less than 5% over 120 hrs. This was slower than found for the c(4x4) surface [17], section 5.2, and implies the c(8x2) surface was more stable under UHV conditions.

7.3. Results.

7.3.1 Patterson function analysis.

The atomic structure of the surface unit cell is determined by direct comparison of the experimental structure factors, $|F_{hkl}|$, with the predictions of theoretical models. The first step in the structural analysis is to calculate the two-dimensional fractional-order Patterson function, given by equation (3.45). The in-plane structure factors $|F_{hk0}|$ are estimated by averaging the measured structure factor amplitudes at (h, k,
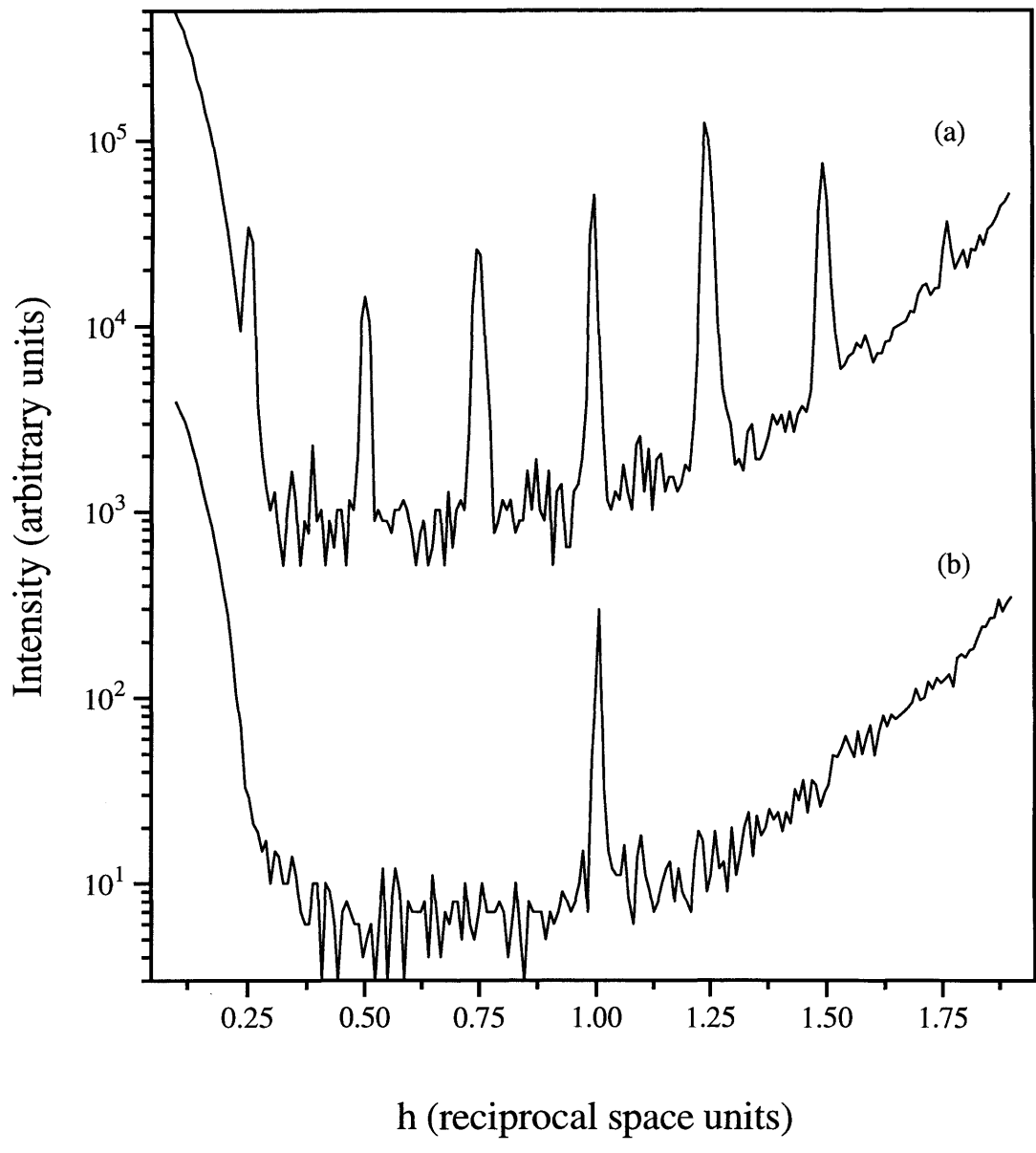
Fig. 7.3: *Reciprocal space lattice scans along: (a) the h axis and (b) the k axis. The curves clearly indicate the reconstruction is c(8x2).*
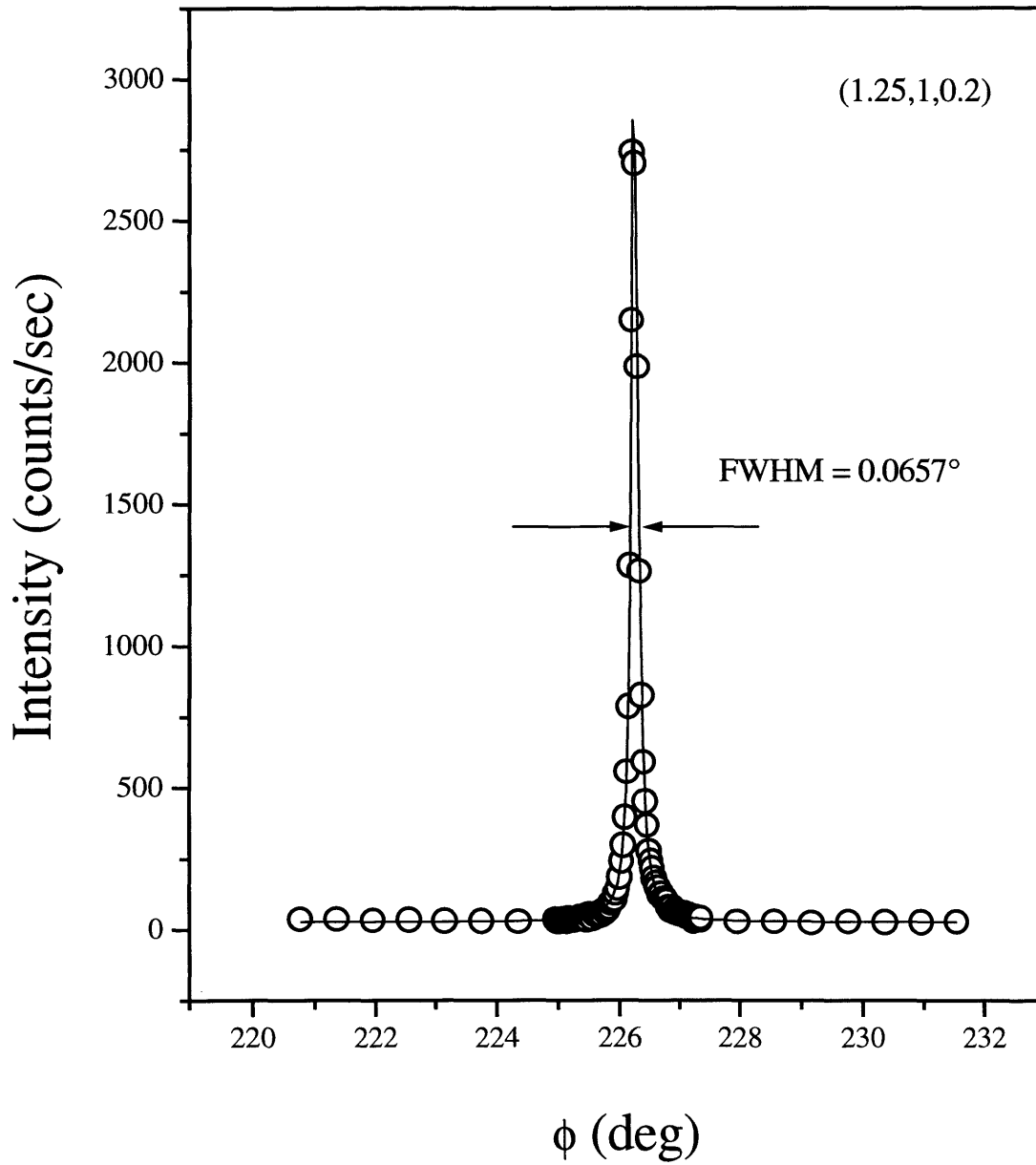
Fig. 7.4: *The (5/4, 1, 0.2) fractional-order-reflection. The fitted curve is Lorentzian.*

0.2) and (-h, -k, 0.2), the latter being equivalent to $|F_{hk\text{-}0.2}|$ by the Friedel rule. The 80 reflections reduce to 40 inequivalent reflections when averaged in this way.

The calculated Patterson map is shown in fig. 7.5. It is in good agreement with that derived by Smilgies *et al* in a preliminary report of another study of this surface [24]. The plot is more complex than the one obtained for the c(4x4) surface [17] indicating that the structure involves more than an ordered array of dimers. In addition to the self correlation peaks defined by the c(8x2) symmetry we can immediately identify a strong peak marked by the vector I. Since the Patterson function is derived from fractional order reflections we can associate the peak with a dominant interatomic correlation of the reconstruction, that is, to a displacement of one interatomic distance along the [110] axis. Inspection of the proposed models which involve dimers only, such as the missing dimer model, fig. 7.1(a), and the model of Ohkouchi *et al* [10], shows that they are inconsistent with this result. Fig. 7.6(a) shows the Patterson function calculated using theoretical structure factors derived from the three dimer model. 40 structure factor amplitudes were used to calculate the map, in order that the distortions due to the truncation of the data set were the same as for the experimental data. The resulting plot is far less complicated than the experimental one, fig. 7.5, with only two non-self correlation features present. The plot is, as expected, close to the experimental Patterson function deduced from the c(4x4) data, fig. 5.3, which is consistent with a dimer array. This result strongly suggests that the InSb(001)-c(8x2) reconstruction does not consist of a simple dimer arrangement.

The theoretical Patterson map, calculated using the model of Biegelsen *et al*, fig. 7.1(b), is displayed in fig. 7.6(b). Again the peaks associated with interatomic vectors between dimers are present. However, there is no peak corresponding to one interatomic distance along the [110] axis, which also brings this model into question. The third and final Patterson map in fig. 7.6, is the one associated with the model of Skala *et al* , fig. 7.1(c), and contains several new features. The Patterson is much closer to the experimental data than the other two, with many similar features present.
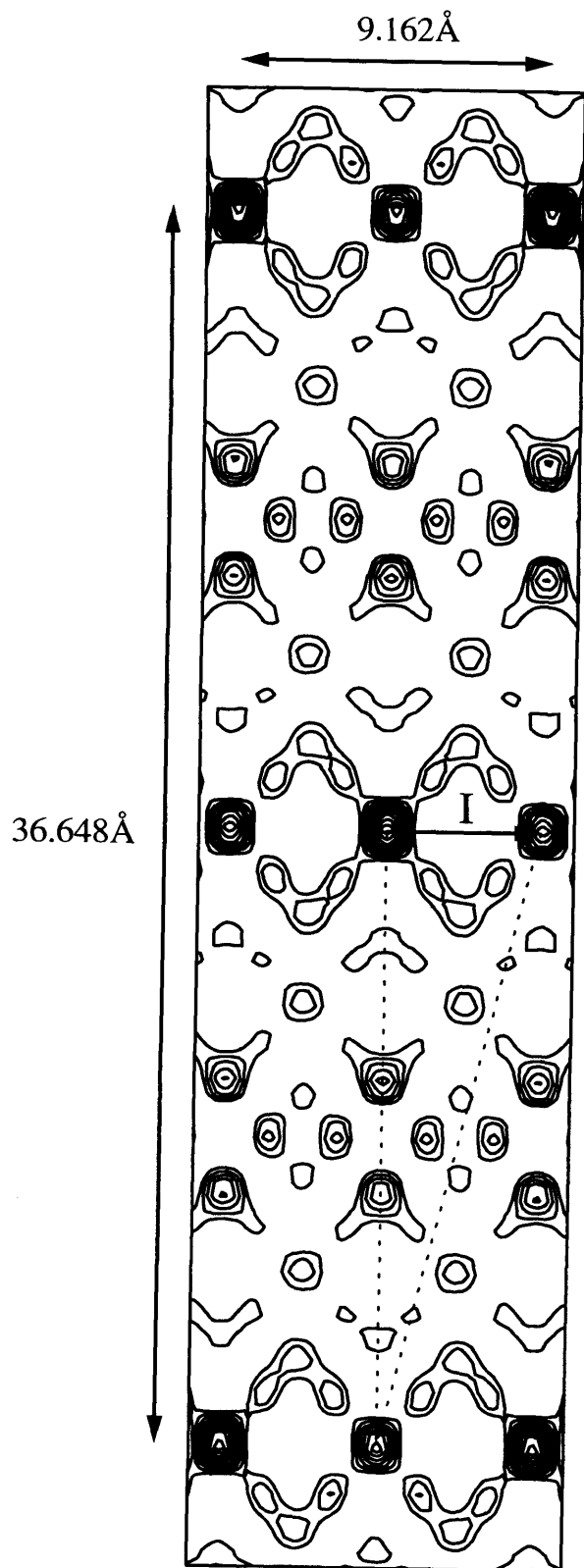
Fig 7.5: *Patterson map of the c(8x2) reconstructed surface. The plot has been rotated by 90°. Vector I identified the strong non-self correlation peak. The dotted lines indicate the irreducible part of the unit cell.*
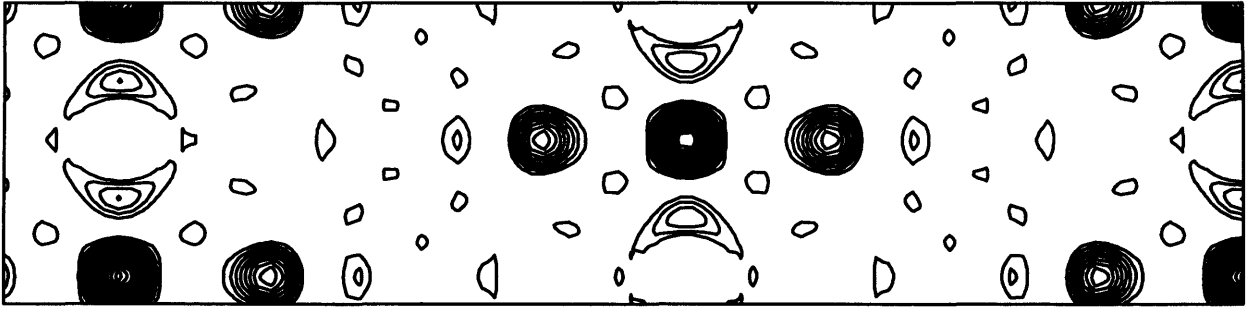
Fig. 7.6(a) : *Theoretical Patterson map of the three dimer model [3]*
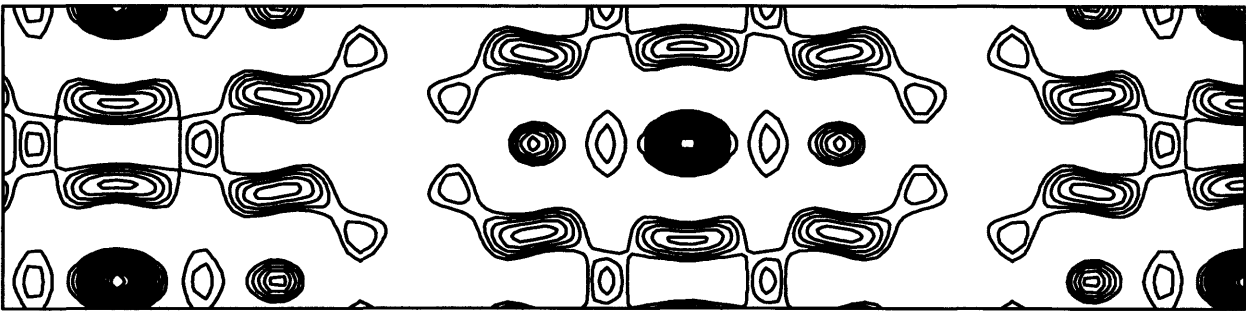
Fig. 7.6(b) : *Theoretical Patterson map of the model of Biegelsen et al [11]*
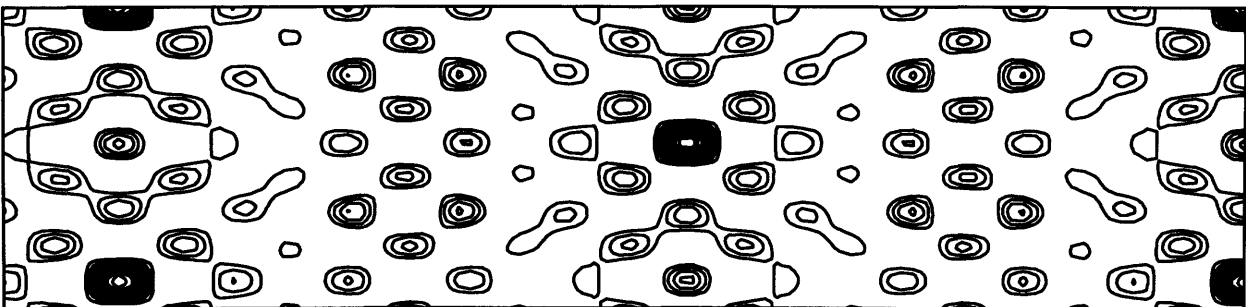
Fig. 7.6(a) : *Theoretical Patterson map of the model of Skala et al [12]*

7.3.2 Structure determination.

The validity of the models shown in Fig 7.1 was further tested by a comparison of the intensities at $\lambda = 0$ for the different models. In this we used the tetragonal nearest neighbour distance of 3.24Å [18] for the In-In dimer separation and the rhombohedral Sb nearest neighbour distance of 2.87Å [18] for the Sb-Sb dimer separation in model 7.1(c). The Debye-Waller factor was included and the best fit was found using only a scale factor as a variable. The models with three dimers in the 4x2 subunit, fig 7.1(a), and two dimers (Ohkouchi *et al*) gave χ^2 values of 31.1 and 35.6 respectively. Allowing the dimer atoms to relax along the [110] axis did not improve the agreement. Adding In dimers in the third layer, fig. 7.1(b), resulted in a χ^2 of 32.9, whereas the model of Skala *et al*, fig. 7.1(c), gave an initial χ^2 agreement of 22.7. Allowing the In dimer atoms to relax along the [110] axis and the Sb dimer atoms to relax along the orthogonal direction slightly improved the agreement with a χ^2 of 20.7. The model of Kendrick *et al* yielded a χ^2 agreement of 40.5 to the in-plane data.

The atomic coordinates perpendicular to the surface are determined from an analysis of the scattered intensity distribution as a function of λ along the crystal truncation rods (CTRs) normal to the surface plane. Three non-specular CTRs are shown in fig. 7.7. The three models in fig. 7.1 were fitted to the CTRs with the dimer lengths fixed at the best fit values calculated from the in-plane analysis and only a global scale factor was varied. χ^2 values of 25.0, 41.0 and 9.9 were obtained for the respective models in fig. 7.1. The model of Kendrick *et al* gave a χ^2 value of 21.5. Only the model of Skala *et al*, fig 7.1(c), gave a calculated rod profile resembling the experimental profile for the (1, 1, λ) rod.

This preliminary analysis indicates that the model of Skala *et al* is the best starting point from which to derive the structure of the reconstruction. We considered various modifications to the basic model of Skala *et al* and found that a significant improvement is the agreement was achieved if the Sb dimer was replaced by a single four-fold coordinated In atom at the mid-point of the dimer. The agreement was further improved by shifting the In atom and the four In atoms not involved in
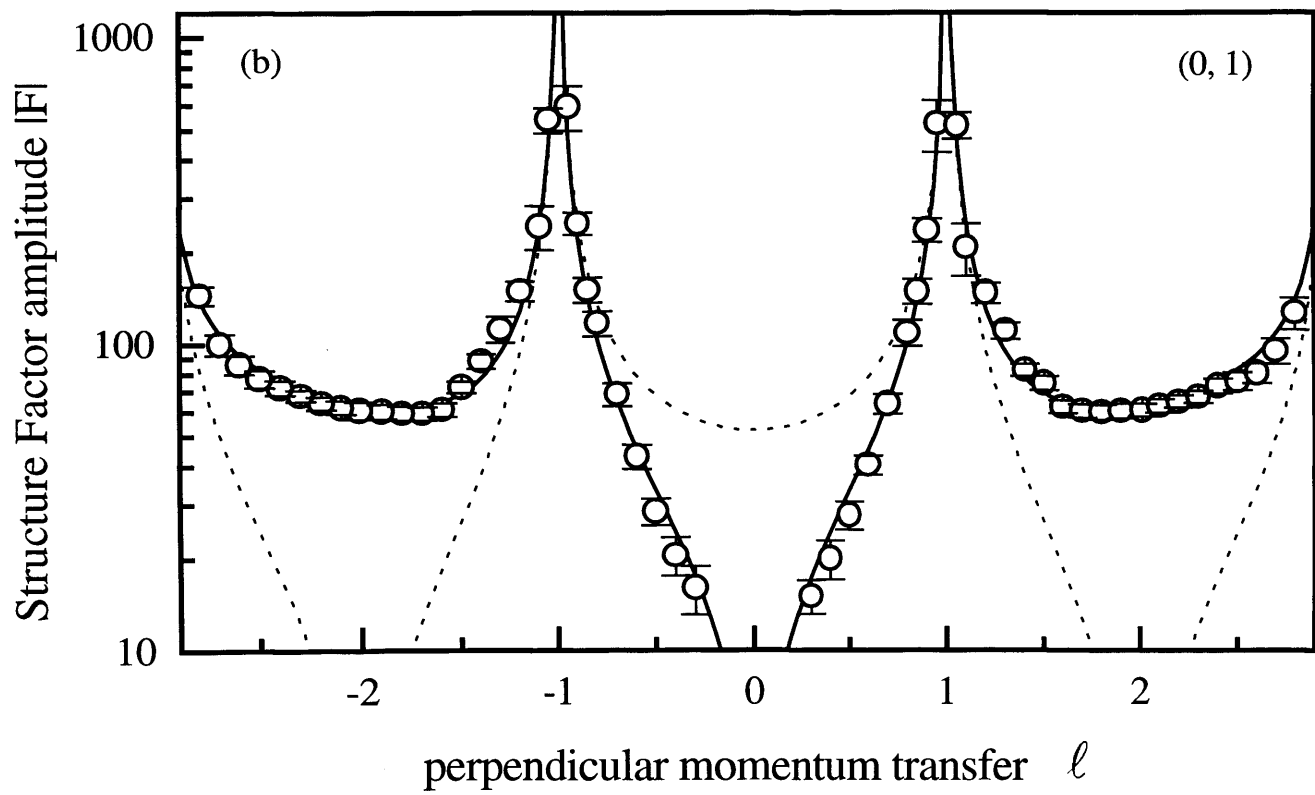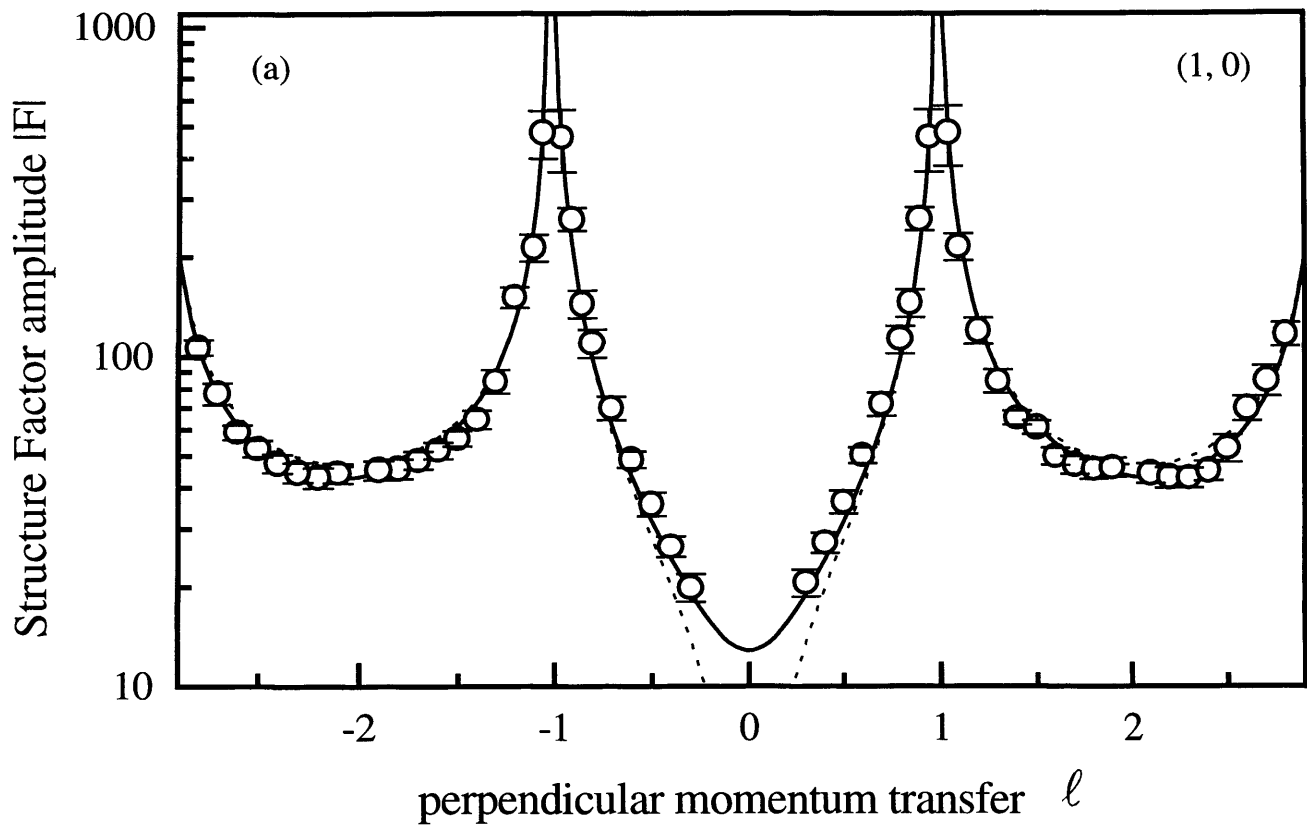
Fig 7.7(i): *Measured structure factor amplitudes along two CTRs. The solid line is the best fit to the data using the model in fig. 7.9. The dotted line is the structure factor amplitude calculated using only unreconstructed bulk InSb.*
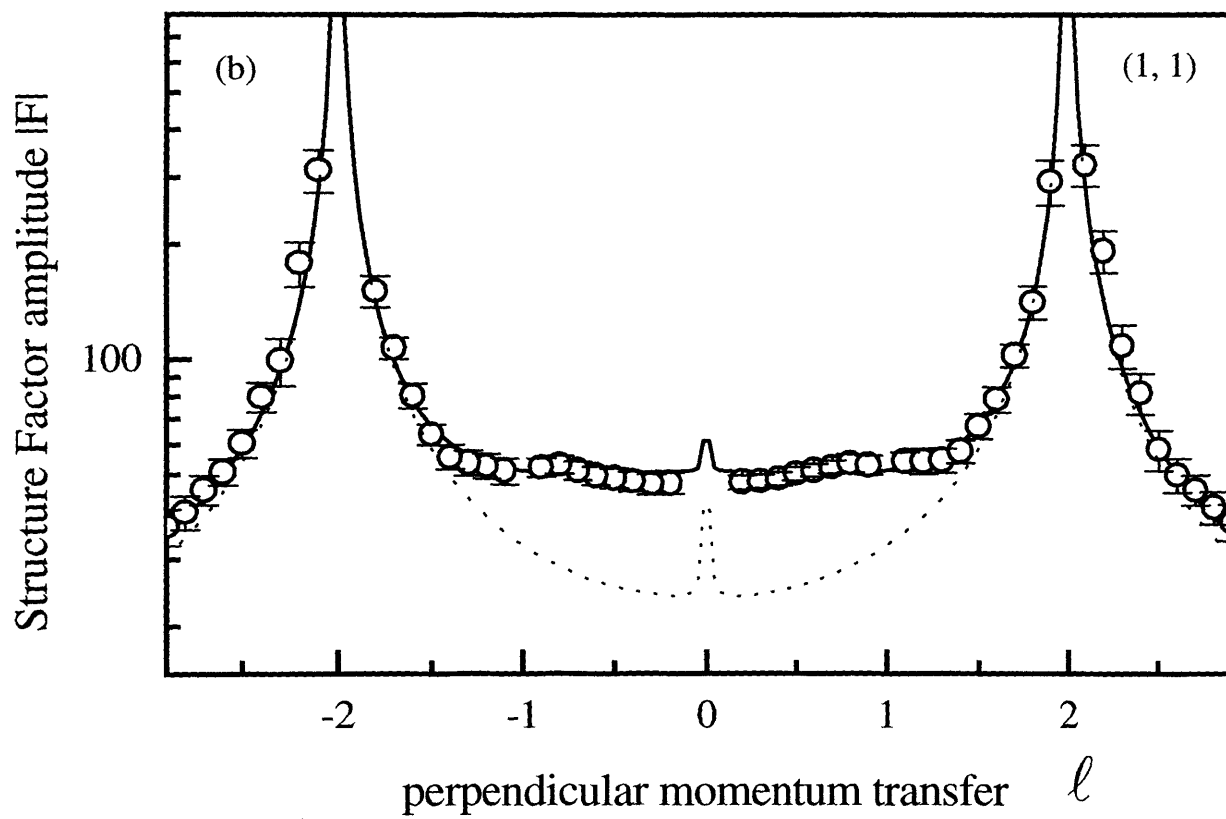
Fig. 7.7(ii): *Measured structure factor amplitudes along the (1,1,l) CTR.*

dimerisation in the second layer to which the top layer In atom is bonded, by half a lattice spacing, 2.29Å, in the [110] direction. This, in effect, forms a triple row of In atoms in two levels running between the dimer rows.

The final refinement was made by comparing the in-plane data at λ = 0.2 and the CTR profiles with this model. The variables used in the fit were the dimer length, the height of the dimers, the height of the undimerised In atoms in the top and second layer and the heights of the Sb atoms in the third layer. Separate scale factors were used for the in-plane and out-of-plane data. The number of top layer In atoms and second layer dimer atoms were also allowed to vary. They were found to be within 2% of complete occupancy. The best fit gave an agreement with the in-plane data of χ^2 =2.4 and with the out-of-plane data of χ^2 =1.1. Allowing other relaxations of the lattice, below layer 3, did not significantly improve the agreement. The experimental and calculated structure factors are listed in table 7.1; the calculated rod profiles are compared with the measured results in fig. 7.7. For completeness, a Patterson map was calculated using the theoretical structure factors derived from our model. All the main features of the experimental Patterson are successfully reproduced. A comparison of the experimental and theoretical Patterson functions is shown in fig 7.8.

7.4. Discussion.

The final model of the InSb(001)-c(8x2) reconstruction is shown in fig. 7.9 and the coordinates of the atoms are listed in table 7.2. X-ray diffraction does not allow us to differentiate between In and Sb atoms since their atomic numbers are close (49 and 51) and there are no convenient absorption edges to exploit. Our assignment of particular atoms to specific sites is based on considerations of the physical character of the surface and, in particular, on the evidence of the measured interatomic separations.

We first note that the length of the second layer dimers, 2e-2f, is measured to be 2.72±0.07Å. This is significantly below the value of 3.24Å which is the smallest

| h	k	$\left\|F_{hkl}^{expt}\right\|$	σ_{hkl}	$\left\|F_{hkl}^{calc}\right\|$
1/8	1/2	28.03	2.71	35.19
1/8	3/2	39.37	3.88	47.69
1/4	0	38.23	3.26	29.06
1/4	1	19.62	2.67	24.29
1/4	3	20.57	2.85	15.01
3/8	1/2	20.70	3.49	14.41
3/8	3/2	21.20	2.36	19.63
1/2	1	30.64	2.32	28.30
1/2	3	23.64	1.94	20.75
5/8	1/2	20.93	2.97	14.12
5/8	3/2	22.20	2.35	19.39
3/4	0	33.44	2.57	31.89
3/4	1	69.15	5.65	78.11
3/4	2	41.36	2.14	40.14
7/8	1/2	33.07	2.24	33.07
7/8	3/2	34.65	3.87	45.96
9/8	1/2	26.72	4.67	31.96
9/8	3/2	46.68	2.53	44.98
5/4	0	42.58	5.37	29.61
5/4	1	78.37	5.78	74.02
5/4	2	50.11	6.51	38.74
5/4	3	28.08	2.98	25.95
11/8	1/2	13.89	2.62	12.77
3/2	1	32.63	3.27	25.48
3/2	3	22.14	2.79	19.70
13/8	1/2	11.37	2.25	12.29
7/4	0	33.09	7.28	24.28
7/4	1	20.76	2.91	20.84
7/4	2	61.62	8.14	80.71
7/4	3	20.07	4.29	14.01
15/8	1/2	21.45	4.82	28.57
9/4	0	32.39	3.55	22.30
9/4	1	20.80	2.86	19.39
19/8	1/2	12.32	3.02	10.97
5/2	1	25.50	2.53	22.01
11/4	0	24.39	1.90	23.42
11/4	1	55.31	2.73	59.59
25/8	1/2	21.80	2.46	23.59
13/4	0	25.48	3.00	21.71
13/4	1	49.06	5.07	55.11

Tab. 7.1: *Experimental in-plane ($\lambda = 0.2$) fractional-order structure factors with associated errors. Calculated best fit values using the proposed model are also included.*
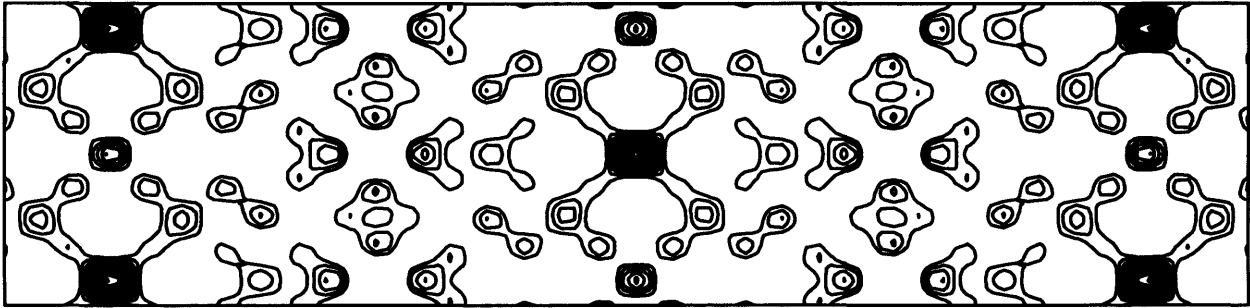
(a) Theoretical Patterson
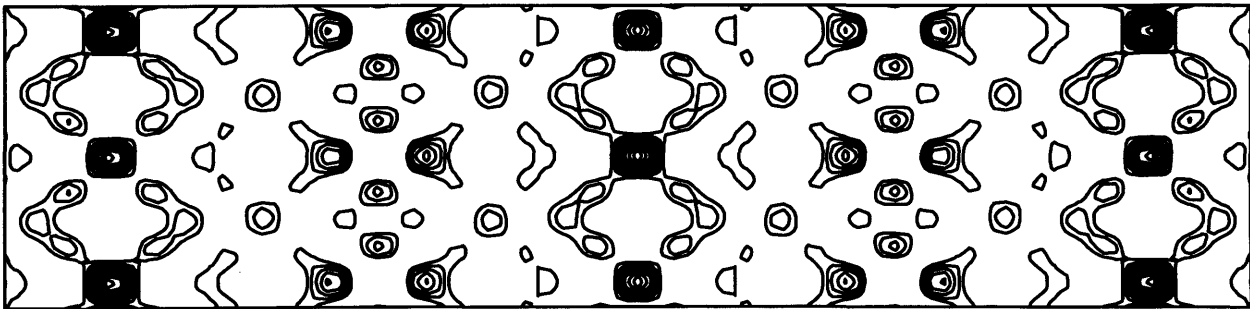
(a) Experimental Patterson

Fig. 7.8: *Theoretical and experimental Patterson functions for the InSb(001)*
c(8x2) reconstruction, calculated using forty structure factors at l = 0.
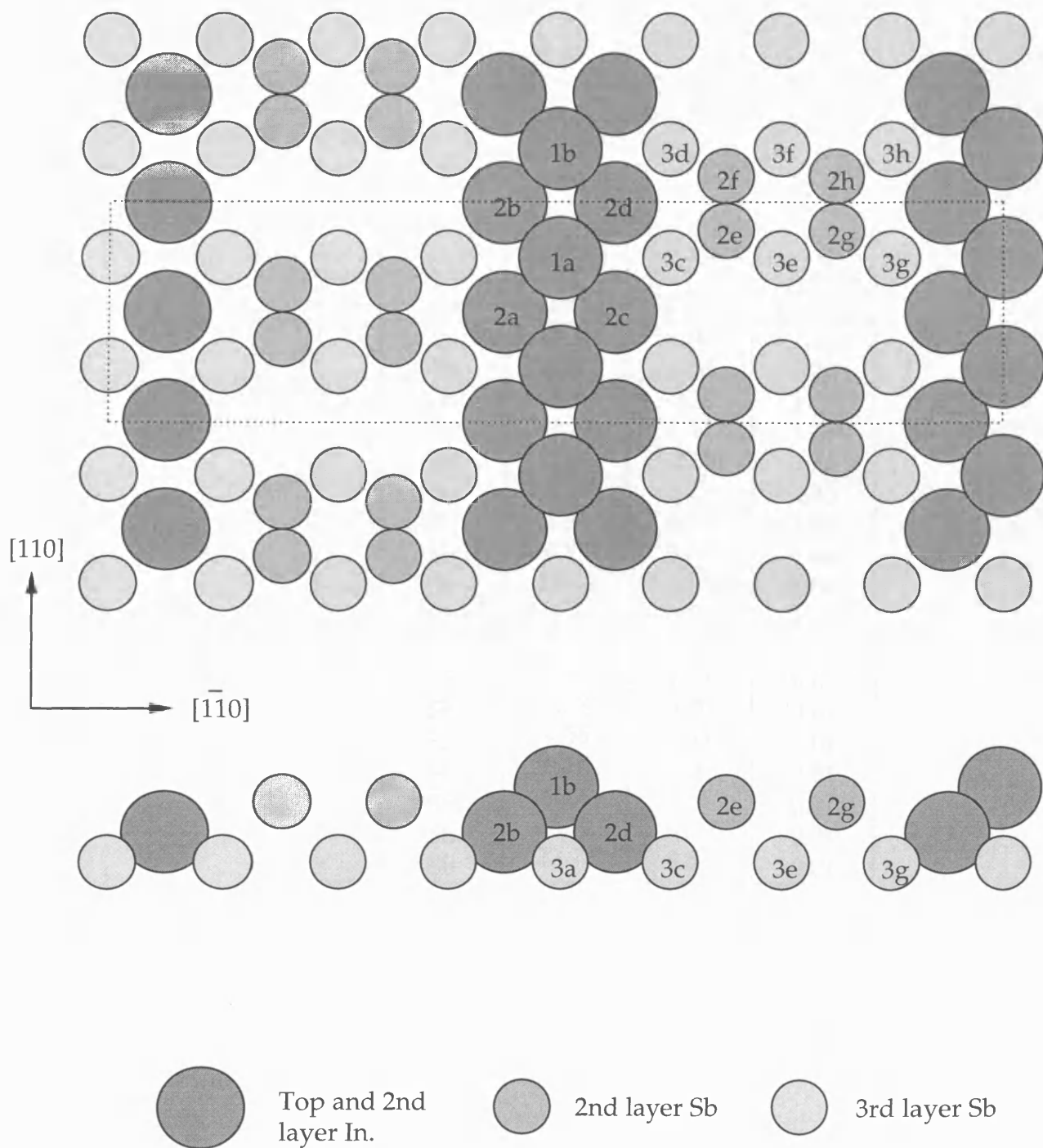
Fig. 7.9: *The proposed model for the InSb(001)-c(8x2) reconstruction. The broken line marks the c(8x2) unit cell.*

Layer n°	Atom type	x (±0.05Å)	y (±0.05Å)	z (±0.04Å)
1	In	0.00	0.00	2.23
1	In	0.00	4.58	2.23
2	In	-2.29	-2.29	1.23
2	In	-2.29	2.29	1.23
2	In	2.29	-2.29	1.23
2	In	2.29	2.29	1.23
2	Sb	6.87	0.93	1.68
2	Sb	6.87	3.65	1.68
2	Sb	11.45	0.93	1.68
2	Sb	11.45	3.65	1.68
3	Sb	0.00	0.00	0.01
3	Sb	0.00	4.58	0.01
3	Sb	4.58	0.00	0.01
3	Sb	4.58	4.58	0.01
3	Sb	9.16	0.00	0.01
3	Sb	9.16	4.58	0.01
3	Sb	13.74	0.00	0.01
3	Sb	13.74	4.58	0.01

Tab. 7.2: *The atomic coordinates (in Å) of the proposed model for the c(8x2) surface, Values shown in italics are fixed.*

separation of atoms in the body centred tetragonal phase of bulk In [18]. The difference is so great that we can confidently rule out the possibility of the dimer pairs being composed of In atoms as suggested in the model of John *et al* and, by analogy, the models of Biegelsen *et al*, Skala *et al* and Kendrick *et al*. The dimer length is infact much closer to the nearest neighbour distance of 2.87Å in the rhombohedral bulk phase of Sb. We therefore identify the atoms in the dimer pairs, 2e-h, as Sb.

The orientation of the dimers along the [110] axis is the same as found on the c(4x4) surface from which the In-rich c(8x2) surface was prepared. This confirms that the atoms in the layer below, layer 3, are also Sb, resulting in a similar local geometry to that found on the c(4x4) surface. Dimers formed on top of an In layer would be oriented along the orthogonal [1$\bar{1}$0] axis as is evident in fig. 7.1(c) which shows both group III and group V dimers. Each dimer Sb atom is therefore bonded to three other Sb atoms, the same local coordination as the rhombohedral bulk phase. The bond length to the Sb atoms in the layer below is 2.99±0.08Å, slightly higher than the bulk value. The angle of the dimer bond to the other bonds is 108±1°. which is close to the value of 109.47° expected for an ideal sp^3 arrangement. It is, therefore, suggested that three electrons form sp^3 orbitals and the remaining two form lone pairs.

We further observe that the arrangement of the atom 1a in the fourfold position above a square assembly of atoms in level 2 (2a-d) is almost identical to that found in the body centred tetragonal bulk indium structure. The separations of atoms 1a and 2a is measured to be 3.39±0.08Å. This agrees with the separation of the atom at the body centre and the atoms at the corners of the square base of the bulk tetragonal unit cell, 3.370Å. We therefore identify atoms 1a, 1b and 2a-d as indium.

The proposed arrangement, shown in fig. 7.9, is consistent with the photoemission measurements of John *et al* who suggested the In coverage was between 0.61 and 0.79 ML. Our model indicates that there is 3/4 ML of In, but also 1/2 ML of Sb which was not proposed in the above study. It also agrees with the STM images of Schweitzer *et al* [4] and, in particular, with the more recent STM images reported by Varekamp *et al* [6]. In the latter study a distinct row of bright spots can be seen running along the [110] axis, parallel to and in-between double rows of double spots. STM is sensitive

to the uppermost atomic layer and from fig. 7.9 this would mean In atoms 1a and 1b and the Sb atoms 2e-h which make up the dimer pairs. We therefore suggest the clearly defined double rows correspond to the lone pair orbitals of the Sb dimers in the second layer and the less well defined streaky features in the single row to the In atoms 1a, 1b and their equivalents.

The local arrangement of Sb dimers is similar to that generally agreed to occur on the Sb rich c(4x4) structure except that there are blocks of two Sb dimers for the c(8x2) structure rather than blocks of three [14,17]. It would suggest that the Sb dimer attached to a lower Sb layer, with a local coordination similar to that of the bulk, is a particularly stable unit. We find here the occupancy of the dimers to be complete, whereas there were vacancies in the c(4x4) structure almost certainly due to preparation conditions. The more significant difference with the Sb rich surface is the presence of extended chains of In. The indium chains closely resemble the bulk tetragonal structure. This suggests the bonding is metallic and the In chains form a one dimensional conducting path on the surface. The model is also believed to be consistent with electron counting heuristics. The local bonding of the dimers is as for the c(4x4) reconstruction with each Sb dimer atom having three bonding electrons and an occupied lone pair orbital. The electrons associated with the In chains are involved in metallic bonding.

The greater departure from the ideal bulk-terminated structure that the chains represent is one reason why the c(8x2) surface, although it is easy to produce and well ordered, is not used as a starting point for the growth of epitaxial InSb films. The more developed reconstruction will impede the growth mechanism and lead to a disrupted epilayer.

The model we propose in fig. 7.9 is a significant departure from other models suggested for the c(8x2) reconstruction on the (001) surface of InSb or any other III-V semiconductor. All the earlier studies suggest that the pairs of dimers are composed of group III atoms contrary to the conclusions of this study. The models of Skala *et al* and Kendrick *et al* do contain chains separating the dimers but the arrangement within the chains is different. Our model is noticeably flatter than that of Kendrick *et*

al. The similarity of the III-V semiconductors would suggest that our model should also apply to other surfaces.

7.5. Summary.

The structure of the InSb(001)-c(8x2) reconstruction has been determined using SXRD. The reconstruction extends into the second surface layer and is characterised by chains of indium atoms running along the [110] axis separated by pairs of Sb dimers on top of an Sb-terminated bulk. Both features, that is, the blocks of second layer Sb dimers and the In chains are departures from any previously proposed models of c(8x2) structures on the III-V (001) surfaces. The model is, however, consistent with earlier STM and photoemission data.

References.

[1]   K. Oe, S. Ando and K. Sugiyama, Jap. J. Appl. Phys. **19** (1980) L417.

[2]   A.J. Noreika, M.H. Francombe and C.E.C. Wood, J. Appl. Phys. **52** (1981) 7416.

[3]   P. John, T. Miller and T.C. Chiang, Phys. Rev. B**39** (1989) 1730.

[4]   M. O. Schweitzer, F.M. Leibsle, T.S. Jones, C.F. McConville and N.V. Richardson, Surf. Sci. **280** (1993) 63.

[5]   C.F. McConville, T.S. Jones, F. M. Leibsle, S.M. Driver, T.C.Q. Noakes, M.O. Schweitzer and N.V. Richardson, Phys. Rev. B**50** (1994) 14965.

[6]   P.R. Varekamp, M. Bjorkvist, M. Gothelid and U.O. Karlsson, Surf. Sci. **350** (1996) L221.

[7]   D.J. Frankel, C. Yu, J.P. Harbison and H.H. Farrell, J. Vac. Sci. Technol. B **5** (4) (1987) 1113.

[8]   D.J. Chadi, J. Vac. Sci. Technol. A **5** (4) (1987) 834.

[9]   M.D. Pashley, K.W. Haberern, W. Friday, J.M. Woodall and P.D. Kirchner, Phys. Rev. Lett. **60** (1988) 2176.

[10] S. Ohkouchi and I. Tanaka, Appl. Phys. Lett. **59** (13) (1990) 1588.

[11] D.K. Biegelsen, R.D. Bringans, J.E. Northrup and L.-E. Swartz, Phys. Rev. **B27** (1983) 4966.

[12] S.L. Skala, J.S. Hubacek, J.R. Tucker, J.W. Lyding, S.T. Chou and K.Y. Cheng, Phys. Rev. **B48** (1993) 9138.

[13] C. Kendrick, G. LeLay and A. Kahn, Phys. Rev. **B54** (1996) 17877.

[14] C.F. McConville, T.S. Jones, F.M. Leibsle and N.V. Richardson, Surf. Sci. **303** (1994) L373.

[15] M. Sauvage-Simkin, R. Pinchaux, J. Massies, P. Calverie, N. Jedrecy, J. Bonnet and I.K. Robinson, Phys. Rev. Lett. **62** (1989) 563.

[16] P.M. Thibado, B.R. Bennett, B.V. Shannabrook and L.J. Whitman, J. Crystal Growth, Vol. 175, No. Pt1 (1997) 317.

[17] N. Jones, C. Norris, C.L. Nicklin, P. Steadman, J.S.G. Taylor, C.F. McConville and A.D. Johnson, , Surf. Sci. **398** (1997) 105.

[18] R.W.G. Wyckoff, Crystal Structures, Interscience Publishers, New York, 2nd Ed. 1969.

[19] S.D. Evans, L.L. Cao, R.G. Egdell, R. Droopad, S.D. Parker and R.A. Stradling, Surf. Sci. **226** (1990) 169.

[20] J.S.G. Taylor, C. Norris, E. Vlieg, M. Lohmeier and T.S. Turner, Rev. Sci. Instrum. 67 (7) (1996) 2658.

[21] I.K. Robinson, *Handbook on Synchrotron Radiation*, volume III, North-Holland, Amsterdam, 1989.

[22] B.E. Warren, *X-ray Diffraction*, Addison-Wesley, Reading, 1969.

[23] International Tables of Crystallography, Vol. A, 4th Rev. Ed. Reidel Publ. Co., Boston (1983) edited by Theo Hahn.

[24] D.-M. Smilgies, E. Landemark, R. Fiedenhans'l, M. Nielsen, L. Seehofer, G. Falkenberg, L. Lottermoser, R.L. Johnson, A.A. Davis and R.G. Jones, Hasylab Annual Report, 1994.

Chapter 8.

Oxide removal from InSb(001) substrates.

A study of the removal of the native oxide from InSb(001) substrates using X-ray diffraction and Auger electron spectroscopy is reported. Several methods have been investigated to produce atomically flat, oxide free, surfaces. These include thermal annealing, argon ion bombardment at both room temperature and elevated temperature, and irradiation of the surface with atomic hydrogen. The quality of the resulting c(8x2) surface gives a good measure of the relative success of each technique. The reflected X-ray intensity was measured as a function of perpendicular momentum transfer λ along the specular (00λ) rod and gives a clear indication of the roughness of each surface. The lateral order was determined from the width of the in-plane fractional order reflections.

The results show a marked improvement in surface order when using hydrogen irradiation/annealing as opposed to thermal annealing alone. A more significant improvement in surface quality, however, was noted when sputtering at elevated temperature.

8.1 Introduction.

The preparation of smooth chemically clean semiconductor surfaces prior to epitaxial growth is an essential prerequisite in the manufacture of modern electronic devices. The removal of the passivating native oxide layer by thermal desorption has proved to be successful in the preparation of both Si and GaAs substrates [1]. In contrast, the removal of the native oxide of InSb(001) by thermal desorption has proved difficult; the technique being both time consuming and resulting in the formation of rough surfaces [2]. The reason for this is that the oxide desorption temperature lies well above the non-congruent evaporation temperature for InSb (~325°C). A further difficulty is the low melting point of InSb, (525°C). However, successful thermal desorption of the oxide layer of InSb has been reported [3]. Liu *et al* showed, using RHEED, AES and X-ray photoelectron spectroscopy (XPS) measurements that the surface oxide was progressively removed by heating the substrate under an antimony flux. They proposed the desorption was a multistage process with Sb oxides being reduced first. The In oxides then desorbed as the substrate temperature was raised further in the presence of the Sb flux; the flux being necessary to react with resulting In droplets and hence form smooth layers of InSb on the surface.

In consequence of the relative lack of success of thermal desorption, low energy argon ion bombardment and subsequent annealing has been the preferred technique for the removal of the oxide layer. This method is highly effective in the removal of contaminants, however it has several disadvantages as the group V species is preferentially depleted resulting in the formation of large In droplets. This can lead to surface roughness and also electronic damage well below the penetration depth of the incident argon ions [4].

More recently, hydrogen irradiation has been used to remove the native oxide layer from III-V semiconductor surfaces [5,6,7]. Schaeffer *et al* [5] studied the effect of atomic hydrogen on GaAs(001) substrates using XPS measurements. They obtained spectra for both the As $2p_{3/2}$ and Ga $2p_{3/2}$ core-level intensities which showed clear decomposition and eventual desorption of both Ga and As oxides. The corresponding XPS results for the 1s-lines of carbon and oxygen show that the carbon

signal is below the detection limit, but a weak O signal persists. However, they report that the C and O contamination levels fall from an initial value of approximately four monolayers to less than 1/20 of a monolayer. After hydrogen irradiation a clear LEED pattern was also observed.

A later study by Sugaya *et al* [6], using RHEED and AES measurements, also investigated the effects of atomic hydrogen on the oxidised GaAs(001) surface. They reported that a previously rough surface gave a clear (2x4) RHEED pattern after hydrogen irradiation. The corresponding AES spectra also provided direct evidence of the removal of carbon and oxygen.

Oxide free, clean III-V surfaces have also been produced using an electron cyclotron resonance (ECR) hydrogen plasma [8,9,10,11]. It was first demonstrated by Sugata *et al* [8] that a hydrogen radical beam produced by an ECR plasma could be used to remove carbon and oxygen from GaAs substrates. The oxide layer was not completely removed, however the Auger oxygen peak fell to one tenth of its initial value after exposure to the hydrogen radical beam. Similar later work, performed on InSb(001) by Johnson *et al* [9], showed ECR hydrogen plasma cleaning to be more effective than the other commonly used surface preparation techniques. Unlike similar surfaces prepared by thermal annealing or argon ion bombardment which were characterised by a high density of indium droplets, scanning electron microscopy (SEM) images of the ECR plasma cleaned surfaces showed that they were very flat with no visible surface topography.

In this chapter, we report an SXRD study of the removal of the native oxide layer from InSb(001) substrates using a number of the techniques highlighted above. SXRD has previously been successfully used to provide accurate information on the morphology and roughness of clean semiconductor surfaces [12].

8.2 Experimental.

8.2.1 Measurements.

The X-ray measurements reported in this chapter were made on beamline 9.4 (section 4.4.2) at the SRS, Daresbury. The wavelength used was 0.9Å and the angular acceptance of the detector was 0.82° in-plane and 0.25° out-of-plane. The base pressure in the chamber was ~ 2×10^{-10} mbar. The InSb samples used were uncapped and prepared as described in section 4.3.1.

The atomic structure of the InSb(001) surface is described by a tetragonal unit cell defined by three base vectors a_i :

$$\mathbf{a}_1 = \frac{1}{2}\left[1\,\overline{1}\,0\right]_{cubic} \qquad \mathbf{a}_2 = \frac{1}{2}[110]_{cubic} \qquad \mathbf{a}_3 = [001]_{cubic}. \qquad (8.1)$$

Reciprocal space coordinates are given in units of { $\mathbf{b}_i$ } with $\mathbf{a}_i.\mathbf{b}_j = 2\pi\delta_{ij}$. The in-plane reflections were measured with the Miller index normal to the surface $\lambda = 0.2$ and the angle of incidence $\beta_{in} = 1°$. For each reflection the diffracted intensity was measured as described in section 5.2. For the out-of-plane reflectivity scans along the specular (00λ) rod, the intensity was measured by counting scattered photons within the angular acceptance of the detector while symmetrically increasing the angle of incidence β_{in} and keeping the exit angle $\beta_{out} = \beta_{in}$. Integrated intensities were obtained by numerically integrating the peaks after linear background subtraction. The correction factors, described in section 4.5.4, were applied to obtain the structure factors.

Four InSb(001) samples were treated separately using two cycles of each particular cleaning technique. The load-lock sample transfer system was used to exchange samples between the different techniques. As all cleaning methods were performed in the absence of an Sb overpressure, the In-rich c(8x2) reconstruction was expected.

The first method used was thermal annealing alone. The sample was held at 370°C for 45 mins. Auger electron spectroscopy showed that carbon and oxygen remained at the surface after both cycles. The second method used was argon ion bombardment and annealing (800V Ar^+ ions for 45 mins at $1\mu A/cm^2$; anneal 30 mins at 370°C). In this case, AES showed that C and O Auger peaks could no longer be observed after the treatment, fig. 8.1(a). After argon ion bombardment with the sample held at an elevated temperature (800V Ar^+ ions, T = 370°C for 30 mins), the AES spectrum, fig. 8.1(b), again showed the absence of both C and O. The final method employed was hydrogen irradiation using a similar procedure to that used by Sugaya et al [6]. Atomic hydrogen was produced in a cracking cell, which was purpose built in Leicester for the experiment and is described in detail below. The distance between the end of the cracking cell and the sample was approximately 20cm which was small enough to eliminate any significant recombination of the hydrogen ions. The base pressure before cleaning was ~ $2x10^{-10}$ mbar; during cleaning the hydrogen gas pressure was held at $5x10^{-5}$ mbar. The sample was held at 370°C during each 30 minute irradiation. The AES spectra in fig. 8.2 clearly show the removal of the O peak. Fig. 8.2(a) is the AES spectrum after one treatment. The size of the O peak is already less than that of the O peak after both cycles of thermal annealing alone. The spectrum after the second treatment is shown in fig. 8.2(b). It can be seen that complete oxygen removal has been achieved.

8.2.2   Hydrogen cracking cell.

The hydrogen cracking cell used in the experiment described here is shown schematically in fig. 8.3. The cell essentially consists of a coiled tungsten filament housed inside an alumina tube, with an internal diameter of 5 mm. The alumina tube has two purposes; it collimates the hydrogen beam and it also prevents any significant deformation of the tungsten filament.

Research grade hydrogen, (99.999% purity), is leaked into the cell through an external valve and passes through the alumina tube, via a hollow stainless steel support rod, where it is cracked by the hot tungsten filament. The filament is heated
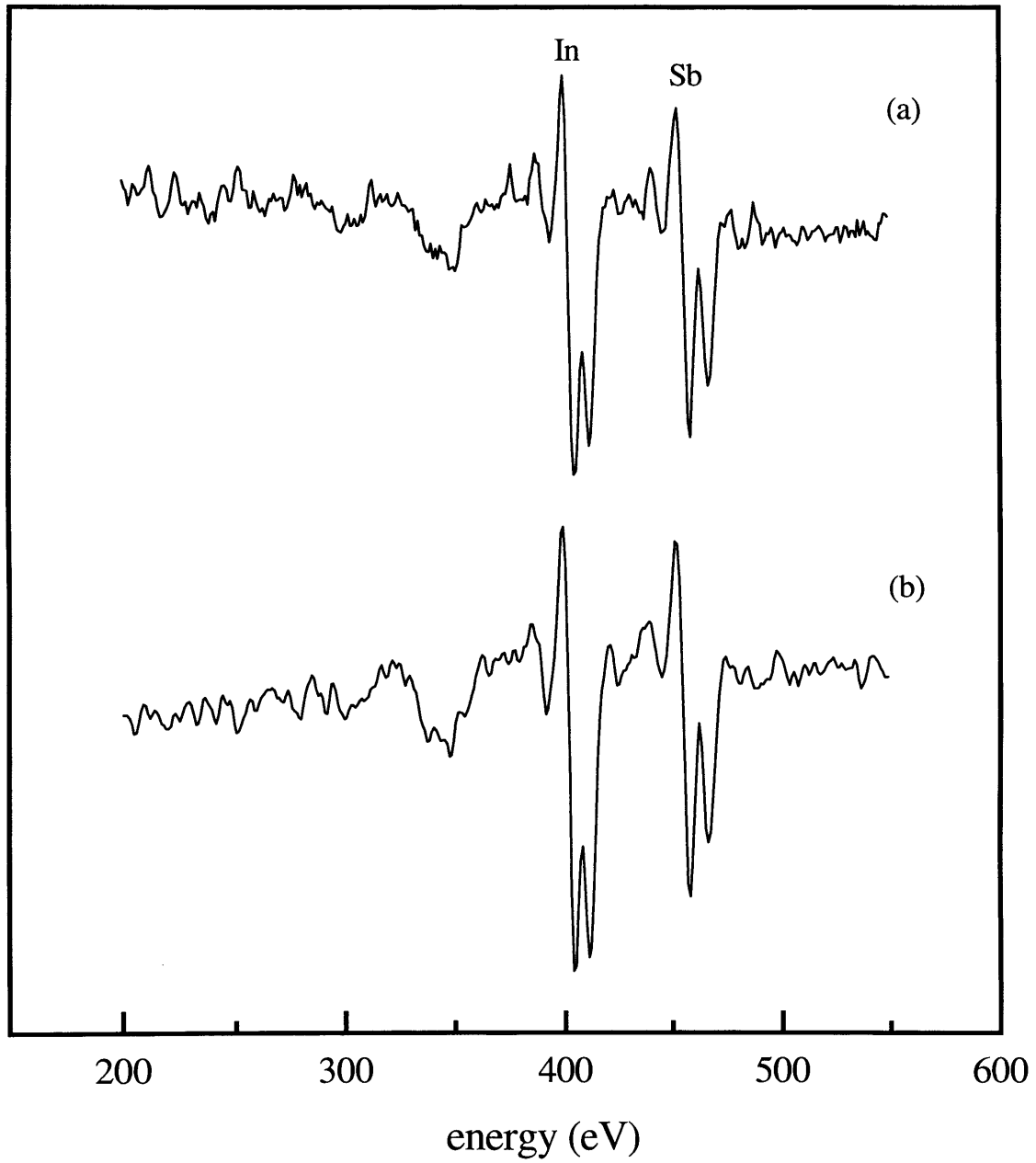
Fig. 8.1: *Auger spectra of the InSb(001) surface after argon ion bombardment (a) at room temperature, (b) at 370°C. The relative sizes of the In and Sb peaks indicate preferential depletion of the Sb.*
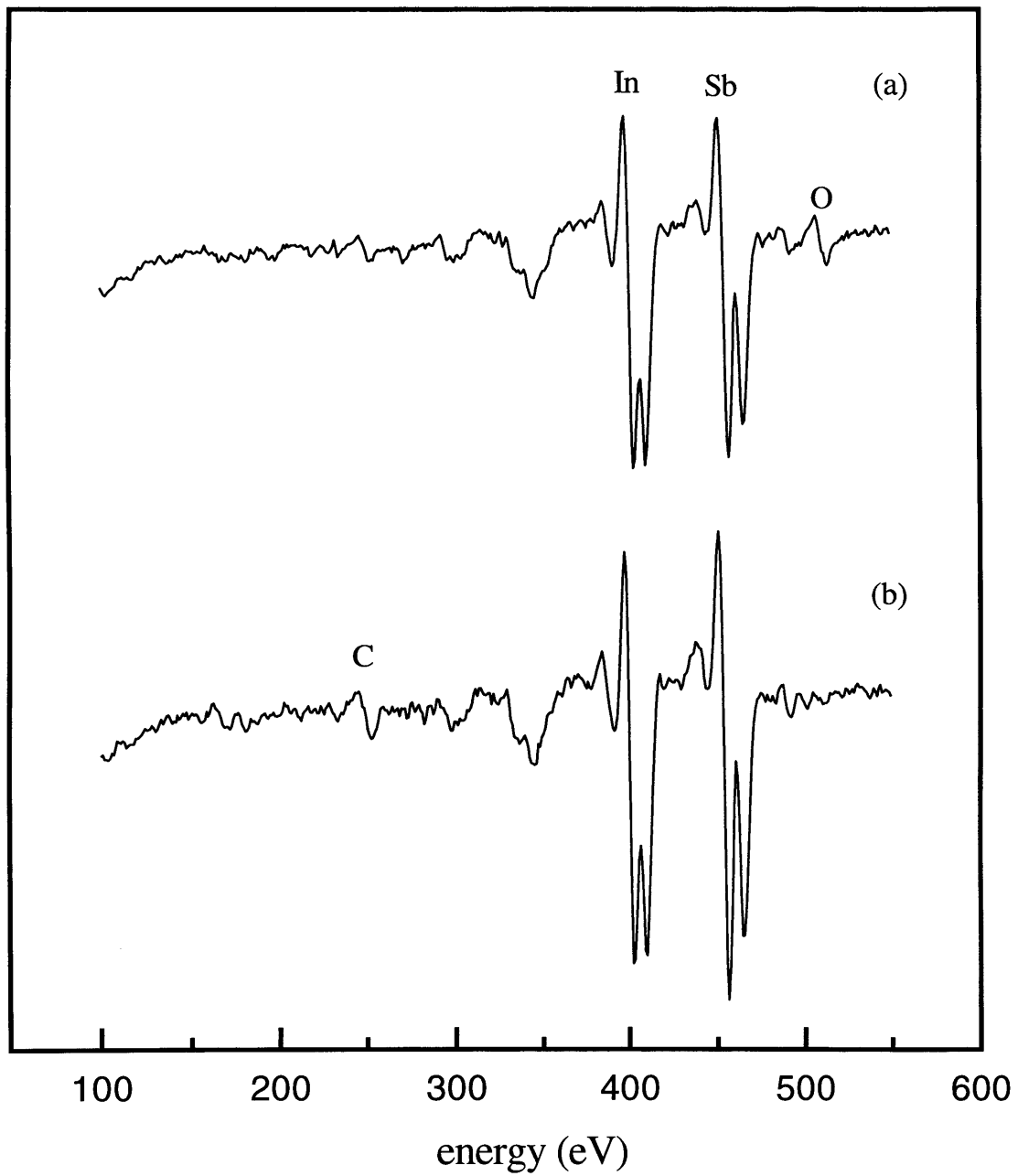
Fig. 8.2: *Auger spectra of the InSb(001) surface treated with hydrogen,*
(a) after 30 mins irradiation at 370°C, (b) after 60 mins irradiation at 370°C
The disappearance of the O peak below the detectable limit is evident
after 60 mins.
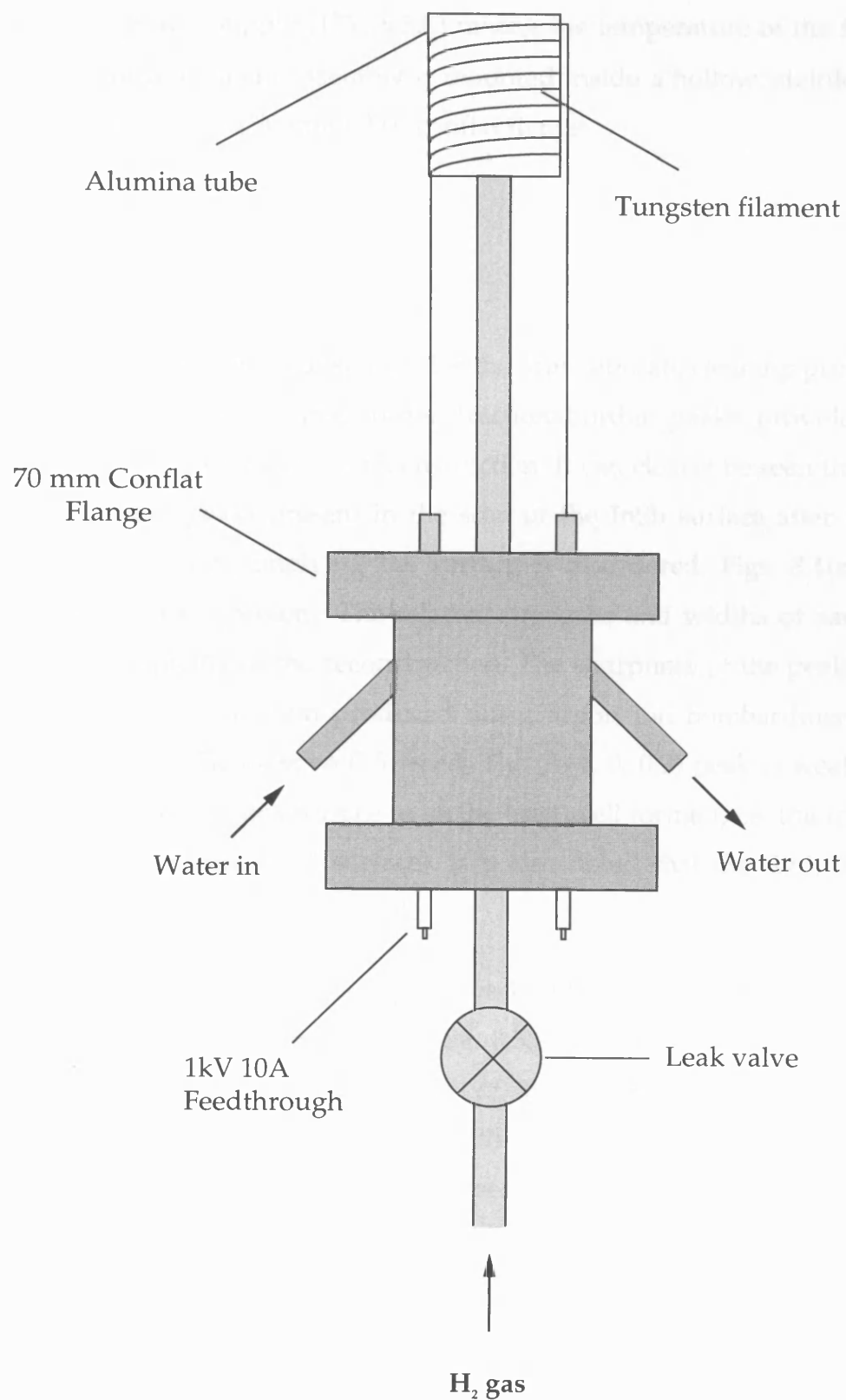
Fig. 8.3: *Schematic diagram of the hydrogen cracking cell.*

by a stabilised DC power supply (17V, 6.5A) raising the temperature of the filament to ~1750°C. The entire filament assembly is mounted inside a hollow, stainless steel cooling shroud, attached to a 70 mm UHV conflat flange.

8.3   Results.

Scans along the h axis in reciprocal space after the four separate cleaning procedures are shown in fig. 8.4. The quarter order fractional-order peaks provide direct evidence for the formation of a c(8x2) reconstruction. It can clearly be seen that there are no fractional-order peaks present in the scan of the InSb surface after thermal annealing alone, fig. 8.4(d), implying the surface is disordered. Figs. 8.4(a)-(c) all show quarter order peaks present. The relative strengths and widths of each peak gives a guide to the quality of the reconstruction. The sharpness of the peaks in fig. 8.4(a) indicates the reconstruction produced using argon ion bombardment at an elevated temperature is the most well formed. The (3/4, 0, 0.2) peak is weak in fig. 8.4(c), which would suggest this surface to be the least well formed, i.e. the roughest, (excluding the thermally annealed surface). It is also noted that the (1/4, 0, 0.2) is obscured by the tail of the bulk Bragg peak.

The (5/4, 0, 0.2) fractional-order reflections for each of the three surfaces exhibiting a reconstruction are shown in more detail in fig. 8.5(a)-(c). The peaks are fitted with Lorentzian curves. The correlation length of the reconstruction is inversely proportional to the FWHM of the reflection. While there is little difference in the correlation lengths between the hydrogen cleaned and sputtered/annealed surface, 187Å and 226Å respectively, the surface produced on ion bombardment at an elevated temperature is clearly more extensively formed with a correlation length of 2475Å.

The surface morphology and roughness are investigated by comparing the measured intensities along the (00λ) rod for each of the three surfaces. In the case of an ideally
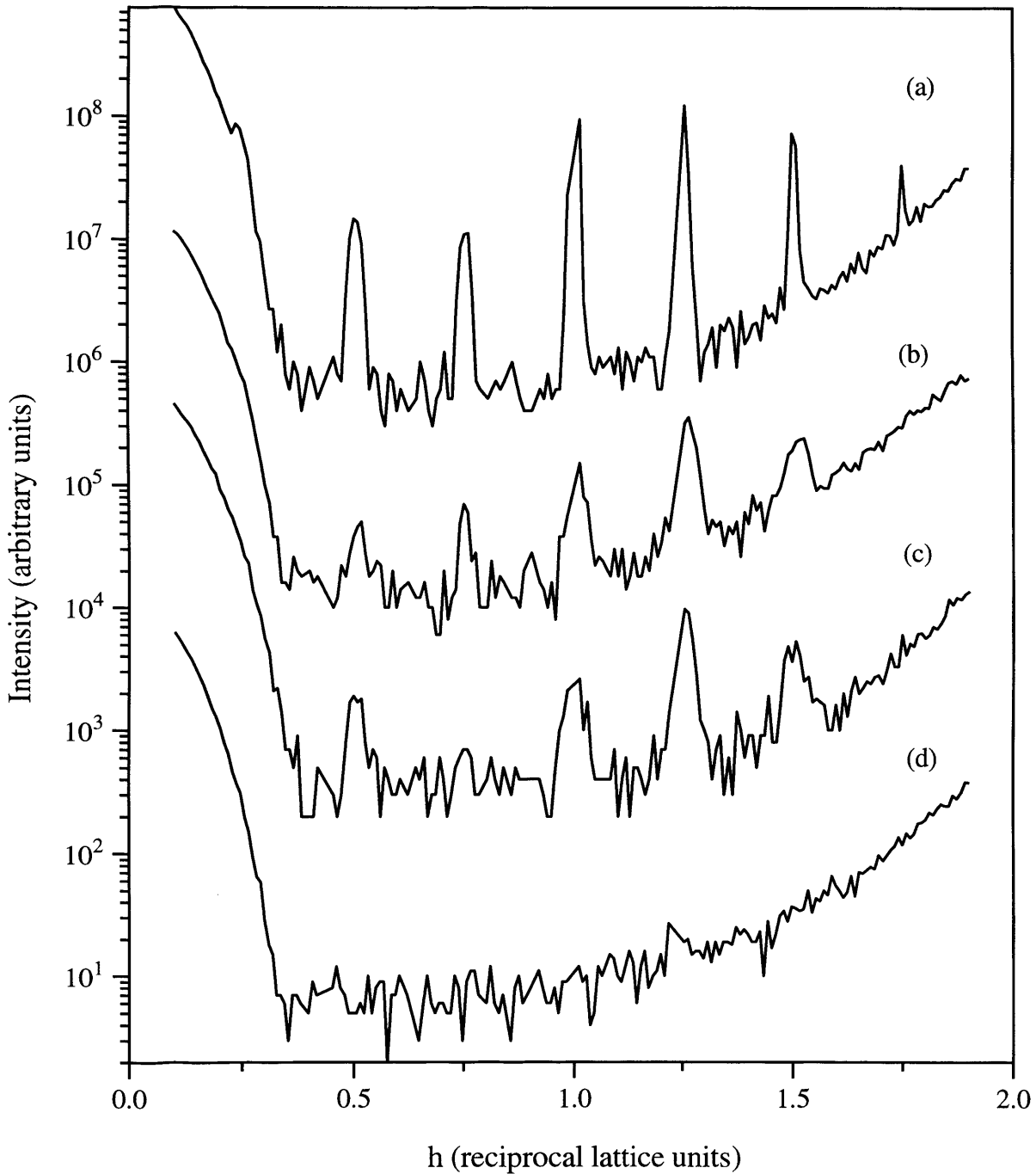
Fig 8.4: *Reciprocal space scans along (h, 0, 0.2) over two reciprocal lattice units after: (a) ion bombardment at 370°C, (b) ion bombardment at room temperature, (c) hydrogen irradiation at 370°C, (d) thermal annealing at 370°C. The quarter order peaks indicate the formation of a c(8x2) reconstruction in the first three cases. The curves have been offset for clarity.*
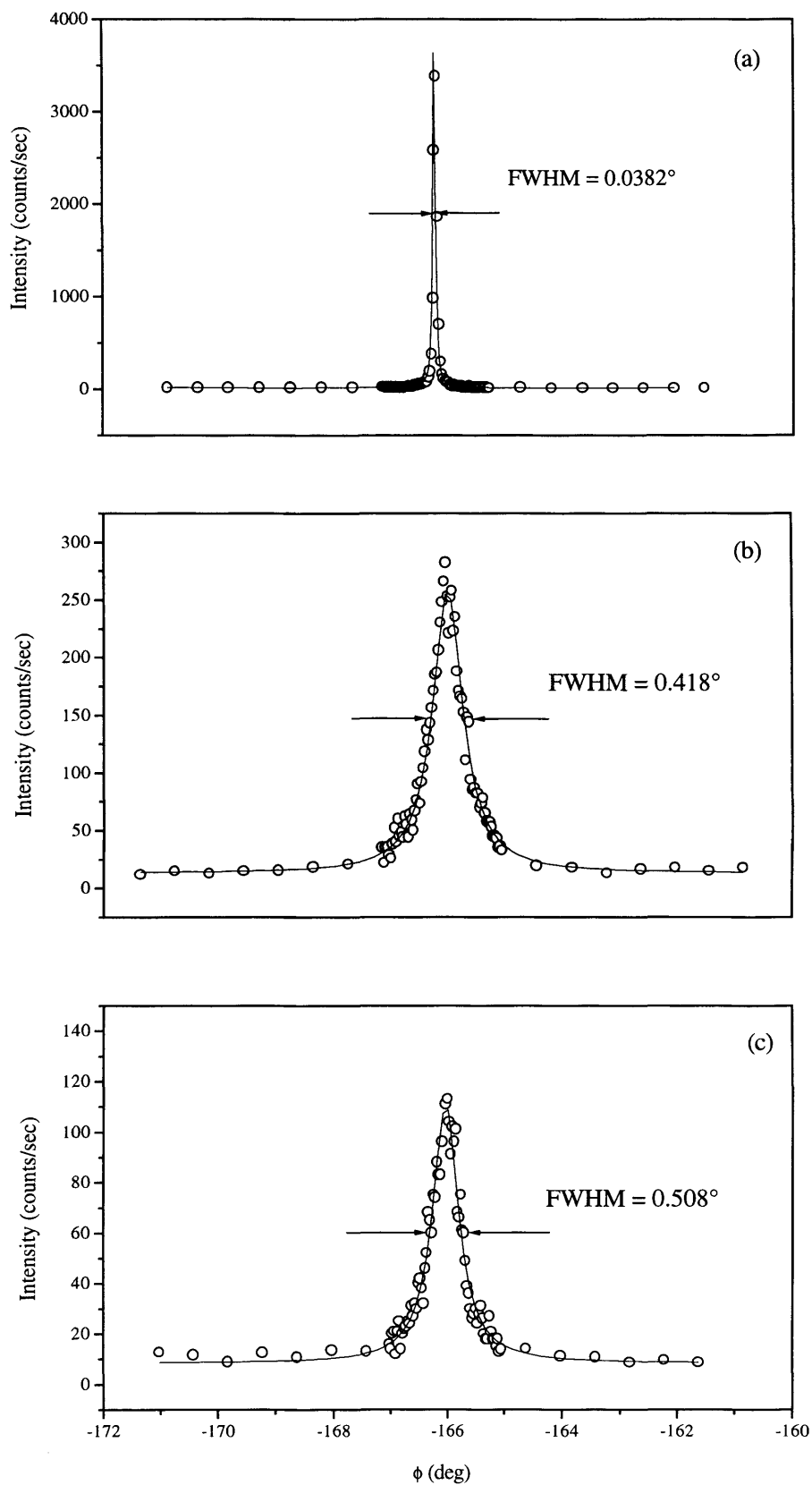
Fig 8.5: *The (5/4, 0, 0.2) fractional-order reflections of the c(8x2) reconstructed surface after: (a) ion bombardment AT 370°C, (b) ion bombardment at room temperature, (c) hydrogen irradiation at 370°C. The fitted curves are Lorentzian.*

flat reconstructed surface the structure factor F_{hkl} is given by contributions from the bulk and the surface:

$$F_{hkl} = \frac{f \exp\left[\dfrac{-BQ^2}{16\pi^2}\right]}{1 - \exp\left[-\pi i l - \left(\dfrac{a_3}{2\mu}\right)\right]} + \sum_j f_j \exp\left[\frac{-B_j Q^2}{16\pi^2}\right]\exp\left[\frac{2\pi i l z_j}{a_3}\right], \qquad (8.2).$$

where f is the atomic scattering factor of the bulk, μ ($>>a_3$) is the penetration depth, B is the bulk Debye-Waller factor, f_j is the atomic scattering factor of the jth atom and z_j is separation of the jth layer from the top layer of the undisturbed bulk. In the analysis the roughness is modelled in the manner described by Robinson [13]. The model assumes an exponential distribution of heights and this leads to an extra factor,

$$\left|F_{hkl}^{total}\right|^2 = \frac{(1-\beta)^2}{1+\beta^2 - 2\beta\cos Q.a_3}\left|F_{hkl}\right|^2. \qquad (8.3).$$

Fig. 8.6 shows the measured structure factor amplitudes along the specular (00λ) rod for the three different surfaces. It can be seen that although the curves overlap in the areas around the Bragg peaks, there is a notable discrepancy in the more surface-sensitive region between the Bragg peaks. This is a consequence of the varying roughness of each surface. The solid lines in the plot are the best fits to the data using the above expressions.

In fitting the specular rods the same structural model and a constant scale factor were used for all of the rods. The scale factor was determined from the fit to the points around the Bragg peak where bulk scattering dominates. The Debye-Waller
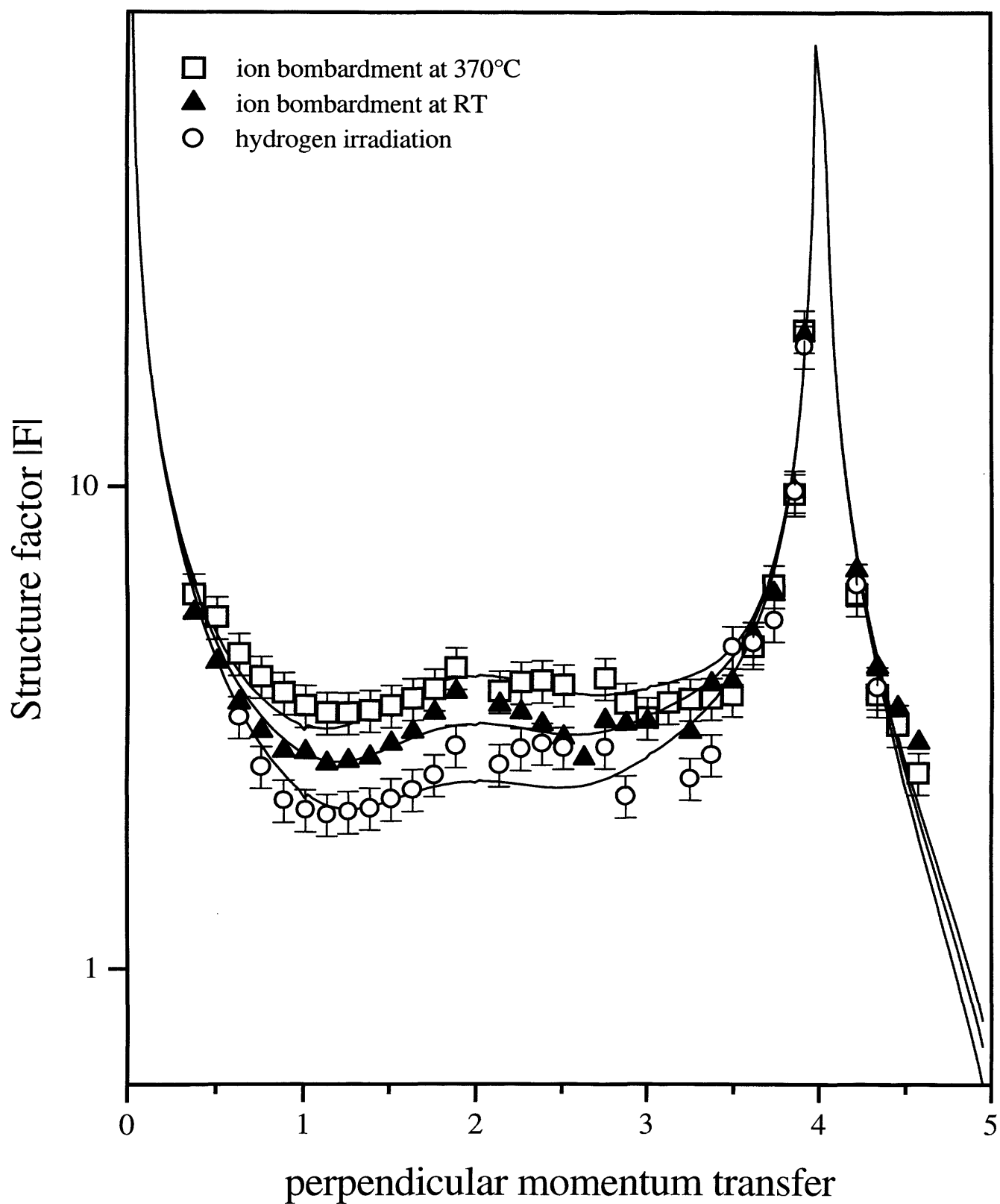
Fig. 8.6: *Scans of the specular reflectivity, (00l) rod, after the different cleaning treatments. The solid lines are the best fits using the equations discussed in the text. For clarity, the error bars have been omitted from one of the data sets.*

factor was held at the bulk value. The model used in the fitting was the three dimer model for the c(8x2) reconstruction reported by several groups [14,15,16]. A dimer layer was used in conjunction with an In-terminated bulk. The dimer layer height was initially set to be equal to that of what would have been the next unreconstructed bulk layer. First the heights of the dimers were allowed to vary in the direction perpendicular to the surface. The outer dimers were fixed at the same height to maintain symmetry. Atoms in the next four underlying layers were also allowed to vary perpendicularly to the surface. Like atom types in each layer were constrained to move together. After establishing the layer heights from the fitting, all parameters, except for the β-roughness, were fixed. The β-roughness parameter was allowed to vary for each of the three different surfaces, yielding the final fits shown in figs. 8.6(a)-(c). The results confirm that the surface formed by ion bombardment at elevated temperature to be the least rough, $\beta = 0.024$. The surface formed by hydrogen irradiation was somewhat surprisingly found to be the roughest, $\beta = 0.261$. These results are discussed later. The calculated β-roughness values and the corresponding χ^2 agreements of fit are shown in Table 8.1.

The specular rod was refitted in a similar manner using the structural model for the c(8x2) reconstruction derived in chapter 7. In this case, the upper layer and second layer In atoms were allowed to relax independently. The heights of the dimer atoms were also allowed to vary in the direction perpendicular to the surface, though the dimers were constrained to be symmetric, which was found to be the case in the structural analysis reported in chapter 7. Finally, atoms in the next two underlying layers, four and five, were allowed to relax in the perpendicular direction, the like atom types in each later being constrained to move together. The results were consistent with the above findings with respective β-roughness values of 0.017, 0.126 and 0.270 for the three surfaces as displayed in fig. 8.6(a)-(c). These results are also included in Table 8.1.

Cleaning Technique	β (3 dimer)	β (new model)	σ_{rms} (Å)	Correlation Length
sputtering and annealing	0.136	0.126	2.76	226Å
sputtering at elevated temperature	0.024	0.017	1.03	2475Å
hydrogen irradiation	0.261	0.270	4.48	187Å

Tab. 8.1: *Beta-roughness values for the three reconstructed surfaces, claculated using: (a) the three dimer model and (b) the model proposed in chapter 7. The root mean square roughness and correlation length of each surface is also included.*

8.4 Discussion.

The results clearly indicate the most successful technique to be the argon ion bombardment at an elevated temperature, the correlation length being approximately ten times greater than any of the reconstructions obtained using the other techniques. However, it is noted that the native oxide layer was removed by hydrogen irradiation and a subsequent clean surface reconstruction was formed. The least successful method was that of thermal annealing alone. This was not unexpected as several groups have reported the difficulty of this technique [2,17]. The absence of a surface reconstruction leads to the conclusion that surface contaminants still remain after the treatment, the resulting surface being disordered. It is noted that Liu et al [3] have reported successful thermal desorption of the native oxide layer, however in their case an Sb overpressure was present with the formation of volatile Sb oxides assisting oxide desorption. For completeness, thermal desorption under the same conditions in the presence of an Sb overpressure has also been attempted, but this also led to a rough surface, although the temperatures used for complete oxide desorption by Liu et al [3] were approximately 60°C higher, (430°C), than the ones used here. Such elevated temperatures, up to 450°C, have, however, been used in a similar method to Liu et al [3], when performing the transition study described in chapter 6. The resulting surfaces were again found to be rough with no reconstruction present.

Argon ion bombardment at both room and elevated temperatures efficiently removed the oxide layer from the InSb(001) surface. It can be seen, fig. 8.1, that the surfaces were In-rich with preferential depletion of the group V species. Despite the similarity between the two techniques the bombardment at the elevated temperature proved much more successful. A reason for this could be the increased mobility of the surface atoms at the higher temperature. Diffusion along any steps or terraces caused by the ion beam, will remove defects, minimising surface damage. Annealing after ion bombardment is less effective because the surface damage induced by the ion beam before annealing is more extensive and the subsequent annealing is not sufficient to produce an atomically flat surface. The surfaces produced by the ion

bombardment are, however, In-rich and may be electrically damaged with the creation of an n-type layer. This can lead to problems in the characterisation of epilayers grown on the surface during the manufacture of electronic devices.

Oxygen removal was achieved by the hydrogen irradiation method. The resulting surface reconstruction was not as sharp as the one produced by ion bombardment at an elevated temperature and the surface was notably rougher. The reason for this was probably carbon contamination from the outgassing filament. It can be seen in fig. 8.2 (a) and (b) that although the C peak is barely detectable after the first treatment, it is significant after the second treatment; the O peak, however, is no longer detectable. This suggests that the technique is indeed a valid one for oxygen removal and can be achieved with a very basic piece of apparatus. Higher quality surfaces have been obtained with the same technique using more sophisticated equipment [9,18], making use of ECR hydrogen plasmas. The AES spectra for the hydrogen cleaned surface, fig. 8.2, would suggest that group V depletion does not occur during hydrogen irradiation resulting in a more electrically balanced surface. This is very important in device fabrication, showing the benefits of hydrogen irradiation as a cleaning method. The oxide removal was believed to occur through the formation of hydrides at the surface, though we are unsure of the exact chemical mechanism of the reaction.

8.5   Summary.

The removal of the native oxide layer from InSb(001) substrates has been demonstrated using a number of techniques. The clean c(8x2) surface was successfully formed in the absence of an Sb overpressure. Argon ion bombardment at an elevated temperature resulted in the most well formed reconstruction. Hydrogen irradiation was also shown to be an efficient method for removing the surface oxide. There was noticeably less depletion of the group V species using hydrogen irradiation suggesting it to be a promising technique for the production of clean InSb(001) devoid of electrical damage.

References.

[1]   C.C. Chiang, P.H. Citrin and B. Schwartz, J. Vac. Sci. Technol. **14** (1977) 943.

[2]   G.W. Smith, A.J. Pidduck, C.R. Whitehouse, J.L. Glasper, A.M. Keir and
        C. Pickering, Appl. Phys. Lett. **59** (1991) 3282.

[3]   W.K. Liu and M.B. Santos, 7th Intl. Conf. Narrow Gap Semiconductors,
        Jan 8-12, 1995, Santa Fe.

[4]   W.T. Yuen, M.O. Schweitzer, T.S. Jones, C.F.McConville, E.A. Johnson,
        A. Mackinnon, N.V. Richardson and R.A. Stradling, Semiconductor Sci.
        Technol. **8** (1993) S396.

[5]   J.A. Schaefer, V. Persch, S. Stock, TH Allinger and A. Goldmann, Europhys.
        Lett. **12** (1990) Vol. 6, 563.

[6]   T. Sugaya and M. Kawabe, Jap. J. Appl. Phys. **30** (3A) L402.

[7]   R. Kobayashi, K. Fujii and F. Hasegawa, Inst. Phys. Conf. Ser. No. 120: Chap
        2. Int. Symp. GaAs and Related Compounds, Seattle, 1991.

[8]   S. Sugata, A. Takamori, N. Takado, K. Asakawa, E. Miyauchi and H.
        Hashimoto, J. Vac. Sci. Technol. **B6** (1988) 1087.

[9]   A.D. Johnson, G.M. Williams, A.J. Pidduck, C.R. Whitehouse, T. Martin, C.T.
        Elliot and T. Ashley, 7th Intl. Conf. Narrow Gap Semiconductors, Jan 8-12,
        1995, Santa Fe.

[10]   Z. Lu, Y. Jiang, W.I. Wang, M.C. Teich and R.M. Osgood Jr., J. Vac. Sci.
        Technol. **B10** (1992) 1856.

[11]   Y.J. Chun, T. Sugaya, Y. Okada and M. Kawabe, Appl. Phys. Lett. **55** (1989)
        760.

[12]   R.G. van Silfhout, J.F. van der Veen, C. Norris and J.E. Macdonald, Faraday
        Discussions of the Royal Chemical Society **89** (1990) 169.

[13]   I.K. Robinson, Phys. Rev. Lett. **57** (1986) 2714.

[14]   P. John, T. Miller and T.C. Chiang, Phys. Rev. **B39** (1989) 1730.

[15]   M.O. Schweitzer, F.M. Leibsle, T.S. Jones, C.F. McConville and N.V.
        Richardson, Surf. Sci. **280** (1993) 63.

[16]   M.D. Pashley, K.W. Huberern, W. Friday, J.M. Woodall and P.D. Kirchner,
        Phys. Rev. Lett. **60** (1988) 2176.

[17]   J.F. Klem, J.Y. Tsao, J.L. Reno, A. Datye and S. Chadda. J. Vac. Sci. Technol A
        9 (1991) 2996.

[18]   S. Yu Shapoval, P.V. Bulkin, A.A. Chumakov, S. A. Khudobin, I. Maximov and G. M. Mikhailov, Vacuum **43** (1992) No. 3, 195.

Chapter 9.

Summary.

9.1   Introduction.

The main experimental conclusions, which are presented in detail in chapters five to eight, are summarised here. The reader is referred to the relevant chapters for a more comprehensive discussion of each experiment.

9.2   InSb(001)-c(4x4).

The atomic structure of the InSb(001)-c(4x4) reconstruction has been determined using surface X-ray diffraction and has been found to consist of groups of three symmetric antimony dimers chemisorbed onto a complete antimony layer.

A comprehensive data set was taken, consisting of a total of 132 in-plane reflections, four integer-order and two fractional-order diffraction rods, which allowed a full three-dimensional structural model of the surface to be established. The two-dimensional Patterson function was uncomplicated revealing only two strong non-self correlation peaks within the irreducible part of the surface unit cell. This was found to be indicative of a simple dimer array. The two measured fractional-order rods were almost constant over a range of three reciprocal lattice units suggesting

that the reconstruction is limited to a depth of less than one third of the lattice parameter a_0.

The detailed in-plane fitting indicated that the central dimer length was very close to that in bulk antimony, whereas the outer dimers were slightly extended, being approximately eight per cent longer. The fitting also showed that the reconstruction was dominated by the top layer dimerisation; the underlying structure being essentially the same as that of the bulk arrangement. This result directly supported the evidence provided by the fractional-order rods, that the reconstruction was a shallow one. Further analysis also showed that the groups of dimers were incomplete in approximately one third of the cases. This result is consistent with STM images of the same surface on both InSb(001) and GaAs(001).

The Sb-rich InSb(001)-c(4x4) surface was found to be well-ordered and characterised by large domain sizes. The reconstruction was stable and extended less than $a_0/3$ into the bulk. These properties make the c(4x4) surface ideal for use in epitaxial growth and it is indeed the preferred starting surface for epitaxial growth on InSb.

9.3. Phase transition study.

The InSb(001) surface has been found to exhibit a continuous surface phase transition from a highly ordered c(4x4) surface phase to a poorly ordered A(1x3) phase at $\sim 350°C$. The phase transition was also found to be fully reversible when an external Sb flux was applied.

The integrated intensity and full-width-half-maximum of an intense fractional-order reflection, characteristic solely of the c(4x4) reconstruction, was measured as functions of both temperature and antimony flux. The integrated intensity is found to fall to zero at a critical transition temperature, which increases with increasing incident flux. The FWHM of the reflection is found to remain constant, within experimental error, with increasing temperature until very close to the transition temperature where there is a sharp rise in the width of the reflection. These results

indicate that the correlation length of the c(4x4) reconstruction remains approximately constant below the transition temperature, despite the fall in the integrated intensity. This implies that the destruction of the c(4x4) surface phase occurs in distinct isolated regions rather than in an overall reduction of domain size. The disordering transition is therefore proposed to occur due to random desorption of antimony dimer atoms in isolated areas, thus the general c(4x4) symmetry of the reconstruction is maintained until very close to the transition temperature. On reaching this point, the extent of the antimony desorption is so widespread that the c(4x4) symmetry is destroyed.

The evolution of a diffraction peak, characteristic of the A(1x3) reconstruction was also monitored as a function of temperature. The peak, however, is broad and weak in intensity indicating that the resulting A(1x3) surface is poorly ordered. The results provide evidence that the c(4x4) and A(1x3) reconstructions coexist on the InSb(001) surface.

9.4 InSb(001)-c(8x2).

The atomic structure of the InSb(001) has been determined by surface X-ray diffraction. A significantly different model, to those previously reported, has been proposed. The reconstruction has been found to be deeper than that of the Sb-rich c(4x4) surface and is composed of chains of indium atoms running parallel to, and separated by, pairs of antimony dimers on top of the antimony terminated bulk.

A large data set, consisting of 96 in-plane reflections and three integer-order diffraction rods, was recorded. In direct contrast to the c(4x4) surface, the two dimensional Patterson function was complicated with several different features present within the irreducible part of the surface unit cell. This immediately provided direct evidence against a simple dimer array for the c(8x2) reconstruction.

Through detailed fitting to both the in-plane and out-of-plane data sets using previously proposed models for the c(8x2) surface, as outlined in the relevant

chapter, it was found that none of the previously suggested models fully explained the experimental data. This necessitated the need for a new model, which is shown in fig. 7.9 and gave significantly better fits to both the in-plane and out-of-plane data. The indium chains closely resemble the bulk tetragonal structure, suggesting the bonding is metallic and the chains form a one-dimensional conducting path on the surface. The bonding geometry of the antimony dimers is notably similar to that found on the Sb-rich c(4x4) surface, the bond angles being indicative of sp^3-type bonding. This suggests that the antimony dimer, attached to a lower antimony layer, with a local coordination similar to that of the bulk, is a particularly stable unit. In contrast to the c(4x4) surface, the occupancy of the dimers on the c(8x2) surface was found to be complete.

The In-rich c(8x2) surface, as with the Sb-rich c(4x4) surface, was found to be well-ordered with large domain sizes. However, unlike the c(4x4) reconstruction, which is confined to the top layer, the c(8x2) reconstruction extends deeper into the bulk. This more developed reconstruction will impede ordered growth and again provides evidence why the c(4x4) surface is preferred for epitaxial growth.

9.5   Oxide Removal.

The removal of the native oxide layer of InSb(001) has been monitored using surface X-ray diffraction. A number of methods, namely: ion bombardment at room temperature, ion bombardment at elevated temperature and hydrogen irradiation were successful in removing the oxide layer. Complete oxide removal, however, was not achieved after thermal annealing alone.

The reflected X-ray intensity was measured for each of the resulting surfaces, from which the roughness of each surface was determined. The results indicate that argon ion bombardment at elevated temperature was the most successful technique used, the root mean square roughness of the resulting surface being approximately a factor of 3 to 4 lower than the values obtained using the other two methods.

Reciprocal space lattice scans showed that the resulting surfaces possessed c(8x2) symmetry, which was as expected as the techniques were performed in the absence of an antimony overpressure. The in-plane fractional order reflections measured for each surface also indicated that the ion bombardment at elevated temperature produced the most well formed surface as the correlation length for this reconstruction was found to be approximately a factor of ten greater than for the reconstructions obtained using the other methods.

The Auger electron spectroscopy results show that the surfaces produced by argon ion bombardment are indium rich with significant depletion of the group V species taking place. However, the corresponding spectra for the surface produced by hydrogen irradiation suggest that group V depletion does not occur on using this technique. This lack of antimony depletion can result in a more electrically balanced surface which is important in the manufacture of electronic devices.

9.6   Suggestions for future work.

The clean surface reconstructions of InSb(001) have been comprehensively studied in this thesis. The precise atomic structures of both the Sb-rich c(4x4) reconstruction and the In-rich c(8x2) reconstruction have been determined using surface X-ray diffraction. The results confirm that the previously proposed missing dimer model is the correct model for the c(4x4) reconstruction and a detailed picture of the atomic coordinates has been established for the first time. In contrast, the results for the c(8x2) reconstruction clearly indicate that all previously proposed models for the reconstruction are incorrect. A new model, consisting of chains of indium atoms separated by parallel pairs of antimony dimers has therefore been proposed.

In addition to the interest in chemically clean semiconductor surfaces, as highlighted in this thesis, a large number of studies have focused on the growth of thin films of noble metals on the surface of semiconductors. Research in this direction has been generated by the technological importance of metallisation of semiconductors, which is a crucial stage in the fabrication of modern electronic devices. Metallic contacts

168

consist of a metal layer, several thousand Angstroms thick, on top of a single crystal semiconductor substrate. The resulting interface can be affected by many factors, including three dimensional island nucleation, alloy formation and penetration. The metal growth is therefore strongly dependent on the quality of the initial monolayer of adsorbate atoms.

Preliminary data of the growth of Au on the InSb(001)-c(8x2) surface is shown in fig. 9.1. The data was taken on the 9.4 beamline at the SRS, Daresbury and shows the variation of the specularly reflected X-ray intensity with deposition time for substrate temperatures of 350°C, 20°C and -190°C respectively. The X-ray intensity was recorded at a grazing angle of 8.00°, which corresponds to a momentum transfer with reciprocal lattice vector (001), that is, the Anti-Bragg position.

The first two plots, (a) and (b), show a small initial rise in intensity, followed by a point of inflection further along the curve and a rapid fall in intensity. For perfect layer-by-layer growth a series of oscillations with distinct maxima and minima would be observed; the absence of such features indicates that three dimensional islanding is probably occurring, that is, new layers are being formed before existing ones are completed. The resulting interface will therefore be disrupted. Plot (c), however, is notably different with definite oscillations present, which may be indicative of layer-by-layer growth. The rapid decay in the intensity of the oscillations, however, imply that the growth may still be poorly ordered and the interface could therefore be disrupted. A possible explanation of why layer-by-layer growth is only observed at the lower temperature is that the c(8x2) surface undergoes a phase transition upon cooling.

Further data, showing the growth of In on the InSb(001)-c(4x4) surface is shown in fig. 9.2. It has already been shown (chapters 5 and 7) that the c(4x4) surface is notably flatter than the c(8x2) surface and it would be reasonable to expect that layer-by-layer growth would be more likely to occur on the c(4x4) surface. The data shown in fig. 9.2 was taken on the W12 beamline at LURE, Paris and also shows the
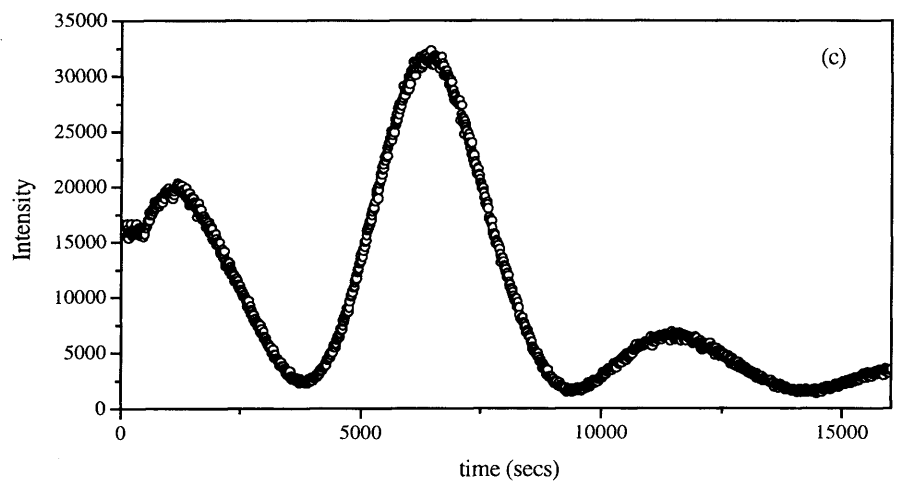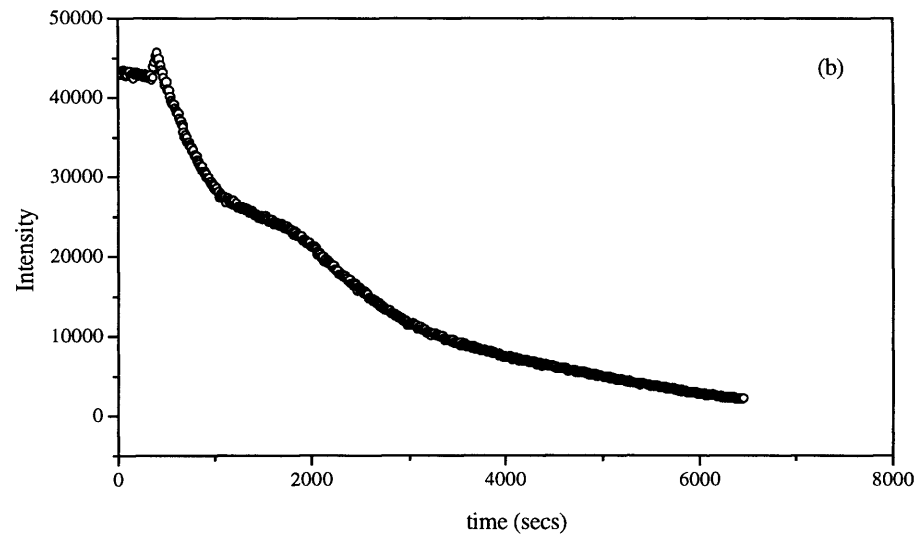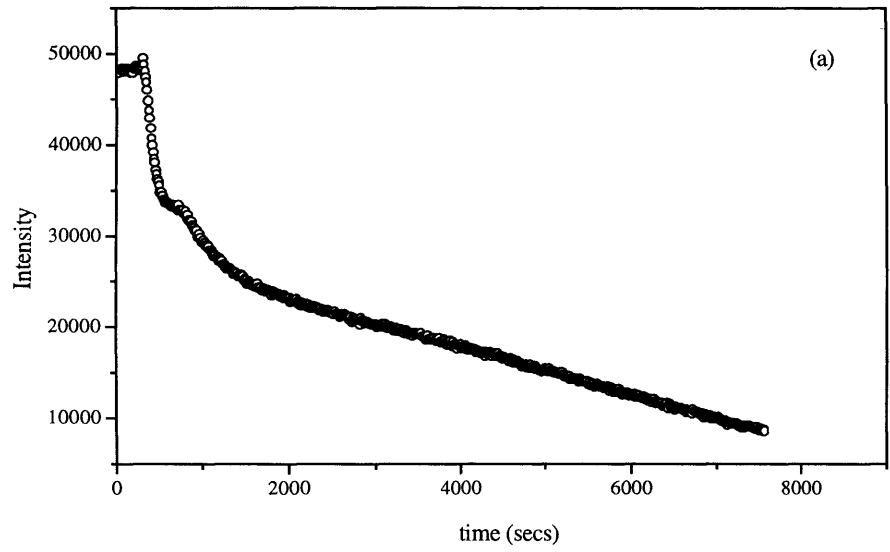
Fig 9.1 : *The specularly reflected X-ray intensity as a function of time for the growth of Au on InSb(001) at a substrate temperature of: (a) 350°C, (b) 20°C and (c) -190°C.*
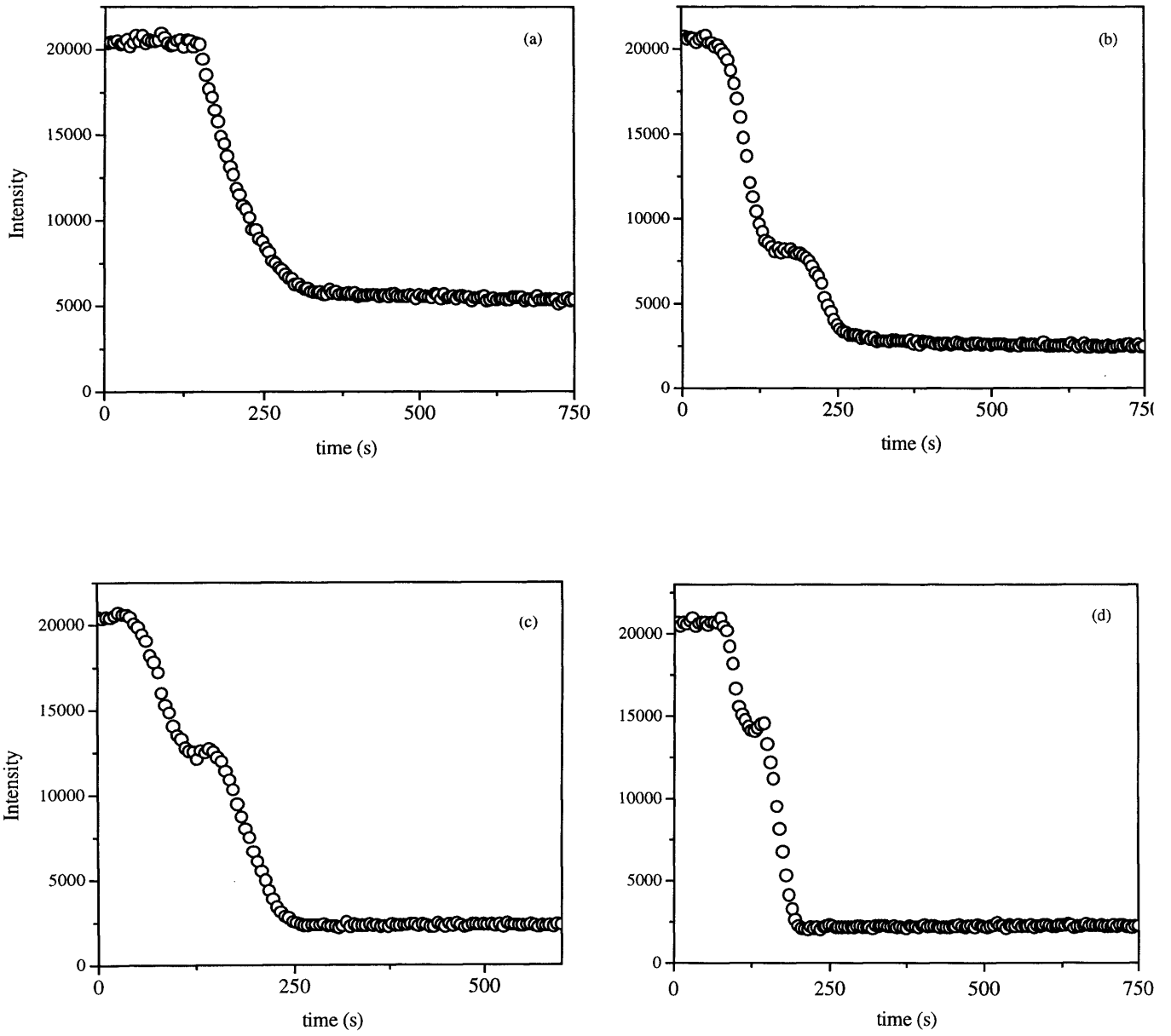
Fig 9.2 : *The specularly reflected intensity as a function of time for the growth of In on InSb(001) at a substrate temperature of: (a) 20°C, (b) 200°C, (c) 250°C and (d) 300°C*

variation of the specularly reflected X-ray intensity as a function of deposition time, for various substrate temperatures. The most notable feature of the In growth data is the presence of a maximum in the growth curve at the higher temperatures, which appears sharper and increasingly faster as the substrate temperature is increased. This is most likely to be due to the increased mobility of the In atoms at the higher temperatures.

A natural extension to the work in this thesis would therefore be, a continuation of the preliminary growth studies and full in-plane and out-of-plane analyses could be used to accurately determine any novel growth structures.